Astronomy & Astrophysics

A sensitive APEX and ALMA CO(1–0), CO(2–1), CO(3–2), and [CI](1–0) spectral survey of 40 local (ultra-)luminous infrared galaxies

I. Montoya Arroyave[1], C. Cicone[1], E. Makroleivaditi[2,3], A. Weiss[2], A. Lundgren[4], P. Severgnini[5], C. De Breuck[4], B. Baumschlager[1], A. Schimek[1], S. Shen[1], and M. Aravena[6]

[1] Institute of Theoretical Astrophysics, University of Oslo, PO Box 1029, Blindern 0315 Oslo, Norway
e-mail: isabemo@uio.no

[2] Max-Planck-Institut fur Radioastronomie, Auf dem Hugel 69, 53121 Bonn, Germany

[3] Rheinische Friedrich-Wilhelms-Universitat Bonn, Regina-Pacis-Weg 3, 53113 Bonn, Germany

[4] European Southern Observatory, Karl-Schwarzschild-Strasse 2, 85748 Garching, Germany

[5] INAF – Osservatorio Astronomico di Brera, Via Brera 28, 20121 Milano, Italy

[6] Instituto de Estudios Astrofísicos, Facultad de Ingeniería y Ciencias, Universidad Diego Portales, Av. Ejército Libertador 441, Santiago, Chile

ABSTRACT

We present a high sensitivity, ground-based spectral line survey of low-J carbon monoxide (CO($J_{up} \rightarrow J_{up} - 1$) with $J_{up} = 1, 2, 3$) and neutral carbon [CI] $^3P_1 - ^3P_0$ ([CI](1–0)) in 36 local ultra-luminous infrared galaxies (ULIRGs) and 4 additional LIRGs, all of which have previous *Herschel* OH 119 μm observations. The study is based on new single-dish observations conducted with the Atacama Pathfinder Experiment (APEX) and complemented with archival APEX and Atacama Large Millimeter Array (ALMA and ACA) data. Our methods are optimized for a multi-tracer study of the total molecular line emission from these ULIRGs, including any extended low-surface-brightness components. We find a tight correlation between the CO and [CI] line luminosities, which suggests that the emission from CO(1–0) (and CO(2–1)) arises from similar regions as the [CI](1–0), at least when averaged over galactic scales. By using [CI] to compute molecular gas masses, we estimate a median CO-to-H$_2$ conversion factor of $\langle \alpha_{CO} \rangle = 1.7 \pm 0.5 M_\odot$ (K km s^{-1}pc^2)$^{-1}$ for ULIRGs. We derive median galaxy-integrated CO line ratios of $\langle r_{21} \rangle = L'_{CO(2-1)}/L'_{CO(1-0)} = 1.09$, $\langle r_{31} \rangle = L'_{CO(3-2)}/L'_{CO(1-0)} = 0.76$, and $\langle r_{32} \rangle = L'_{CO(3-2)}/L'_{CO(2-1)} = 0.76$, significantly higher than normal star-forming galaxies, confirming the exceptional molecular gas properties of ULIRGs. We find that the r_{21} and r_{32} ratios are poor tracers of CO excitation in ULIRGs, while r_{31} shows a positive trend with L_{IR} and star formation rates and a negative trend with the H$_2$ gas depletion timescales (τ_{dep}). Our investigation of CO line ratios as a function of gas kinematics shows no clear trends, except for a positive relation between r_{21} and σ_v, which can be explained by CO opacity effects. These ULIRGs are also characterized by high $L'_{[CI](1-0)}/L'_{CO(1-0)}$ ratios, with a measured median value of $\langle r_{CICO} \rangle = 0.18$, higher than values from previous interferometric studies that were affected by missing [CI] line flux. The r_{CICO} values do not show a significant correlation with any of the galaxy properties investigated, including OH outflow velocities and equivalent widths. We find that the widths of [CI](1–0) lines are ~10% smaller than those of CO lines, and that this discrepancy becomes more significant in ULIRGs with broad lines ($\sigma_v > 150$ km s^{-1}) and when considering the high-v wings of the lines. This suggests that the low optical depth of [CI] can challenge its detection in diffuse, low-surface-brightness outflows and, therefore, its use as a tracer of CO-dark H$_2$ gas in these components. Finally, we find that higher L_{AGN} are associated with longer τ_{dep}, consistent with the hypothesis that active galactic nucleus feedback may reduce the efficiency of star formation. Our study highlights the need for sensitive single-dish multi-tracer H$_2$ surveys of ULIRGs that are able to recover the flux that is missed by interferometers, especially in the high-frequency lines such as [CI]. The Atacama Large Aperture Submillimeter Telescope (AtLAST) will be transformational for this field.

Key words. galaxies: evolution – submillimeter: galaxies – galaxies: active – galaxies: starburst – galaxies: ISM – galaxies: interactions

1. Introduction

In the local ($z \lesssim 0.2$) Universe, ultra-luminous infrared galaxies (ULIRGs, where $L_{IR}(8 - 1000$ μm$) \geq 10^{12} L_\odot$) and luminous infrared galaxies (LIRGs, where $L_{IR}(8 - 1000$ μm$) \geq 10^{11} L_\odot$) pinpoint gas-rich galaxy mergers undergoing intense starbursts (SBs) and supermassive black hole accretion (Sanders & Mirabel 1996; Genzel et al. 1998; Lonsdale et al. 2006; Pérez-Torres et al. 2021; U 2022). These processes together deeply modify the physical and dynamical proper-

ties of the interstellar medium (ISM), likely leading to a permanent morphological transformation and quenching (e.g., Hopkins et al. 2008).

(Sub)millimeter interferometric observations of CO lines (e.g., Downes & Solomon 1998; Wilson et al. 2008; Ueda et al. 2014) and dense H$_2$ gas tracers such as HCN and HCO$^+$ (Aalto et al. 2012; Imanishi & Nakanishi 2014; Imanishi et al. 2019; Ledger et al. 2021) show that the extreme star formation rates (SFRs) of (U)LIRGs are fueled by massive ($M_{H_2} > 10^9 M_\odot$), dense H$_2$ gas reservoirs, characterized by a high

surface brightness in the central kiloparsec-scale region. However, feedback mechanisms and tidal forces can disperse ISM material outside of the nuclear regions (Springel et al. 2005; Narayanan et al. 2006, 2008; Duc & Renaud 2013). Hence, we can expect a portion of the ISM of (U)LIRGs to reside in diffuse, low-surface-brightness structures, possibly missed by high-resolution interferometric observations.

Galactic outflows have been ubiquitously observed in (U)LIRGs for decades, in the ionized (Westmoquette et al. 2012; Arribas et al. 2014) and atomic (Rupke et al. 2005; Martin 2005; Cazzoli et al. 2014) gas phases, as expected in sources affected by strong radiative feedback from SBs and active galactic nuclei (AGNs; e.g., Costa et al. 2018; Biernacki & Teyssier 2018). More recent is the discovery that the outflows of (U)LIRGs can embed large amounts of molecular gas, traveling at speeds of up to $v \sim 1000$ km s^{-1}. Such molecular outflows have been detected unambiguously by *Herschel*, via observations of P-Cygni profiles and/or blueshifted absorption components of far-infrared (FIR) OH, H$_2$O, and OH$^+$ transitions (Fischer et al. 2010; Sturm et al. 2011; Spoon et al. 2013; Veilleux et al. 2013; Stone et al. 2016; González-Alfonso et al. 2017, 2018), as well as through the investigation of broad and/or high-velocity components of CO (Feruglio et al. 2010, 2015; Cicone et al. 2012, 2014; Pereira-Santaella et al. 2018; Lutz et al. 2020; Fluetsch et al. 2019; Lamperti et al. 2022), HCN, HCO$^+$ (Aalto et al. 2012, 2015; Barcos-Muñoz et al. 2018), and CN (Cicone et al. 2020) emission lines. These sensitive observations have also shown that the molecular ISM of (U)LIRGs, and especially the low-surface-brightness outflow components (e.g., Feruglio et al. 2013; Cicone et al. 2018; Herrera-Camus et al. 2020), can extend to several kiloparsecs, up to the edge of the field of view of single-pointing interferometric data.

Obtaining robust H$_2$ mass measurements of the total ISM reservoirs as well as of the gas embedded in outflows is crucial for understanding the impact of gas-rich galaxy mergers – and of the collateral powerful SB and AGN feedback mechanisms – on galaxy evolution. Low-J CO lines such as CO(1–0) and CO(2–1) can be used to estimate H$_2$ masses through a CO-to-H$_2$ conversion factor (hereafter $\alpha_{\rm CO}$); it is, however, highly dependent on the physical state of the gas. The $\alpha_{\rm CO}$ parameter can vary by up to a factor of ~ 10 in different ISM environments, depending on the CO optical depth, on the metallicity of the medium, and on the exposure to far-UV radiation and cosmic rays (CRs) that can destroy CO more than H$_2$ (see, e.g., Bisbas et al. 2015; Glover et al. 2015; Offner et al. 2014). For the molecular ISM of disk galaxies, the conventional $\alpha_{\rm CO}$ factor is 4.3 $M_\odot$ (K km s^{-1} pc^{-2})$^{-1}$ (Strong & Mattox 1996; Abdo et al. 2010; Bolatto et al. 2013), while for more perturbed galaxies, such as gas-rich mergers and SBs, a lower $\alpha_{\rm CO}$ factor of $\sim 0.8 - 1.0$ $M_\odot$ (K km s^{-1} pc^{-2})$^{-1}$ is often preferred (Downes & Solomon 1998).

Combining multiple molecular transitions can help constrain the physical properties of molecular gas and so derive a better estimate of the $\alpha_{\rm CO}$ factor. A particularly valuable H$_2$ gas tracer is the forbidden $^3P_1 - ^3P_0$ fine structure line of atomic carbon, hereafter [CI](1–0), which has an excitation temperature of $T_{\rm ex} = 23.6$ K and a critical density similar to that of CO(1–0) (i.e., $n_{crit,[CI]} \sim 1000$ cm^{-3}). The [CI](1–0) line is optically thin and has a simple three-level partition function, which makes it easier to interpret than low-J CO lines (see the discussion in Papadopoulos et al. 2022). Early models of photodissociation regions (PDRs) predicted [CI] to exist in a thin transition layer between the central region of molecular clouds (molecular gas – CO) and its envelope (ionized gas – [CII]; for the standard PDR view, see Tielens & Hollenbach 1985). How-

ever, observations have shown [CI] to be well mixed with CO widely throughout the cloud (Valentino et al. 2018; Saito et al. 2020; Papadopoulos et al. 2022), suggesting that both species might trace the bulk of molecular gas mass (Ojha et al. 2001; Papadopoulos et al. 2004; Kramer et al. 2008; Salak et al. 2019; Izumi et al. 2020; Jiao et al. 2017). Moreover, theoretical models show that CO (but not H$_2$) may be destroyed in environments dominated by CRs, shocks, or intense radiation fields, leaving behind CO-dark or CO-poor reservoirs; this provides support to the idea of [CI] being an alternative H$_2$ gas mass tracer.

Observing the atomic carbon emission from local galaxies requires a sensitive submillimeter telescope located at a very high and dry site. Indeed, the [CI](1–0) transition, at a rest frequency of $\nu^{\rm rest}_{\rm [CI](1-0)} = 492.161$ GHz (609.135 µm), in the absence of a significant redshift, can be observed only if the atmospheric opacity is low (precipitable water vapor PWV < 1 mm). For this reason, sensitive observations of [CI](1–0) in the local Universe are still very sparse, even for bright (U)LIRGs. Cicone et al. (2018) used the Atacama Large Millimeter/submillimeter Array (ALMA) and the Morita Array (also known as the Atacama Compact Array, ACA) to obtain high S/N [CI](1–0) observations of NGC 6240. These data, combined with archival CO(1–0) and CO(2–1) observations, were used to study the $r_{21} \equiv L'_{\rm CO(2-1)}/L'_{\rm CO(1-0)}$ and $r_{\rm CICO} \equiv L'_{\rm [CI](1-0)}/L'_{\rm CO(1-0)}$ line ratios (the latter can be used to estimate $\alpha_{\rm CO}$) in the massive molecular outflow of NGC 6240. From a spatially resolved analysis, Cicone et al. (2018) find that the outflowing ISM in NGC 6240 is robustly characterized by an $\alpha_{\rm CO}$ that is lower than the non-outflowing H$_2$ medium, and that r_{21} is higher for high-σ_v outflow components, especially at large distances from the nuclei. The Cicone et al. (2018) analysis suggests that: (i) despite its obvious limitations, a multicomponent decomposition of galaxy-integrated spectra, performed simultaneously to multiple transitions, which enables an investigation of line ratios separately for spectral components with different widths and central velocities, can deliver results that are consistent with a proper spatial decomposition of the ISM for the outflowing and disk material; and (ii) the outflowing H$_2$ gas may be characterized by different physical properties from the non-outflowing ISM of NGC 6240, and in particular by a lower CO optical depth and a higher CO excitation. These results have been obtained on a single, extreme source, and further statistics are required.

Our study builds upon these previous results and aims to expand the analysis of Cicone et al. (2018) to a sample of 36 local ULIRGs and 4 additional LIRGs with low-J CO (up to J=3) and [CI](1–0) line observations. In designing our survey, we paid particular attention to capturing the total flux from these sources, including possible extended low-surface-brightness components that may be dominated by outflows and tidal tails and may be missed by high-resolution, low S/N interferometric data. The final survey contains proprietary and archival data from the Atacama Pathfinder EXperiment (APEX) telescope, ALMA, ACA, and the IRAM Plateau de Bure Interferometer (PdBI, now the NOrthern Extended Millimeter Array, NOEMA), which we have re-reduced and reanalyzed in a consistent and uniform way. Therefore, we can rely both on a consistent data analysis and on high-quality spectra, all taken with receivers whose large instantaneous intermediate frequency (IF) bandwidth can properly sample the extremely broad emission lines of (U)LIRGs.

This paper is organized as follows. In Sect. 2 we describe the sample selection. In Sect. 3 we describe the observing strategy, the observations, and the data reduction. In Sect. 4 we explain the methodology used for the spectral fitting and the data

analysis. Our results are presented in Sect. 5, where they are also contextualized through a comparison with relevant results from the literature. A more general discussion is reported in Sect. 6. Finally, Sect. 7 summarizes the main results and presents the conclusions of our work. Throughout this work, we adopt a Λ cold dark matter cosmology, with $H_0 = 67.8$ km s^{-1}Mpc^{-1}, $\Omega_M = 0.307$, and $\Omega_\Lambda = 0.693$ (Planck Collaboration XVI 2014).

2. The sample

In absence of additional spatial information, the only unambiguous method for assessing the presence of molecular outflows trough spectroscopy, is the detection of P-Cygni profiles or blueshifted absorption components in molecular transitions, such as the OH119 μm line observed by *Herschel* (Fischer et al. 2010; Sturm et al. 2011). However, the absence of these features does not necessarily rule out the presence of outflows, as in the case of NGC 6240, studied in Cicone et al. (2018). In this source, OH is detected only in emission despite the presence of an extreme molecular outflow detected in multiple tracers. For this reason, molecular emission line observations can provide valuable and unique information on the presence and properties of galactic outflows, complementary to OH data.

The *Herschel* OH targets studied by Veilleux et al. (2013) and Spoon et al. (2013) represent the only conspicuous sample of (U)LIRGs that has uniform and unambiguous prior information about their molecular outflows, hence providing a robust comparison data set for our investigation based on emission lines. Moreover, the southern targets in this sample also have plenty of ancillary data from ALMA and APEX, allowing us to capitalize on public archives, which is a main focus of this work. For these reasons, the targets in our sample are selected from the Spoon et al. (2013) and Veilleux et al. (2013) samples, regardless of the detection of a molecular outflow in OH.

From the parent *Herschel* samples, we have included all sources with declination $\delta < 15$ deg, except IRAS 12265+0219 and IRAS 00397-1312 for which we did not have any data available[1]. NGC 6240 satisfies our selection criteria but is excluded from our work because it was the target of the pilot study by Cicone et al. (2018). Our sample includes 36 ULIRGs, whose physical properties such as redshifts, L_{IR}, SFRs, and AGN fractions ($\alpha_{AGN} \equiv L_{AGN}/L_{bol}$) are reported in Table 1 with their corresponding references. The 4 additional LIRGs reported in Appendix A have been reduced and analyzed consistently with the rest of the sample, but they have been excluded from the main body of the paper to avoid biasing the relations given the low statistics for these low-L_{IR} sources. Hereafter, we use the term "(U)LIRGs" when referring to the entire sample, and "ULIRGs" when we exclude the 4 LIRGs.

The parent *Herschel* samples from which our targets were selected have a redshift upper limit of $z < 0.2$. As a result, our study investigates local (U)LIRGs with redshifts ranging from $z = 0.00708$ (IRAS F12243–0036) to $z = 0.1935$ (IRAS F05024–1941). The sample is by definition composed by high-L_{IR} galaxies with L_{IR} ranging from $10^{11} L_\odot$ to $10^{12.8} L_\odot$, covering luminosities within the (U)LIRG regime. The sources span a wide range in α_{AGN} values from 0.0 up to 0.92, with ~50% of the sources having $\alpha_{AGN} \geq 0.5$. The SFRs are taken from the parent sample papers, with the exception of galaxies selected in Veilleux et al. (2013) for which there are no SFRs reported.

---

[1] The galaxy IRAS 00397-1312 was registered to have APEX CO(2–1) archival data; however, when opened, it returns an empty file, and it was not possible to reobserve this source within our PI programs.

In those cases, we followed the method by Sturm et al. (2011; also used in Spoon et al. 2013) to obtain the SFRs using: SFR = $(1 - \alpha_{AGN}) \times 10^{-10} L_{IR}$, so that all values are computed uniformly. The SFRs range from a couple of solar masses a year up to ~300 $M_\odot$yr^{-1}. We checked that our sample of ULIRGs is representative, in terms of physical properties (e.g., SFR, L_{AGN}, α_{AGN}) of the local ULIRG population by comparing it with the QUEST (Quasar/ULIRG Evolutionary Study) sample at $z < 0.2$ (see Veilleux et al. 2009a). Most previous works studying the molecular gas in local (U)LIRGs have included both LIRGs and ULIRGs. We compare some of our results with the works of Herrero-Illana et al. (2019) and Jiao et al. (2017), whose samples are however heavily dominated by LIRGs as opposed to ours. As the distinction between LIRGs and ULIRGs is based on an arbitrary L_{IR} cut, several galaxies that are officially LIRGs (such as NGC 6240) belong to the same population as the more infrared-luminous ULIRGs.

Table 1 lists the OH outflow velocity values for the sources (29 out of the whole sample of 40) that show an OH outflow detection according to Veilleux et al. (2013) and Spoon et al. (2013). We also report the OH equivalent widths for the whole sample.

Our sample, which focuses on southern (U)LIRGs targeted by previous *Herschel* OH observations, has naturally a large overlap with the APEX and ALMA/ACA public archives. Indeed, many of these sources have been observed in previous projects targeting different molecular tracers. In this work, we make the most out of such archives, focusing on the low-J CO transitions and [CI] atomic carbon line, and we complement them with our own new proprietary high-sensitivity single-dish observations with APEX. The observations and the data reduction process are described in detail in Sect. 3.

3. Observations

3.1. Observing strategy and data reduction

We want to study simultaneously the total integrated line emission from the three lowest-J transitions of CO and from [CI](1–0) in our sample of 40 (U)LIRGs. To do so, we combine proprietary and archival single-dish (APEX) and interferometric (ACA, ALMA, and IRAM PdBI) observations. The final, reduced spectra employed in our analysis are all shown in Figs. B.1–B.6.

In Table B.1 we report all the data sets considered in this paper with their respective project IDs. In those cases where multiple spectra are available for the same source and transition, we report at the top of the corresponding row in Table B.1 the data set that was used for our main analysis, followed by the one(s) that are not employed in the analysis. In such cases of duplication, we assign higher priority to data sets with the highest sensitivity to large-scale structures, namely: (1) APEX PI data, (2) APEX archival data, (3) ACA archival data, and, lastly, (4) ALMA archival data. In this way, we prioritize single-dish data that better trace the total flux, including possible extended emission that can be filtered out by interferometric observations. If, for a given transition, single-dish data exist but are of poor quality (i.e., have a low S/N or are affected by instrumental issues), we prefer the ACA or ALMA data when available for the same transition, after carefully checking that there is no significant flux loss. The ALMA/ACA archival data used here are not tailored to the aim of our study, and therefore, the angular resolutions and maximum recoverable scales (MAS) of the interferometric observations vary over a wide range, from a fraction of arcsec (in the most extended ALMA antenna configurations), up

Table 1. Galaxies analyzed in this work along with some general properties.

Galaxy name	z	RA	Dec	α_{AGN}	$\log L_{IR}$ [$L_\odot$]	$\log L_{AGN}$ [$L_\odot$]	SFR [$M_\odot\,yr^{-1}$]	OH$_{max}$ [†] [km s^{-1}]	OH$_{EQW}$ [†] [km s^{-1}]	Ref.
(1)	(2)	(3)	(4)	(5)	(6)	(7)	(8)	(9)	(10)	(11)
IRAS 00188−0856	0.1284	00:21:26.522	−08:39:25.98	0.51	12.39	12.16	120±50 [*]	−1781	−305	γ
IRAS 01003−2238	0.1178	01:02:50.007	−22:21:57.22	0.83	12.32	12.30	36±14	−1238	−276	γ
IRAS F01572+0009	0.1631	01:59:50.253	+00:23:40.87	0.65	12.62	12.49	150±60 [*]	−1100::	0	β
IRAS 03521+0028	0.1519	03:54:42.219	+00:37:03.41	0.06	12.52	11.39	309±120	−100	−26	γ
IRAS F05024−1941	0.1935	05:04:36.555	−19:37:02.83	0.07	12.37	11.30	220±80 [*]	−850::	−83	β
IRAS F05189−2524	0.0426	05:21:01.392	−25:21:45.36	0.72	12.16	12.07	40±16 [*]	−850	−10	β
IRAS 06035−7102	0.0795	06:02:54.066	−71:03:10.48	0.60	12.22	12.06	70±30	−1117	−128	γ
IRAS 06206−6315	0.0924	06:21:01.210	−63:17:23.5	0.43	12.23	11.92	100±40	−750	−272	γ
IRAS 07251−0248	0.0876	07 :27:37.544	−02:54:54.67	0.30	12.39	11.92	170±70 [*]	−550	−56	β
IRAS 08311−2459	0.1005	08:33:20.600	−25:09:33.7	0.79	12.50	12.46	70±30		163	γ
IRAS 09022−3615	0.0596	09:04:12.689	−36:27:00.76	0.55	12.29	12.09	90±30 [*]	−650	17	β
IRAS 10378+1109	0.1363	10:40:29.169	+10:53:18.29	0.30	12.31	11.85	140±60	−1300	−155	γ
IRAS 11095−0238	0.1066	11:12:03.377	−02:54:22.58	0.49	12.28	12.03	100±40		107	γ
IRAS F12072−0444	0.1286	12:09:45.132	−05:01:13.76	0.75	12.40	12.33	60±20 [*]	−1200	−51	β
IRAS F12112+0305	0.07309	12:13:45.978	+02:48:40.4	0.18	12.32	11.63	170±70 [*]	−400	−2	β
IRAS 13120−5453	0.0308	13:15:06.358	−55:09:23.23	0.33	12.24	11.83	120±50 [*]	−1200	−113	β
IRAS F13305−1739	0.1484	13:33:16.540	−17:55:10.7	0.88	12.26	12.26	23±9 [*]			β
IRAS F13451+1232	0.1217	13:47:33.425	+12:17:24.32	0.81	12.32	12.29	41±15[*]		136	β
IRAS F14348−1447	0.0830	14:37:38.317	−15:00:23.29	0.17	12.34	11.64	180±70 [*]	−900	−25	β
IRAS F14378−3651	0.068127	14:40:59.008	−37:04:31.94	0.21	12.11	11.50	100±40 [*]	−1200	−119	β
IRAS F15462−0450	0.100283	15:48:56.813	−04:59:33.61	0.61	12.21	12.05	60±20 [*]	−600:	80	β
IRAS 16090−0139	0.1336	16:11:40.432	−01:47:06.56	0.43	12.55	12.25	200±80	−1422	−332	γ
IRAS 17208−0014	0.0428	17:23:21.920	−00:17:00.7	≤ 0.05	12.39	11.15	230±90 [*]		−148	β
IRAS 19254−7245	0.06149	19:31:21.400	−72:39:18.0	0.74	12.09	12.02	32±12	−1126	−130	γ
IRAS F19297−0406	0.08573	19:32:21.250	−03:59:56.3	0.23	12.38	11.81	180±70 [*]	−1000	−119	β
IRAS 19542+1110	0.0624	19:56:35.786	+11:19:05.45	0.26	12.06	11.52	90±30 [*]	−700	−29	β
IRAS 20087−0308	0.1057	20:11:23.870	−02:59:50.7	0.20	12.42	11.79	210±80	−812	−386	γ
IRAS 20100−4156	0.1296	20:13:29.540	−41:47:34.9	0.27	12.67	12.16	340±130	−1609	−461	γ
IRAS 20414−1651	0.0871	20:44:18.213	−16:40:16.22	0.00	12.22	<11.46	170±60	−100	−101	γ
IRAS F20551−4250	0.0430	20:58:26.781	−42:39:00.20	0.57	12.05	11.87	48±19 [*]	−1200	−70	β
IRAS F22491−1808	0.0778	22:51:49.264	−17:52:23.46	0.14	12.84	12.05	590±220 [*]		−25	β
IRAS F23060+0505	0.1730	23:08:33.952	+05:21:29.76	0.78	12.53	· · ·	80±30			δ
IRAS F23128−5919	0.0446	23:15:46.749	−59:03:15.55	0.63	12.03	11.89	40±15 [*]			β
IRAS 23230−6926	0.1066	23:26:03.620	−69:10:18.8	0.32	12.37	11.93	160±60	−845	−55	γ
IRAS 23253−5415	0.1300	23:28:06.100	−53:58:31.5	0.23	12.36	11.78	180±70	−650	−134	γ
IRAS F23389+0300	0.1450	23:41:30.306	+03:17:26.44	0.23	12.13	11.54	100±40 [*]	−600	46	β
IRAS F00509+1225	0.0611	00:53:34.940	+12:41:36.0	0.90	11.95	11.96	36±14		65	β
PG 1126−041	0.0600	11:29:16.729	−04:24:07.25	0.89	11.46	11.47	3±1 [*]			β
IRAS F12243−0036	0.00708	12:26:54.620	−00:52:39.40	0.56	11.00	10.81	15±6		−63	β
PG 2130+099	0.0630	21:32:27.813	+10:08:19.46	0.92	11.71	11.76	4±2 [*]			β

Notes. (1) Source name. (2) Redshift. (3) Right ascension. (4) Declination. (5) Reported fractional contribution of the AGN to the bolometric luminosity in the reference papers ($\alpha_{AGN} = L_{AGN}/L_{bol}$). (6) Infrared luminosity (8 − 1000 μm), [*]computed using $L_{IR} = L_{bol}/1.15$ for sources retrieved from the reference paper β. (7) Reported AGN luminosity in the reference papers, derived using method 6 by Veilleux et al. (2009b), which uses the 15 to 30 μm continuum ratio (f_{30}/f_{15}) to infer α_{AGN}, resulting in uncertainties of ~20% on average for the L_{AGN} for sources retrieved from the reference paper β, similar to the method used in the reference paper γ. (8) Star formation rate, computed using SFR = $(1 − \alpha) \times 10^{-10} L_{IR}$. (9) In case of a detection of OH outflow through P-Cygni profile, the maximum velocity of the absorption feature is reported according to the reference paper. (10) The equivalent width of the OH 119 μm doublet as reported by the reference papers; a negative equivalent width implies that the absorption component is stronger than the emission component. [†] For sources taken from γ, the OH velocities have uncertainties of ±200 km s^{-1}. Sources taken from β have uncertainties typically of 50 km s^{-1}, unless the value is followed by a colon, meaning uncertainties from 50 to 150 km s^{-1}, or a double colon, meaning uncertainties larger than 150 km s^{-1}.
References. β: Veilleux et al. (2013), γ: Spoon et al. (2013).

to ~40 arcsec (in the ACA antenna configurations) for the angular resolution, and a few arcsec up to ~90 arcsec for the MAS. We do, however, pay special attention to define an aperture for extracting the total flux that is equal to or smaller than the MAS of the observation. The duplicated spectra that were discarded from our main analysis, have been nevertheless reduced and are shown in Figs. C.1–C.3.

As summarized in Table B.1, we have CO(1–0) line spectral data for 22 galaxies (20 ULIRGs and 2 LIRGs), where 21 data sets are obtained from the ALMA/ACA data archive, and one from the IRAM PdBI (analyzed by Cicone et al. 2014). CO(2–1) line observations are available for all 40 sources of the sample (36 ULIRGs and 4 LIRGs); of these, 32 galaxies were observed with APEX through PI observations, 7 have archival APEX data, and 6 have ALMA/ACA archival data. As many as 31 galaxies have CO(3–2) line coverage (30 ULIRGs and only one LIRG): 18 sources have APEX PI data, 16 have APEX archival data and 12 have ALMA/ACA archival data. Lastly, we have APEX PI

observations of the [CI](1–0) line for 17 galaxies of the sample (14 ULIRGs and 3 LIRGs), one of which resulted in a non-detection (the LIRG PG2130+099). For 7 of these sources there are also ACA archival [CI](1–0) data. Summarizing, we cover all three CO transitions for 18 galaxies (45% of the sample), two CO transitions for 17 galaxies (42% of the sample), and a single CO transition (CO(2–1)) for the remaining 5 galaxies (13% of the sample). Additionally, we probe the [CI](1–0) emission line for 16 galaxies (40% of the sample), and have an [CI](1–0) upper limit for 1 additional target. In Appendix C we discuss specific instances where additional archival data were available but have been discarded in our analysis because of poor quality and unreliable fluxes.

In the following, we describe the data reduction and analysis procedure in more detail, separately for the single-dish and interferometric data.

3.2. APEX

3.2.1. Observations

The APEX PI CO(2–1) observations for 32 sources of our sample (see Table B.1) were conducted between August and December 2019 (project ID E-0104.B-0672, PI: C. Cicone). Our observing strategy was to reach a line peak-to-rms ratio of $S/N > 5$ on the expected CO(2–1) peak flux density in velocity channels $\delta v \sim 5 - 50$ km s^{-1}. The observations of the CO(2–1) line ($\nu^{rest}_{CO(2-1)} = 230.538$ GHz) were performed with the receivers SEPIA180 and PI230 (similar frequency coverage as the ALMA Band 5 and 6 receivers), depending on the target's redshift. Both PI230 and SEPIA180 are frontend heterodyne with dual-polarization sideband-separating (2SB) receivers. The instrument PI230 can be tuned within a frequency range of $195 - 270$ GHz with an IF coverage of 8 GHz per sideband and with 8 GHz gap between the sidebands. The backends are fourth-generation fast Fourier transform spectrometers (FFTS4Gs) that consist of two sidebands, upper (USB) and lower (LSB), of 4 GHz (2x4 GHz bandwidth), which leads to the total bandwidth of $\Delta \nu = 8$GHz[2]. The instrument SEPIA180 covers a frequency range from $159-211$ GHz. For this instrument, the backends are the eXtended bandwidth fast Fourier transform Spectrometers (XFFTSs), which also consist of two sidebands, upper and lower, each covering 4–8 GHz, for a total of $\Delta \nu = 16$GHz IF bandwidth. Both receivers have an average noise temperature (T_{rx}) of ~55 K (Belitsky et al. 2018).

Each sideband spectral window covered 4 GHz and was divided into 65 536 (64k) channels, resulting in a resolution of ~61kHz, which corresponds to ~80−95ms^{-1} in velocity units at the range of redshifts covered by our sample. The CO(2–1) emission line was placed in the LSB and the telescope was tuned to the expected CO(2–1) observed frequency for each source computed by using previously known optical redshifts (see Table 1). All our PI observations were performed in the wobbler-switching symmetric mode with 60″ chopping amplitude and a chopping rate of $R = 0.5$Hz. The data were calibrated using standard methods. The on-source integration times (without overheads) varied from source to source and were calculated using the APEX Observing Time Calculator tool[3], and are reported in Table B.2. During the observing runs, the PWV varied from $0.8 < \text{PWV[mm]} < 3$.

APEX PI CO(3–2) observations were obtained between October and December 2020 (project ID E-0106.B-0674, PI: I. Montoya Arroyave). In this case, our observing strategy was to reach a line peak-to-rms ratio of $S/N \sim 7$ on the expected CO(3–2) peak flux density in velocity channels $\delta v \sim 50-100$ km s^{-1}. These CO(3–2) observations ($\nu^{rest}_{CO(3-2)} = 345.796$ GHz) were carried out with the SEPIA345 receiver, which has a frequency coverage similar to ALMA Band 7. The instrument SEPIA345, similar to SEPIA180, is a frontend heterodyne with dual-polarization 2SB receiver and works with an XFFTS backend. It can be tuned within a frequency range of $272-376$ GHz and it has two IF outputs per polarization (two sidebands: USB and LSB), each covering 4–12 GHz, leading to a total of up to $\Delta \nu = 32$ GHz IF bandwidth (Meledin et al. 2022). Each sideband spectral window covered 8 GHz and was divided into 4096 channels. Initially, the requested resolution was for 65536 (64k) channels (~122 kHz per channel), corresponding to ~107−126ms^{-1}; however, due to the necessity of performing remote operations during the pandemic and to the limited band for transferring data, we applied a spectral binning at the acquisition stage so that the data could be transferred quickly to Europe after acquisition. This however did not affect the scientific output, since these extragalactic targets are characterized by broad emission lines and the new spectral resolution of ~1953kHz (~1.7 − 2kms^{-1}) was still very high for our science goals. The CO(3–2) emission line was placed in the LSB, and the tuning frequency was the expected CO(3–2) observed frequency plus 2 GHz: by doing so, we centered the line at IF = 8 GHz (center of sideband), rather than at IF = 6 GHz (center of backend unit) in order to have better sampling of the baselines on both sides of the line. Observations were performed in the wobbler-switching symmetric mode with 100″ chopping amplitude and a chopping rate of $R = 0.5$Hz, and we adopted standard calibration. The on-source integration times (calculated similarly as for the CO(2–1) observations) are reported in Table B.2. During the observing runs, the PWV varied from $0.7 < \text{PWV[mm]} < 2.5$.

The [CI](1–0) APEX PI observations were obtained between October 2020 and June 2021 (project ID E-0104.B-0672, PI: C. Cicone). Our observing strategy for the atomic carbon line was to reach a S/N peak-to-rms of ~5 on the expected [CI](1–0) peak flux density in velocity channels $\delta v \sim 25-100$ km s^{-1}. The expected [CI](1–0) line flux was conservatively estimated by assuming $L'_{[CI](1-0)}/L'_{CO(1-0)} = 0.2$, that is, the lowest value observed in NGC 6240 by Cicone et al. (2018), which turned out to be a reasonable assumption. The [CI](1–0) line observations ($\nu^{rest}_{[CI](1-0)} = 492.161$ GHz) were carried out with nFLASH460, which covers a similar frequency range as the ALMA Band 8 receiver. The instrument nFLASH460 is a frontend heterodyne with dual-polarization 2SB receiver with instantaneous coverage in two bands (USB and LSB) of 4 GHz each, where the separation between the center of the two sidebands is 12 GHz. It covers the frequency window between 378 and 508 GHz, and works with a fast Fourier transform spectrometer backend in each sideband. For our observations, each sideband spectral window covered 4 GHz and were divided into 65 536 (64k) channels (~61 kHz per channel), corresponding to a resolution of ~37 − 44 m s^{-1} in velocity units at the range of redshifts covered by our sample. The telescope was tuned to the expected [CI](1–0) observed frequency for each source, with wobbler-switching symmetric mode with 60″ chopping amplitude and a chopping rate of $R = 0.5$Hz. The data were calibrated using standard procedures. The observing times, computed similarly as for CO(2–1) and CO(3–2), are reported in

---

[2] https://www.eso.org/sci/facilities/apex/cfp/cfp104/recent-changes.html
[3] https://www.apex-telescope.org/heterodyne/calculator/

Table B.2. During the observing runs, the PWV varied from $0.3 < \text{PWV[mm]} < 1.0$.

Additionally, we used APEX archival CO(2–1) and CO(3–2) data for part of the sample, from different projects with observing dates ranging from 2010 to 2017, using the SHeFI and nFLASH receivers. All project codes of the archival data sets used throughout this work are also reported in Table B.1. The APEX archival CO(2–1) observations used in this paper have an average $S/N \sim 5$, while APEX CO(3–2) archival observations reach an average $S/N \sim 3–5$ (computed peak-to-rms with $\delta v \sim 50$ km s^{-1} channels).

For all single-dish data, PI and archival, we adopted the same reduction and analysis steps, which are described below in Sect. 3.2.2.

3.2.2. Data reduction

For the reduction of the APEX data sets we used the `GILDAS/CLASS` software package[4], and applied the following four steps to all science targets.

First, after collecting all spectral scans of interest for a given target and transition (which could have different observing dates), we checked all scans individually, and discarded those affected by baseline instabilities and instrumental features following a similar procedure to Cicone et al. (2017). At the time of our APEX PI CO(2–1) observations, we found that the receiver SEPIA180 had slightly more stable baselines than PI230. For PI230, we verified that one of the polarization windows was heavily affected by standing waves, which led to discarding an average of 40% of sub-scans in that polarization. In the worst cases, this polarization window had to be discarded completely, therefore effectively cutting the integration time by half. For the SEPIA180 instrument, the average percentage of discarded scans was ~20%. For the PI SEPIA345 CO(3–2) observations, the average percentage of discarded scans was 25% (an additional flagging was performed at the edge of the window to compensate for platforming issues). The nFLASH460 [CI](1–0) observations were heavily affected by instrumental features and/or sky-lines (more common at these high frequencies) and therefore the average fraction of discarded scans was ~50% for most sources.

Second, we collected all the selected sub-scans corresponding to a given source and transition, and fitted and subtracted a linear baseline from each sub-scan after masking the central $v \in (-500, 500)$ km s^{-1} in order to avoid the expected line emission. We then averaged together all baseline-subtracted scans to produce a high S/N spectrum for each source.

Third, we smoothed the combined spectrum to a common velocity bin of $\delta v \approx 50$ km s^{-1}. We fitted and subtracted a final linear baseline by using the same masking of the central $v \in (-500, 500)$ km s^{-1}. We fitted a single Gaussian function to the spectrum and, based on the result, we refined the central masking adjusting it to the width of the detected line emission. For the non-detections, we kept the initial mask ($v \in (-500, 500)$ km s^{-1}). These spectra were binned to $\delta v \approx 50$ km s^{-1} resolution to compute the rms values reported in Table B.2.

Lastly, we produced the final spectrum to be used in the spectral analysis. For all the galaxies, the spectrum was extracted with a resolution of $\delta v \approx 5$ km s^{-1}, in order to allow for further smoothing, if needed, in the spectral fitting stage. The final spectrum was imported into Python[5], where we performed the remaining analysis.

The output signal from the APEX telescope corresponds to the antenna temperature corrected for atmospheric losses, T_A^* in [K], and it must be multiplied by a calibration factor (or telescope efficiency) in order to obtain the flux density in units of Jansky [Jy]. Both for PI230 and SEPIA180 the average Kelvin to Jansky conversion factor measured during our observation period is ~36 ± 3 Jy K^{-1}, for SEPIA345 it is ~37.5 ± 3 Jy K^{-1} and for nFLASH460 it is ~58 ± 5 Jy K^{-1}. For the archival data, the calibration factor used for CO(2–1) observations was ~39 ± 5 Jy K^{-1} and ~46.5 ± 7 Jy K^{-1} for CO(3–2) observations.

3.3. ALMA and ACA

The archival data used here have observing dates ranging from 2012 to 2018. They use different antenna configurations of the 12 m (ALMA) and 7 m (ACA) arrays, corresponding to different angular resolutions and different MAS. All the project IDs used in this work are reported in Table B.1. We performed calibration and imaging using the Common Astronomy Software Applications (CASA) package[6]. The calibrated measurement sets (MSs) of data sets older than 2018 were provided by the European Southern Observatory (ESO) ALMA helpdesk. For the newer data obtained after 2018, we retrieved the MS by running the CASA pipeline (version `5.6.1`) and executing the calibration script provided with each corresponding data set.

We then analyzed the MS within `CASA 5.6.1` and separated the spectral windows including the lines of interest (i.e., CO(1–0), CO(2–1), CO(3–2) or [CI](1–0), depending on the data set), using the task `split`. A first deconvolution and cleaning were performed in interactive mode with the task `tclean`, by adapting the mask to the source size. This first clean provided us with an initial datacube that we used to identify the line-free channels for continuum subtraction, and to optimize the parameters for the final clean. We ran the cleaning process until reaching uniform residuals, and produced an image of the source in which we measured the noise level. We then performed the continuum subtraction using the task `uvcontsub`, by fitting a first-order polynomial and estimating the continuum emission in the line-free frequency ranges previously identified. We produced the final data cube using once again the task `tclean` on the continuum-subtracted MS file. We constructed all image cubes with the highest spectral resolution available, ranging from $\Delta v \sim 1$ to ~10 km s^{-1}, depending on the data set. Final cubes are obtained using Briggs weighting with robust parameter equal to 0.5 and primary-beam corrected. We extracted the final spectrum from a circular aperture that is size-matched to maximize the recovered flux. The apertures used for spectra extraction are reported in Table B.2. For the sources where only high-resolution ALMA observations were available (IRAS F01572+0009 and IRAS F12072−0444), we applied an *uv* tapering to enhance the sensitivity to extended structures. This however does not overcome the possible issue of missing flux from faint extended structures due to poor sampling of short *uv* baselines.

The spectra are exported from CASA in flux density [Jy] units, extracted in suitable format and imported into Python for further analysis. The quoted errors refer to the systematic errors on the absolute flux calibration of ALMA/ACA data (estimated to be 5% for Band 3 data and 10% for Bands 6–8 data, and typically the dominant source of error in the data used in this study), added in quadrature to the statistical rms of the spectra.

---

4. Methodology

4.1. Spectral line fitting

Our analysis is aimed at deriving source-averaged line ratios for different kinematic components of the molecular and atomic ISM in local (U)LIRGs. We also want to investigate possible statistical trends between the molecular (CO and [CI]) line ratios as a function of the central velocity v and line width σ_v of the different components, to understand whether broader and/or higher-v H$_2$ gas components are the origins for the extremely high global CO excitation previously found in (U)LIRGs (e.g., Papadopoulos et al. 2012), which Cicone et al. (2018) suggested based on their pilot study on NGC 6240.

We base the analysis reported in this paper exclusively on total (i.e., galaxy-integrated) molecular line spectra, and on the results of a multi-Gaussian spectral fitting of the CO and [CI](1–0) lines. We acknowledge that, without spatially resolved information, it is not possible to link in a straightforward way the different (e.g., broad or narrow) spectral line components to outflowing or non-outflowing gas. However, performing such a classification is not needed in our case, because we can rely on a large, statistically significant sample. Indeed, we are interested in studying in a statistical sense any trends observed between molecular line ratios and the central velocity (v) and/or velocity dispersion (σ_v) of the different spectral components. Once the presence of statistical correlations is assessed (independently of any arbitrary classification of such components in terms of outflow or disk), we can interpret the results by assuming that, in this sample of (U)LIRGs, the line luminosities of high-σ_v and/or high-v spectral components are more likely to be dominated by molecular gas embedded in outflows compared to the low-σ_v and low-v components. Such an assumption would be supported by (i) the results of the pilot study on NGC 6240 (see Cicone et al. 2018), (ii) the unambiguous detection of OH119 μm outflows in most targets (Sturm et al. 2011; Veilleux et al. 2013; Spoon et al. 2013), and (iii) the widespread evidence for high-velocity molecular outflows in local (U)LIRGs reported in the recent literature (see the review by Veilleux et al. 2020).

After having clarified our strategy, we now describe our spectral fitting procedure. We used `mpfit` for Python[7]. This tool uses the Levenberg-Marquardt technique to solve the least-squares problem in order to fit a user-supplied function (the model) to the user-supplied data points (the data). Spectral lines were modeled using single or multiple Gaussian profiles characterized by an amplitude, a peak position (v_{cen}), and velocity dispersion (σ_v, or, equivalently, the full width at half maximum, FWHM). Having multiple CO transitions allows us to partially break any degeneracy in the spectral line decomposition with Gaussian functions. We therefore fitted simultaneously all CO transitions available for each source, by constraining the v_{cen} and σ_v of the Gaussian components to be equal in all CO transitions, allowing only their amplitudes to vary freely in the fit. We allowed the fit to use up to a maximum of three Gaussian functions to reproduce the observed global line profiles, so that line asymmetries and broad wings are properly captured with separate spectral components when the S/N is high enough (see for example IRAS 13120-5453 in Fig. B.2). For all the fits, we verified using a reduced χ^2 criterion that a fourth Gaussian component was not required for any of the sources, with the data at hand. In those cases where the statistical criterion (reduced χ^2) does not indicate a clear preference between a fit performed with one, two, or three Gaussians,

we performed a visual inspection of the fit. For the low S/N spectra (e.g., $S/N \sim 3$) without clear asymmetries, we used only one Gaussian component, in order not to over-fit the data.

The fitting procedure for the [CI](1–0) line spectra is carried out separately from the CO lines due to their overall lower S/N. Furthermore, by doing so, we can avoid assuming a priori that the atomic carbon and CO lines trace the same gas clouds and share the same kinematics. This assumption will be tested and discussed in Sect. 5.1.2.

The final fits for all sources and transitions are shown in Figs. B.1–B.6, where the spectral transitions are color-coded. Based on the fit results, we computed velocity-integrated line fluxes for both the individual Gaussian components and the entire line profiles, and the latter are reported in Table D.1. As a sanity check, we verified that the total line fluxes measured through the fit (by adding up the individual Gaussians) are consistent with the total line fluxes calculated by directly integrating the spectra within $v \in (-1000, 1000)$ km s^{-1}, after setting a threshold of $>2\sigma$ for each channel. We find the values to be consistent within the errors, and therefore using either value will not affect the analysis performed throughout our work.

4.2. Line luminosities and ratios

We calculated the CO and [CI] line luminosities from the integrated line fluxes following the definition from Solomon et al. (1997):

$$L'_{line} \,[\mathrm{K\,km\,s^{-1}\,pc^2}] = 3.25 \times 10^7 \frac{D_L^2}{\nu_{obs}^2 (1+z)^3} \int S_\nu \, d\nu, \qquad (1)$$

where D_L is the luminosity distance measured in [Mpc], ν_{obs} is the corresponding observed frequency in [GHz], and $\int S_\nu \, d\nu$ is the total integrated line flux in [Jy km s^{-1}]. In Table D.1 we report the total integrated fluxes and respective luminosities calculated for the different transitions. The CO line ratios are defined as

$$
\begin{aligned}
r_{21} &= L'_{CO(2-1)}/L'_{CO(1-0)} \\
r_{31} &= L'_{CO(3-2)}/L'_{CO(1-0)} \qquad\qquad (2)\\
r_{32} &= L'_{CO(3-2)}/L'_{CO(2-1)}.
\end{aligned}
$$

In our analysis we use both the global CO line luminosity ratios as well as those computed for individual Gaussian components. Additionally, we calculate global [CI](1–0)/CO(1–0) line luminosity ratios, as

$$r_{CICO} = L'_{[CI](1-0)}/L'_{CO(1-0)}. \qquad (3)$$

Line ratios were computed for all combinations of lines and sources where the individual line luminosity measurements pass a loose criterion of $S/N > 1$, in order not to penalize cases where one of the two lines is constrained at very high significance. As a result, some line ratios have very large error bars, which are taken into account in our analysis.

5. Results

5.1. Atomic carbon as an alternative gas tracer

5.1.1. A tight relation between CO(1–0) and [CI](1–0) luminosities

In Fig. 1 we plotted the measured total CO(1–0) and CO(2–1) line luminosities as a function of [CI](1–0) line luminosity, for

---

[7] Open-source algorithm adapted from the IDL version; see https://github.com/segasai/astrolibpy/blob/master/mpfit/
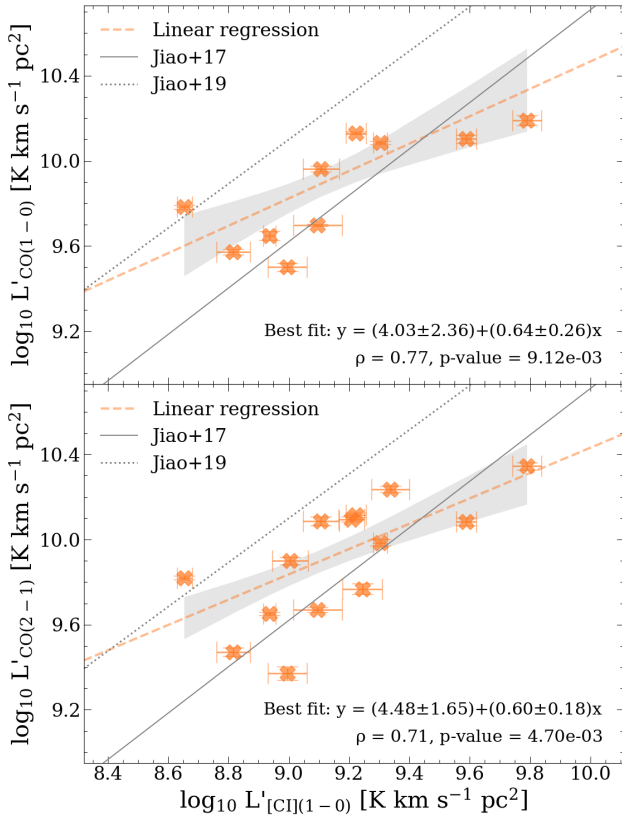
Fig. 1. CO(1–0) vs. [CI](1–0) luminosity (top) and CO(2–1) vs. [CI](1–0) luminosity (bottom) for the ULIRGs in our sample. The best-fit relations are shown as dashed orange lines. The best-fit parameters are reported at the bottom-right corner of the plots. We also display the Pearson correlation coefficients (ρ) and their associated p-values. The solid black lines in both panels represent the corresponding relations reported by Jiao et al. (2017) for a sample of 71 (U)LIRGs, and the dotted lines represent the relations of Jiao et al. (2019) for a sample of 15 nearby spiral galaxies, between $L'_{CO(1-0)}$ and $L'_{[CI](1-0)}$.

the ULIRGs in our sample. The relation with CO(3–2) was not studied as this line starts to trace denser and more excited H_2 gas rather than the global molecular reservoir, while we are interested in exploring the potential of [CI](1–0) to probe similar regions as the CO J_{up} = 2, 1 transitions.

The plots in Fig. 1 show that $L'_{CO(1-0)}$ and $L'_{CO(2-1)}$ are both tightly correlated with $L'_{[CI](1-0)}$, showing Pearson correlation coefficients (ρ) equal to 0.77 and 0.71, and p-values of 9.1×10^{-3} and 4.7×10^{-3}, respectively, for $L'_{CO(1-0)}$ and $L'_{CO(2-1)}$. We performed a fit to the relation between $L'_{CO(1-0)}$ and $L'_{[CI](1-0)}$ using least squares, which gives

$$\log_{10} L'_{CO(1-0)} = (4.03 \pm 2.36) + (0.64 \pm 0.26) \log_{10} L'_{[CI](1-0)}. \quad (4)$$

We performed a similar fit with the CO(2–1) line, whose results are reported on the corresponding plot. We find that $L'_{CO(1-0)}$ and $L'_{CO(2-1)}$ follow very similar relations as a function of $L'_{[CI](1-0)}$, with variations in the best-fit parameters within one standard deviation.

In Fig. 1 we also report the relation found by Jiao et al. (2017) in a study of unresolved neutral carbon emission in a sample of 71 (U)LIRGs based on *Herschel* observations, for which they derive a best-fit relation of $\log_{10} L'_{CO(1-0)} = (-0.19 \pm 1.26) + (1.09 \pm 0.15) \log_{10} L'_{[CI](1-0)}$. In a similar study performed on 15 nearby spiral galaxies with spatially resolved *Herschel* data,

Jiao et al. (2019) obtain: $\log_{10} L'_{CO(1-0)} = (0.74 \pm 0.12) + (1.04 \pm 0.02) \log_{10} L'_{[CI](1-0)}$. Our best-fit $L'_{[CI](1-0)}$ versus $L'_{CO(1-0)}$ relation has a flatter slope than the one found by Jiao et al. (2017), likely due to our sample only covering a narrower dynamic range in luminosities than the sample in Jiao et al. (2017), while our sources are exclusively ULIRGs, the Jiao et al. (2017) sample is heavily dominated by LIRGs (62 LIRGs and only 9 ULIRGs). When we explore the same relations in our extended sample (including the LIRGs), shown in Fig. A.1, we find that the best-fit relation between $L'_{[CI](1-0)}$ and $L'_{CO(1-0)}$ ($\log_{10} L'_{CO(1-0)} = (-0.45 \pm 0.73) + (1.13 \pm 0.08) \log_{10} L'_{[CI](1-0)}$) is almost linear and well in agreement with that obtained by Jiao et al. (2017) and clearly shifted to higher $L'_{[CI](1-0)}/L'_{CO(1-0)}$ ratios with respect to the Jiao et al. (2019) fit performed on non-infrared luminous local galaxies. Such a difference in $L'_{[CI](1-0)}/L'_{CO(1-0)}$ ratios between (U)LIRGs and other galaxies is further explored in Sect. 5.6.

The tight correlations in Fig. 1 suggest that the CO(1–0) and CO(2–1) lines arise from similar regions as the [CI](1–0) emission, at least when averaged over galactic scales, and strengthen the hypothesis (see, e.g., Papadopoulos et al. 2004) that the [CI](1–0) line is an excellent molecular gas tracer, and a valid alternative to low-J CO line emission.

5.1.2. Comparison between CO and [CI] line widths

In the previous section we find a tight relation between the [CI](1–0) and CO total line luminosities for ULIRGs (which becomes almost linear when expanding the dynamic range in luminosity values by including the LIRGs). Here we test whether the two tracers share the same kinematics. We compared the line widths using the CO(2–1) and the [CI](1–0) lines. We preferred CO(2–1) over CO(1–0) to maximize the sample size, since CO(2–1) spectra are available for all 16 sources with a [CI](1–0) detection.

We used two different approaches to study the line widths of the two tracers. Firstly, we performed a dedicated, single Gaussian spectral fit, run independently for each line. Secondly, we computed the 16–84 ($v_{84} - v_{16}$) and 2.3–97.7 ($v_{97.7} - v_{2.3}$) percentile velocity intervals, derived from the analytical form of the overall best-fit line profile obtained by a multi-Gaussian fit. The latter approach is likely a more robust method when dealing with complex line profiles, as is the case for some of the sources in our sample, for example IRAS 19254–7245.

The results are shown in Fig. 2. The plot of $\sigma_{v,[CI]}$ versus $\sigma_{v,CO}$ obtained through a single Gaussian fit is plotted on the top panel of Fig. 2, while the percentile velocity plots obtained using the second approach are shown in the bottom panels of Fig. 2. We find that the sources characterized by broader profiles sit preferentially below the 1:1 relation. The best-fit relations obtained through a least squares regression analysis have a slope below unity.

As an additional test, we over-plotted in Fig. 2 the values obtained for NGC 6240, which is a source characterized by an extremely turbulent ISM, strongly affected by outflows. The purple pentagon represents the total measurement available for NGC 6240, computed from spectra extracted from a $12'' \times 6''$ rectangular aperture encompassing the nuclei and the molecular outflow, while the pink dot represents the central $2'' \times 2''$ region (for a more in depth explanation of how the apertures are defined, see Cicone et al. 2018). Quite strikingly, both NGC 6240 data points sit on the best-fit relation obtained for our sample when probing the core of the lines via σ_v and $v_{84} - v_{16}$. Instead, as
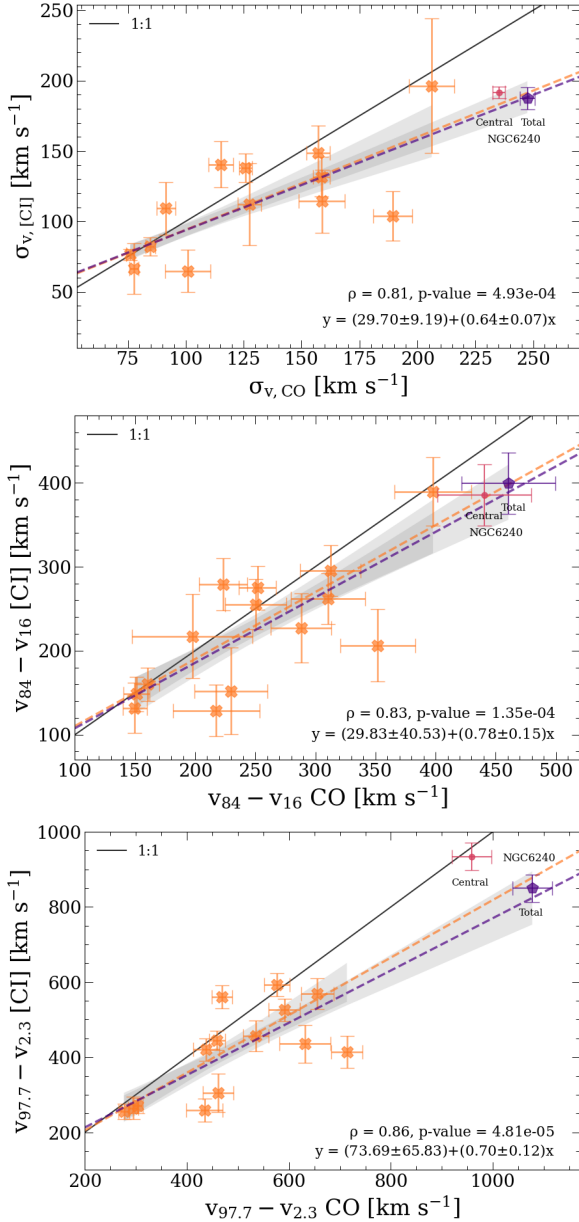
Fig. 2. [CI](1–0) line width as a function of the CO(2–1) line width. Top panel: Velocity dispersion (σ_v) obtained via a single Gaussian spectral fit to the [CI](1–0) and CO(2–1) emission lines. Middle and bottom panels: 16–84 ($v_{84} - v_{16}$) and 2.3–97.7 ($v_{97.7} - v_{2.3}$) percentile velocity intervals for CO and [CI], respectively, derived from the best-fit function obtained from the multi-Gaussian fit. Orange data points correspond to the ULIRGs sample analyzed in this work. The purple pentagon and the pink dot represent the values obtained for NGC 6240, respectively for the total region and for the inner $\sim 2''$ (see Cicone et al. 2018, and the text in Sect. 5.1.2 for a more detailed explanation of the apertures used for spectra extraction). The solid black line indicates the 1:1 relation. The dashed orange line shows the best-fit relation obtained using only our sample, while the dashed purple line is the best-fit relation obtained for our sample plus NGC6240 (total). The shaded gray areas corresponds to the 1σ confidence interval of the two fits. At the bottom-right corner we report the Pearson correlation coefficient (ρ) and the p-values, as well as the best-fit coefficients of the purple fit.

we probe more toward the high-velocity wings of the line by using, e.g., the $v_{97.7} - v_{2.3}$ values, the nuclear spectrum results to be more consistent with the 1:1 relation between [CI] and CO line width, while the total spectrum of NGC 6240, including the

extended outflows, sits on the best-fit relation obtained from the analysis of the other sources. The fact that the total spectrum includes more of the extended outflow than the nuclear one (see Cicone et al. 2018), and is also the one that departs more from the 1:1 relation, may indicate that this deviation (i.e., a narrower width of [CI] with respect to CO) is accentuated by the inclusion of diffuse outflowing gas.

The fit that includes the total emission from NGC 6240 displayed in the top panel of Fig. 2 which is consistent with the one obtained from our sample alone, is

$$\sigma_{v,[CI]} = (30 \pm 9) + (0.64 \pm 0.07)\,\sigma_{v,CO}\,, \tag{5}$$

and the corresponding fit for the $v_{97.7} - v_{2.3}$ velocity percentiles (shown in the bottom panel) is

$$v_{97.7} - v_{2.3}\,[CI] = (74 \pm 66) + (0.70 \pm 0.12)\,v_{97.7} - v_{2.3}\,CO\,. \tag{6}$$

Therefore, our data indicate that the [CI](1–0) line is narrower than CO(2–1). The average line width ratio is $\langle \sigma_{v,[CI]}/\sigma_{v,CO} \rangle = \langle r_\sigma \rangle = 0.91 \pm 0.07$, computed using all sources. The ratios below unity are driven by targets with $\sigma_{v,CO} > 150$ km s^{-1}, while those with $\sigma_{v,CO} \lesssim 150$ km s^{-1}, which represents the majority of our sample, are consistent with the 1:1 relation.

Few comparisons of CO and [CI] line widths can be found in the literature, and most of these previous studies report a 1:1 correspondence between the line widths. Michiyama et al. (2021), by comparing ACA CO(4–3) and [CI](1–0) observations of a sample of 36 local (U)LIRGs, found a 1:1 relation between the FWHMs of the two transitions. However, their analysis excludes sources with complex profiles (e.g., double peak emission), which we did not do. Similarly, Bothwell et al. (2017) analyzed ALMA [CI](1–0) emission line observations in a sample of strongly lensed dusty star-forming galaxies spanning a wide redshift range of $2 < z < 5$, and for 11 of such sources they compared [CI] and CO(2–1) line widths, using literature CO data. Their results are consistent with a 1:1 relation. In Sect. 6 we discuss possible explanations for the difference in CO and [CI] line widths observed in our sample and specifically in the high-σ_v (U)LIRGs.

5.2. Molecular gas mass estimates and the CO-to-H₂ factor

Building upon Sect. 5.1.1, we use the [CI](1–0) and CO(1–0) emission lines to derive independent estimates of the molecular gas mass (M_{mol}) of the ULIRGs of our sample. We also use the [CI]-based M_{mol} to derive an average value for the α_{CO} factor, similarly to Cicone et al. (2018).

Both tracers rely on calibration factors in order to compute M_{mol}. For [CI](1–0)-based estimates, we need to assume the optically thin condition (which applies to most extragalactic environments), a value for the [CI] abundance with respect to H₂ ($X_{CI} = [C/H_2]$), and a value for the parameter Q_{10} (i.e., the [CI] excitation factor). The molecular hydrogen gas mass can then be computed, following Dunne et al. (2021), as

$$M_{mol,[CI]}[M_\odot] = 1.36\,\frac{(9.51 \times 10^{-5})}{X_{CI}\,Q_{10}}\,L'_{[CI](1-0)}. \tag{7}$$

For CO-based mass measurements, we need to assume an α_{CO} factor:

$$M_{mol,CO}[M_\odot] = \alpha_{CO}\,L'_{CO(1-0)}. \tag{8}$$

Both Eqs. (7) and (8) include the Helium contribution to the molecular gas mass through a multiplicative factor of 1.36.
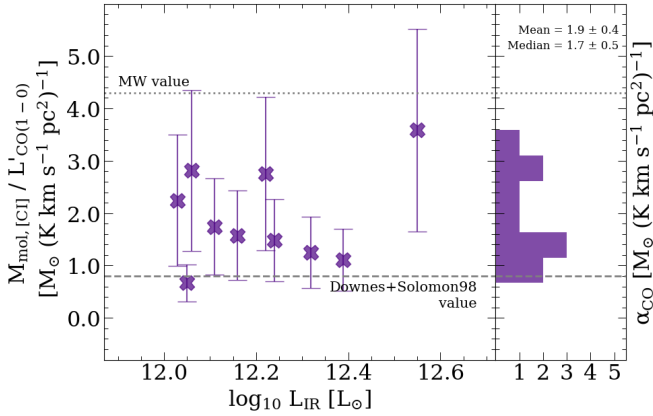
Fig. 3. Ratio between [CI]-based molecular gas mass estimates and CO(1–0) line luminosity, computed for the ULIRGs in our sample that have both lines available, and plotted as a function of the infrared luminosity. This ratio is interpreted as the α_{CO} factor (see Eq. (10)). The right part of the plot shows the resulting distribution of [CI]-based α_{CO} values. The dotted line indicates the CO-to-H$_2$ conversion factor for the Milky Way, and the dashed line corresponds to the value commonly used in the literature for (U)LIRGs (Downes & Solomon 1998). The mean and median values obtained for our sample (reported at the top-right corner) are $\alpha_{CO} = 1.9 \pm 0.4\,M_\odot$ and $1.7 \pm 0.5\,M_\odot$ (K km s^{-1} pc^2)$^{-1}$, respectively.

All tracers of H$_2$ are affected by uncertainties. Using CO and an arbitrary α_{CO} value can introduce large errors in the computed M_{mol} due to its sensitivity to metallicity in a nonlinear fashion, and to the turbulence and kinematics of the CO-emitting clouds that affect the global optical depth of galaxy-averaged CO measurements. In the case of [CI], different combinations of X_{CI} and Q_{10} may yield different results; X_{CI} may be the easiest parameter to model in terms of the ISM conditions if in fact the C^0 abundance is determined by CRs (e.g., Bisbas et al. 2015; Dunne et al. 2021). In the following Sects. 5.2.1 and 5.2.2, we discuss separately the [CI]-based and CO-based M_{mol} estimates.

5.2.1. [CI]-based M_{mol} estimates

We compute $M_{mol,[CI]}$ using the [CI](1–0) luminosities reported in Table D.1 and Eq. (7). We adopt a carbon abundance of $X_{CI} = (3.0 \pm 1.5) \times 10^{-5}$, which is an appropriate value for local star-forming galaxies and has been used by several previous studies (e.g., Weiß et al. 2005; Papadopoulos et al. 2004; Walter et al. 2011; Jiao et al. 2017; Cicone et al. 2018). For the [CI] excitation factor Q_{10}, we adopt a value of 0.48 (with <16% variation), following the prescriptions by Papadopoulos et al. (2022), who find that, for the most expected average ISM conditions in galaxies ($n_{H_2} = [300 - 10^4]$ cm^{-3} and $T_{kin} = [25 - 80]$ K), the [CI] lines are globally sub-thermally excited.

By defining a parameter $\alpha_{[CI]}$ analogous to α_{CO} to represent a [CI](1–0)-to-H$_2$ conversion factor, we can rewrite Eq. (7) as

$$M_{mol,[CI]} = \alpha_{[CI]} L'_{[CI](1-0)}$$
$$\text{with } \alpha_{[CI]} = 1.293 \times 10^{-4}(X_{CI}Q_{10})^{-1}. \quad (9)$$

And thus, plugging in our assumptions for the X_{CI} and Q_{10} values, we obtain $\alpha_{[CI]} = 9.0\,M_\odot$ (K km s^{-1} pc^2)$^{-1}$.

The [CI]-based M_{mol} values can then be used to infer α_{CO} as follows:

$$\alpha_{CO} = M_{mol,[CI]}/L'_{CO(1-0)}. \quad (10)$$

The ratio $M_{mol,[CI]}/L'_{CO(1-0)}$, which in practice represents the α_{CO} factor required to force agreement between [CI]- and CO-based H$_2$ mass estimates, is plotted in Fig. 3 against the infrared luminosity, for the 10 ULIRGs with available CO(1–0) and [CI](1–0) detections. The distribution of the resulting α_{CO} values is also shown on the right of Fig. 3.

Figure 3 demonstrates that 9 out of 10 targets require an α_{CO} value higher than the one commonly assumed for (U)LIRGs of 0.8 $M_\odot$ (Kkms^{-1}pc^2)$^{-1}$, see Downes & Solomon (1998). The mean value measured for our sample is $1.9 \pm 0.4\,M_\odot$, and the median value is 1.7 $M_\odot$ (K km s^{-1} pc^2)$^{-1}$, with 16–84 velocity percentile equal to $1.2 - 2.8$ (K km s^{-1} pc^2)$^{-1}$. Our results are consistent with the dust-based α_{CO} estimate equal to $1.8^{+1.3}_{-0.8}\,M_\odot$ (K km s^{-1} pc^2)$^{-1}$) derived by Herrero-Illana et al. (2019) for 55 (U)LIRGs from the Great Observatories All-sky LIRG survey (GOALS). These authors estimate first the dust mass (M_{dust}) from a FIR spectral energy distribution (SED) fit using *Herschel* data, following the strategy proposed by Scoville et al. (2016) of fixing $T_{dust} = 25$ K for every source, and then estimate α_{CO} by requiring that the gas-to-dust mass ratio of (U)LIRGs matches the one of local star-forming spirals. Similarly, a study performed by Kawana et al. (2022) on a nearby LIRG (NGC 3110) estimates an α_{CO} value of 1.7 $\pm$ 0.5 $M_\odot$ (K km s^{-1} pc^2)$^{-1}$ based on thermal dust continuum emission and assuming that the dust and the rotational temperature of the CO molecule are equal.

In Appendix A we extend the calculations to include the LIRGs in our sample with available [CI](1–0) and CO(1–0) data (i.e., two additional sources; see Fig. A.2). The resulting mean and median values are perfectly consistent with the ones obtained in Fig. 3.

5.2.2. CO-based M_{mol} estimates

We then use the lowest-J CO transition available for each source to estimate a CO-based total molecular gas mass. For sources without CO(1–0) data, we first estimate $L'_{CO(1-0)}$ based on the $L'_{CO(2-1)}$ transition, which is available for the whole sample. We assume a line ratio of $r_{21} = 1.1 \pm 0.4$, which is the median value computed in this work based on the data available in our sample (see Sect. 5.4 and Fig. 6). We then proceed to compute $M_{mol,CO}$ using Eq. (8). We compute $M_{mol,CO}$ using three different α_{CO} values, namely, 4.3, 0.8 and 1.7 $M_\odot$ (Kkms^{-1}pc^2)$^{-1}$, corresponding to the value measured for the Milky Way galaxy (Bolatto et al. 2013), the value commonly employed in the past for (U)LIRGs (Downes & Solomon 1998), and the median value obtained for our sample using the [CI]-based method described previously (see Sect. 5.2.1).

In Fig. 4 we show the comparison between the [CI]-based M_{mol} values, and the CO-based M_{mol} estimates obtained using different conversion factors. These plots report the same result as Fig. 3 (i.e., the α_{CO} value), but visualized in a different way and including the uncertainties. For each relation we perform two linear fits, one with a free-varying slope and another with a slope fixed to unity. The 1:1 relation is also over-plotted using a dotted black line. The plots in Fig. 4 show clearly that an $\alpha_{CO} = 4.3\,M_\odot$ (Kkms^{-1}pc^2)$^{-1}$ overestimates the M_{mol}, while an $\alpha_{CO} = 0.8\,M_\odot$ (Kkms^{-1}pc^2)$^{-1}$ underestimates it, for all ULIRGs of the sample. Instead, as is obvious from the definition, the value of $\alpha_{CO} = 1.7\,M_\odot$ (Kkms^{-1}pc^2)$^{-1}$, which is the median of the individual [CI]-based α_{CO} values estimated in the previous section, brings all data points closer to the 1:1 relation. We note, however, that this is an average value for the CO-to-H$_2$ conversion factor, and it is most likely to vary from galaxy to
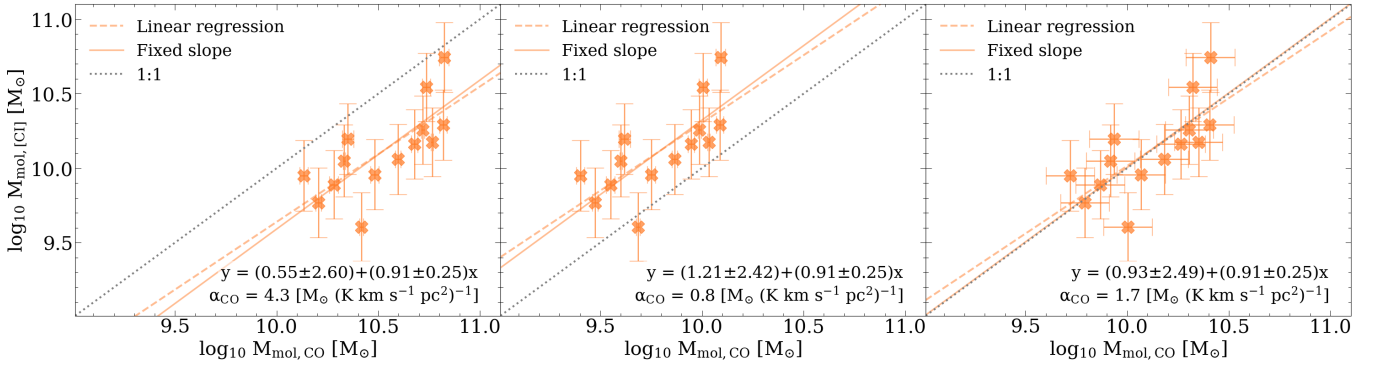
Fig. 4. [CI]-based $M_{\rm mol}$ vs. CO-based $M_{\rm mol}$ values obtained with different $\alpha_{\rm CO}$ assumptions (0.8, 4.3, and 1.7 $M_\odot$ (Kkms^{-1}pc^2)$^{-1}$). The best-fit linear relation with a free-varying slope is shown as a dashed orange line, and the best-fit parameters are reported at the bottom-right corner of each plot. The solid orange line shows the best-fit relation obtained by fixing the slope to unity, and the 1:1 relation is reported as a dotted black line.

galaxy (as shown by a few outliers visible in Fig. 4), as well as a function of aperture size and spatial scales probed. This variability averages out on galaxy-averaged measurements leading to a typical value corresponding to the dominant radiation-emitting regions within the galaxy. We note that large uncertainties on empirically estimated $\alpha_{\rm CO}$ values are still expected, as there are many factors that may impact on its value, for example density, temperature, metallicity, and optical depth. These results are however reassuring and indicate that the adoption of $\alpha_{\rm CO} \simeq 1.7\ M_\odot$ (Kkms^{-1}pc^2)$^{-1}$ for local (U)LIRGs is reasonable.

5.3. Total line luminosities as a function of galaxy properties

Before investigating molecular line ratios and their dependencies on galaxy properties, it is worth exploring first the trends involving the line luminosities that are used to compute such ratios. We recall that our sample is, by construction, biased toward high $L_{\rm IR}$. This could cause underlying galaxy scaling relations not to be properly captured by our targets, or to be detected with different slopes compared to the global star-forming galaxy population (as already seen, e.g., in Fig. 1), due to the limited range of intrinsic properties (e.g., SFR) probed by local (U)LIRGs (see the discussion on scaling relations in, e.g., Cicone et al. 2017). It is therefore important to identify the portion of the $L'_{\rm line} - L_{\rm IR}$ (or $L'_{\rm line}$- SFR, $L'_{\rm line} - L_{\rm AGN}$) parameter space occupied by our sources in order to place our results into perspective. To this aim, Fig. 5 shows the CO(1–0), CO(2–1), CO(3–2), [CI](1–0) line luminosities as a function of $L_{\rm IR}$, SFR, and $L_{\rm AGN}$, for all targets with corresponding line measurements available (see Table D.1).

For the $L'_{\rm CO}$ versus $L_{\rm IR}$ relations (top-left panel of Fig. 5), we measure correlation coefficients of $\rho_{L'_{\rm CO(1-0)}-L_{\rm IR}} = 0.41$, $\rho_{L'_{\rm CO(2-1)}-L_{\rm IR}} = 0.45$, $\rho_{L'_{\rm CO(3-2)}-L_{\rm IR}} = 0.38$, with p-values $= 7.6 \times 10^{-2}$, 6.4×10^{-3}, 4.1×10^{-2}, respectively). These relations trace, essentially, the Schmidt-Kennicutt (S-K) law (Schmidt 1959; Kennicutt 1998); the correlation coefficients, although hinting of positive relations, do not show significant relation, most likely caused by the narrow range in $L_{\rm IR}$ probed by our sample. Such an hypothesis is strengthened as the ρ coefficients (and their respective p-values) yield much tighter relations between the quantities when the LIRGs in our sample are included in the analysis (see Fig. A.3). Our sample lies close to the $L'_{\rm CO(1-0)} - L_{\rm IR}$ relation obtained by Sargent et al. (2014) for local SBs (see the top-left panel of Fig. 5), which is offset by $\simeq 0.46$ dex from the main-sequence galaxies' relation. We

note that our sample is instead significantly offset with respect to the Herrero-Illana et al. (2019) relation, we ascribe this discrepancy to a combination of two factors: (i) the extrapolation of a relation that is based on a lower-$L_{\rm IR}$ sample than ours; and (ii) their use of a different method for computing the $L_{\rm IR}$ based on an SED fitting, which delivers lower $L_{\rm IR}$ (by ~ 0.5 dex) per given $L'_{\rm CO(1-0)}$. We verified that for the four targets in common with Herrero-Illana et al. (2019), the CO fluxes are consistent, but the $L_{\rm IR}$ computed through their SED fitting (reported in their Table 5) are 0.45–1.0 dex lower than our $L_{\rm IR}$ values, which are instead consistent with the $L_{\rm IR}$ values reported by Armus et al. (2009) for the same sources. The best-fit $L'_{\rm CO(1-0)} - L_{\rm IR}$ relation obtained by running a least square regression analysis on our data is $\log_{10} L'_{\rm CO(1-0)} = (0.8 \pm 2.2) + (0.74 \pm 0.18) \log_{10} L_{\rm IR}$, with $L'_{\rm CO(1-0)}/L_{\rm IR}$ ratios similar to the SB sample of Sargent et al. (2014). This is not surprising since all of the sources in our sample of ULIRGs show enhanced star formation (see Table 1).

The bottom-left panel of Fig. 5 reports $L'_{\rm [CI](1-0)}$ as a function of $L_{\rm IR}$. The [CI](1–0) luminosities span a range $\log_{10} L'_{\rm [CI](1-0)} = 8.7 - 9.8$ [K km s^{-1}pc^2], consistently lower than the CO(1–0) luminosities ($\log_{10} L'_{\rm CO(1-0)} = 9.4 - 10.4$ [K km s^{-1}pc^2]). Figure 1 shows a tight relation between $L'_{\rm CO(1-0)}$ and $L'_{\rm [CI](1-0)}$, and hence a similar relation to that found between $L'_{\rm CO(1-0)}$ (or $L'_{\rm CO(2-1)}$) and $L_{\rm IR}$ is expected. Indeed, we measure a slightly higher Pearson correlation coefficient of $\rho_{L'_{\rm [CI](1-0)}-L_{\rm IR}} = 0.56$ (p-value = 0.04).

The middle panels of Fig. 5 display the CO and [CI] line luminosities as a function of SFR. These relations are not much dissimilar from those with $L_{\rm IR}$ (left panels), as expected since much of the $L_{\rm IR}$ in (U)LIRGs is powered by star formation. Since the SFRs have been computed by removing the contribution to $L_{\rm IR}$ estimated to arise from AGN-heated dust, the middle panels of Fig. 5 should more truthfully trace the S–K relation. However, we struggle to retrieve a tight S–K law for this sample, probably because of selection biases due to their narrow distribution in SFRs, combined with the inevitably large uncertainties on the AGN fraction (Veilleux et al. 2009b). Although we measure slightly higher Pearson correlation coefficients for the $L'_{\rm CO}$ versus SFR relations ($\rho_{L'_{\rm CO(1-0)}-{\rm SFR}} = 0.42$, $\rho_{L'_{\rm CO(2-1)}-{\rm SFR}} = 0.46$, $\rho_{L'_{\rm CO(3-2)}-{\rm SFR}} = 0.50$, with p-values $= 6.8 \times 10^{-2}$, 5×10^{-3} and 5.8×10^{-3}, respectively) than for the $L'_{\rm CO}$ versus $L_{\rm IR}$ relations, the values are still marginal at best for their correlations. When using [CI](1–0) as a H$_2$ tracer, we obtain $\rho_{L'_{\rm [CI](1-0)}-{\rm SFR}} = 0.47$ and p-value $= 8.7 \times 10^{-2}$. The best-fit $L'_{\rm CO(1-0)}$-SFR relation
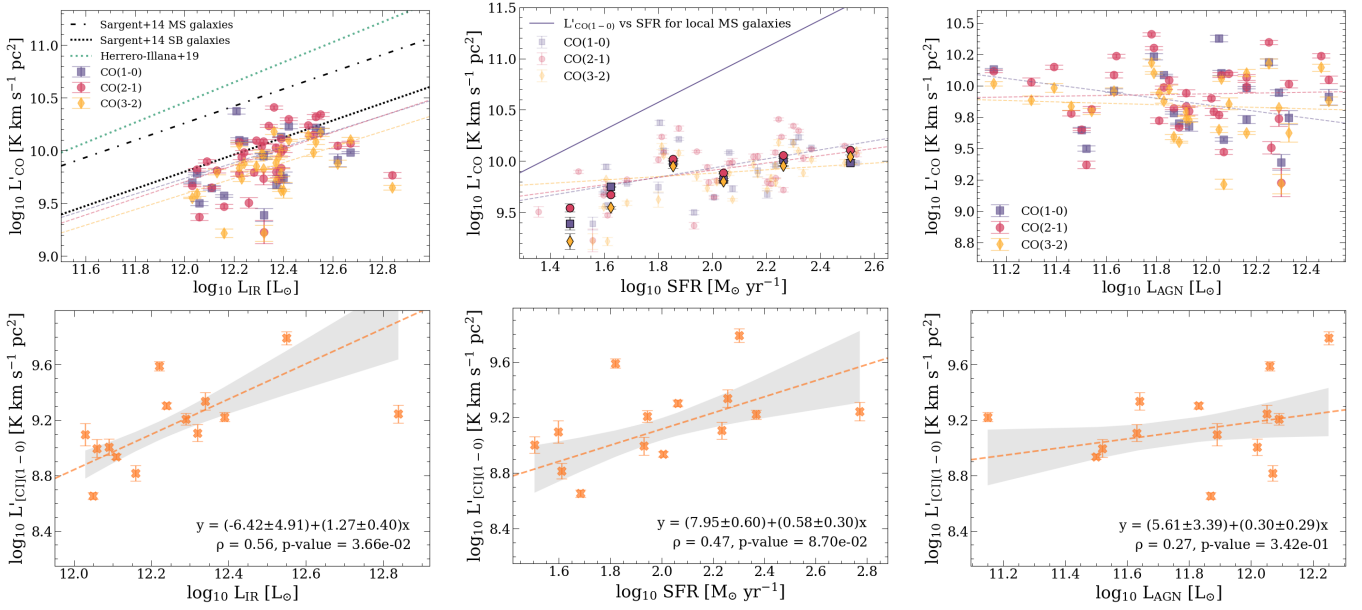
Fig. 5. Global CO(1–0), CO(2–1), CO(3–2) (top panels) and [CI](1–0) (bottom panels) line luminosity plotted as a function of L_{IR} (left), SFR (middle), and L_{AGN}(right) for our sample of ULIRGs. In each plot, the dashed lines are the best-fit relations obtained from a least squares regression analysis conducted for each transition separately (color-coded according to the transition; see the legend in the top-left panel). In the bottom panels, the shaded gray areas correspond to the 1σ confidence interval of the fit. The bottom panels also report the Pearson correlation coefficients (ρ) and their associated p-values. The top-left panel also shows the $L'_{CO(1-0)} - L_{IR}$ relations found by Sargent et al. (2014) for local main-sequence (dot-dashed black line) and SB galaxies (dotted black line), and the $L'_{CO(1-0)} - L_{TIR}$ relation obtained by Herrero-Illana et al. (2019) using IRAM 30m CO(1–0) observations of 55 local sources in the GOALS sample, which comprises mostly LIRGs with $L_{IR} < 10^{12} L_\odot$ and with a <20% AGN contribution to L_{IR}. In the top-middle panel, for better visualization, we over-plot with darker colors the data in bins of SFRs. In this plot, the solid purple line represents the $L'_{CO(1-0)}$-SFR best fit obtained by Cicone et al. (2017) for the ALLSMOG and COLDGASS samples of local star-forming galaxies, described by $\log_{10} L'_{CO(1-0)} = (8.16 \pm 0.04) + (1.34 \pm 0.07) \log_{10}$ SFR.

($\log_{10} L'_{CO(1-0)} = (9.04 \pm 0.22) + (0.44 \pm 0.11) \log_{10}$ SFR) has a flatter slope than the $L'_{CO(1-0)}$-L_{IR} one. Similarly, the $L'_{[CI](1-0)}$-SFR relation (reported on the plot), also shows a considerably shallower slope than the $L'_{[CI](1-0)}$-L_{IR} relation, with a value of 0.6 ± 0.3. In the top-middle panels of Fig. 5, we plot the best-fit $L'_{CO(1-0)}$-SFR relation obtained for a much more unbiased sample of local star-forming main-sequence galaxies (drawn from the COLDGASS and ALLSMOG surveys; see Cicone et al. 2017)[8]. Our ULIRGs are characterized by significantly lower $L'_{CO(1-0)}$/SFR ratios than main-sequence galaxies, especially in the high-SFR regime. The result of lower $L'_{CO(1-0)}$/SFR ratios in (U)LIRGs than in normal main-sequence galaxies is well known, and due to a combination of (i) a higher star formation efficiency (SFE; i.e., higher SFE=SFR/M_{mol}, or equivalently lower $\tau_{dep} = M_{mol}$/SFR) and (ii) a lower α_{CO} compared to normal disk galaxies, as also confirmed by our analysis in Sect. 5.2.

The right panels of Fig. 5 show the CO and [CI] line luminosities as a function of AGN luminosity. Neither of the two gas tracers, in any of the transitions, show any correlation with L_{AGN}. The measured Pearson correlation coefficients and p-values for the CO emission lines are $\rho_{L'_{CO(1-0)}-L_{AGN}} = -0.05$ (p-value = 0.8), $\rho_{L'_{CO(2-1)}-L_{AGN}} = -0.06$ (p-value = 0.7) and $\rho_{L'_{CO(3-2)}-L_{AGN}} = -0.2$ (p-value = 0.3). These results are opposed to what has been found in the literature by, for example, Husemann et al. (2017) and Shangguan et al. (2020a), who find signs of correlation between the CO(1–0) (or CO(2–1)) line luminosity and L_{AGN} on samples of tens of local quasars, although the interpre-

tation is not entirely clear. Indeed, while it is generally accepted that the S-K law traces a fundamental causal relation between the availability of fuel and the resulting star formation activity, the relation between L'_{CO} and L_{AGN} can be only investigated globally, because it relates two processes that affect very different scales in galaxies. We note, however, the change in the relation when the LIRGs in our sample are included (see Fig. A.3), for which we obtain Pearson correlation coefficients and p-values of $\rho_{L'_{CO(1-0)}-L_{AGN}} = 0.53$ (p-value = 0.01), $\rho_{L'_{CO(2-1)}-L_{AGN}} = 0.37$ (p-value = 0.02), and $\rho_{L'_{CO(3-2)}-L_{AGN}} = 0.32$ (p-value = 0.09). Hence, the inclusion of LIRGs, with the consequent widening of the dynamic range in properties probed, produces positive trends between molecular line luminosities and L_{AGN}, in particular, for CO(1–0) and CO(2–1) (although weak); possibly originating from an underlying scaling of both quantities with SFR and/or M_* (see Cicone et al. 2017). It is, however, necessary to confirm these results with a sample including more sources in the $L_{IR} < 12 L_\odot$ regime.

The relation between $L'_{[CI](1-0)}$ and L_{AGN} in our sample of ULIRGs (bottom-right panel of Fig. 5) is equally weak as the relations for CO lines, with a measured correlation coefficient of $\rho_{L'_{[CI](1-0)}-L_{AGN}} = 0.27$ (p-value = 0.3). Interestingly, when we include the LIRGs in the analysis (see Fig. A.3), [CI](1–0) shows a stronger correlation with L_{AGN} than CO(1–0) or CO(2–1), we measure a correlation parameter of $\rho_{L'_{[CI](1-0)}-L_{AGN}} = 0.68$ (p-value = 3.7×10^{-3}), with a slope equal to 0.74 ± 0.26, a similarly tight relation to the one found for $L'_{[CI](1-0)}$ and SFR for the entire sample. Indeed, our sample poorly populates the $L_{IR} < 10^{12} L_\odot$ regime, and these results are solely driven by the galaxy IRAS F12243-0036 (also known as NGC 4418), a source

---

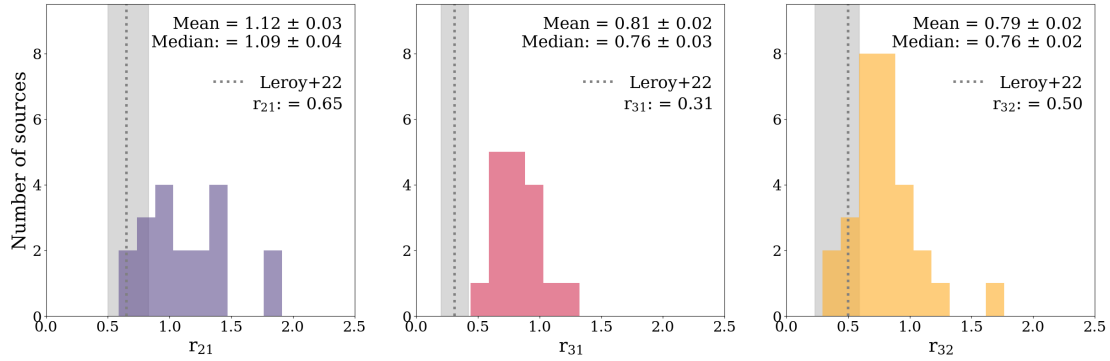[8] SFR range for ALLSMOG and COLDGASS samples: $-1.5 < \log_{10}$SFR $[M_\odot$ yr$^{-1}] < 1.5$.

Fig. 6. Distribution of galaxy-integrated CO line ratios obtained for our sample of ULIRGs, with mean and median values reported at the top right of each plot. Left: $r_{21} \equiv L'_{CO(2-1)}/L'_{CO(1-0)}$. Middle: $r_{31} \equiv L'_{CO(3-2)}/L'_{CO(1-0)}$. Right: $r_{32} \equiv L'_{CO(3-2)}/L'_{CO(2-1)}$. The mean CO line ratios measured by Leroy et al. (2022) in local massive main-sequence disk galaxies are shown using vertical dotted lines, with the gray shaded regions representing their 16-84 velocity percentile ranges.

that is an outlier in many respects. This galaxy has also the lowest redshift ($z = 0.00708$) in our sample, and was discovered by Sakamoto et al. (2010) to host an extremely compact obscured nucleus (CON). Here, $\sim 10^8 M_\odot$ of molecular gas are concentrated in a region with <20 pc size, pointing to extremely high column densities of $N_H > 10^{25}\ cm^{-2}$ (see Falstad et al. 2021, and references therein). If such a correlation between $L'_{[CI](1-0)}$ and L_{AGN} is confirmed with larger statistics, this result could suggest different behaviors of CO and [CI] as H_2 gas tracers in AGN hosts.

5.4. Galaxy-integrated CO line ratios

The distributions of galaxy-integrated CO line ratios ($r_{21} \equiv L'_{CO(2-1)}/L'_{CO(1-0)}$, $r_{31} \equiv L'_{CO(3-2)}/L'_{CO(1-0)}$, $r_{32} \equiv L'_{CO(3-2)}/L'_{CO(2-1)}$) for our local ULIRGs are shown in Fig. 6. Our sample spans a very wide range of values: $0.6 \lesssim r_{21} \lesssim 1.9$, $0.4 \lesssim r_{31} \lesssim 1.3$, and $0.4 \lesssim r_{32} \lesssim 1.7$. For comparison, we report in Fig. 6 also the measurements obtained by Leroy et al. (2022) across tens of local disk galaxies ($N \sim 40, 30, 20$ objects with r_{21}, r_{32}, and r_{31} measurements, respectively), which are based on resolved CO maps and are thus unaffected by beam mismatch. We note that the Leroy et al. (2022) sample is only representative of local massive ($\log_{10} M_*[M_\odot] \sim 10.2 - 10.8$), star-forming galaxies on the main sequence ($-10.5 \lesssim \log_{10} sSFR\ [yr^{-1}] \lesssim -9.9$).

Our mean and median r_{21} values, respectively 1.12 and 1.09, are significantly higher than the average $\langle r_{21} \rangle = 0.79 \pm 0.03$ measured by Saintonge et al. (2017) for the xCOLD GASS sample[9]. Although dominated by massive main-sequence galaxies, the xCOLD GASS sample, being only M_*-selected, includes targets above the main-sequence as well as AGNs; hence, it is not necessarily representative of purely star-forming disks. Indeed, the molecular ISM of main-sequence disks generally presents even lower values of $r_{21} \approx 0.6-0.7$ at $z \sim 0$ (den Brok et al. 2021; Leroy et al. 2022), and perhaps also at higher redshift (see the results at $z \sim 2$ by Aravena et al. 2014). Whether the r_{21} ratio is higher or not in AGNs is not clear, indeed the mean r_{21} measured by Husemann et al. (2017) and Shangguan et al. (2020b) in nearby unobscured quasars are $\langle r_{21} \rangle = 0.9 \pm 0.3$ and $\langle r_{21} \rangle = 0.6^{+0.15}_{-0.13}$, respectively. It is however quite well established

that the central regions of star-forming galaxies, and in general regions with higher Σ_{SFR}, present systematically higher ratios than the outskirts (den Brok et al. 2021; Leroy et al. 2022).

Despite slight variations in different samples, global r_{21} luminosity ratios above unity are extremely rare in the Universe, yet they are predominant in our sample of local (U)LIRGs. This finding is in agreement with Papadopoulos et al. (2012) who, through their analysis of 70 (U)LIRGs with heterogeneous single-dish multi-J CO observations, measured $\langle r_{21} \rangle = 0.91$. This is slightly lower than our mean value, probably because of their larger statistics. It is also probable that the smaller apertures of the *James Clerk Maxwell* Telescope (JCMT) and IRAM 30m telescopes used for the CO(2–1) observations, combined with the narrower bandwidths of the heterodyne receivers used at that time, have contributed to some CO(2–1) flux loss for the most extreme (U)LIRGs of the Papadopoulos et al. (2012) sample. In any case, the r_{21} value distribution obtained by these authors is similarly broad to the one we obtain (Fig. 6) with many sources globally characterized by $r_{21} > 1$ values.

The offset in global CO ratios from the local galaxy population is even more extreme in the r_{31} values, whose mean and median of 0.81 and 0.76 measured in our sample of ULIRGs are significantly higher than $\langle r_{31} \rangle = 0.31$, which is the mean galaxy-integrated value measured by Leroy et al. (2022). Strikingly, Fig. 6 shows that there is no overlap between our ULIRGs sample and normal massive star-forming galaxies in the r_{31} values. The results by Leroy et al. (2022) are consistent with literature data focusing on local massive main-sequence star-forming galaxies, overall confirming that the low-J CO line emission in these sources is dominated by optically thick clouds with moderately sub-thermally excited CO(2–1) and CO(3–2) transitions. As expected due to the diversity of their sample, Lamperti et al. (2020) measure higher values of r_{31} compared to Leroy et al. (2022). Specifically, Lamperti et al. (2020) obtain $\langle r_{31} \rangle = 0.55 \pm 0.05$ for 25 xCOLD GASS objects with JCMT CO(3–2) data, which probe a massive ($M_* > 10^{10}\ M_\odot$), highly star-forming (with $\log_{10} sSFR\ [yr^{-1}] > -10.5$ and with most sources being above the main sequence) portion of the parent xCOLD GASS sample presented by Saintonge et al. (2017). The same study by Lamperti et al. (2020) includes also 36 hard X-ray-selected AGNs from the BASS survey with JCMT CO(3–2) and CO(2–1) observations, and, by extrapolating the CO(1–0) luminosities from the CO(2–1) data, they report consistent r_{31} values compared to a non-AGN sample with matched specific

---

[9] A stellar-mass-selected ($M_* > 10^9\ M_\odot$) and molecular gas fraction-limited sample of 532 local galaxies, having single-dish CO(1–0) and CO(2–1) data from the IRAM 30m and APEX telescopes.
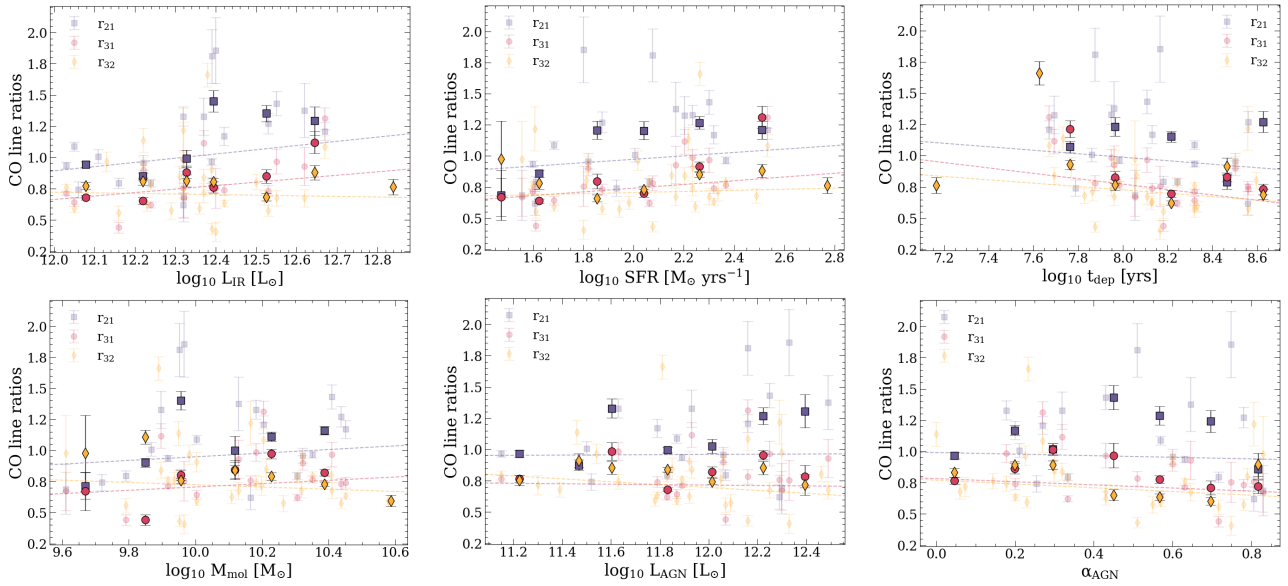
Fig. 7. CO line ratios as a function of galaxy properties: L_{IR} (top left), SFR (top middle), molecular gas depletion timescale due to star formation $\tau_{dep} \equiv M_{mol}/SFR$ (top right), molecular gas mass M_{mol} (computed by using the average α_{CO} derived in this work; bottom right), L_{AGN} (bottom middle), and AGN fraction (L_{AGN}/L_{bol}; bottom right). We show the binned values using darker colors, overplotted on the individual data points. Dashed lines indicate the best-fit relations obtained from a least squares regression analysis conducted for each transition line separately. The color coding refers to different line ratios, as indicated in the legend at the top-right corner of each plot.

SFR. The average LIRG value obtained by Papadopoulos et al. (2012) is $\langle r_{31} \rangle = 0.67^{10}$, with a distribution displaying a significant tail including many sources with $r_{31} \gtrsim 1$.

For completeness, we show in Fig. 6 also our r_{32} measurements, with average and median respectively $r_{32} = 0.80$ and $r_{32} = 0.76$. These are also quite offset from normal galaxy disks, for which Leroy et al. (2022) report $\langle r_{32} \rangle = 0.50$.

5.5. Global CO line ratios as a function of galaxy properties

In Fig. 7 we plotted the total CO line ratios as a function of different galaxy properties, namely: L_{IR} (top left), SFR (top middle), L_{AGN} (top right), M_{mol} (bottom left), molecular gas depletion timescale due to star formation, defined as $\tau_{dep} \equiv M_{mol}/SFR$, which is the inverse of the SFE (SFE $\equiv$ SFR/M_{mol}) (bottom middle), and the AGN fraction ($\alpha_{AGN} \equiv L_{AGN}/L_{bol}$). The values of L_{IR}, SFR, L_{AGN}, and α_{AGN} are taken from the literature and are listed in Table 1 together with their corresponding references. Instead, the M_{mol} and τ_{dep} values have been computed in this work using, for each source, the lowest-J CO transition available and adopting the median α_{CO} factor computed in this work, that is, 1.7 $M_{\odot}$ (Kkms^{-1}pc^2)$^{-1}$ (see Sect. 5.2).

With the aim of better highlighting any underlying trends, we divided the ULIRG sample into bins according to the quantity on the x-axis and calculated the mean values of the ratios in these bins, which are shown using darker symbols in Fig. 7. The dashed lines show the best-fit relations, with color coding indicating different CO line ratios. An inspection of Fig. 7 shows the absence of strong correlations between the global low-J CO line ratios and the other quantities investigated here. This is not completely surprising given the narrow dynamic range in galaxy properties spanned by our sample, which is representative of the most extremely infrared-bright galaxies of the local Universe ($\log_{10} L_{IR}[L_{\odot}] \in [12.0, 12.8]$), making it a very special sample in

its galaxy and ISM properties, already evident in Fig. 6, where almost no overlap with the normal population of star-forming galaxies is seen. However, we retrieve (although still weak) positive correlations between some of the low-J CO line ratios and quantities related to the strength of the star formation activity (namely, L_{IR}, SFR and SFE= τ_{dep}^{-1}).

In the top-left panel of Fig. 7 we investigate the relations between the line ratios and L_{IR}. With measured Pearson correlation coefficients and p-values of $\rho_{r_{21}-L_{IR}} = 0.50$ (p-value = 0.02), $\rho_{r_{31}-L_{IR}} = 0.62$ (p-value = 0.008) and $\rho_{r_{32}-L_{IR}} = -0.02$ (p-value = 0.93), we find that r_{21} and r_{31} show a positive relation with the infrared luminosity, while r_{32} does not. In the relations with SFR (middle top panel), we find the ratio r_{31} to be the only one showing a positive correlation ($\rho_{r_{31}-SFR} = 0.69$ and p-value = 0.002), while no significant correlation is found for r_{21} ($\rho_{r_{21}-SFR} = 0.40$ and p-value = 0.09), and r_{32} ($\rho_{r_{32}-SFR} = 0.10$ and p-value = 0.61). Equivalently to the results seen in Fig. 5, the relations with L_{IR} and SFR are expected to be similar since much of the infrared luminosity in these galaxies is due to star formation. The correlations found with L_{IR} are in agreement with the study performed by Rosenberg et al. (2015) on the HERCULES sample[11], where a correlation was found between high-J CO ratios and L_{FIR} (as well as with dust color). Lamperti et al. (2020) and Leroy et al. (2022) found, for massive main-sequence galaxies with or without an AGN, positive correlations between CO line ratios and SFR, in particular for the ratio r_{31}. If the CO(1–0) emission traces the total H$_2$ reservoir including the more diffuse components, and the CO(3–2) emission traces the somewhat already denser gas, then the ratio r_{31} can be interpreted as a measure of the fraction of molecular gas that is in the denser star-forming regions. This would lead to higher values of r_{31} for ULIRGs and SB galaxies, as these sources are expected to have higher fractions of dense gas, leading also to an increased SFE (and decreased τ_{dep}). Indeed, in our sample of ULIRGs, we compute Pearson coefficient for the CO ratios versus τ_{dep} of $\rho_{r_{21}-\tau_{dep}} = -0.27$ (p-value = 0.27), $\rho_{r_{31}-\tau_{dep}} = -0.58$

---

[10] Papadopoulos et al. (2012) use the r_{32} notation to indicate the $L'_{CO(3-2)}/L'_{CO(1-0)}$ ratio, which we instead indicate as r_{31}.

[11] The *Herschel* Comprehensive ULIRG Emission Survey.

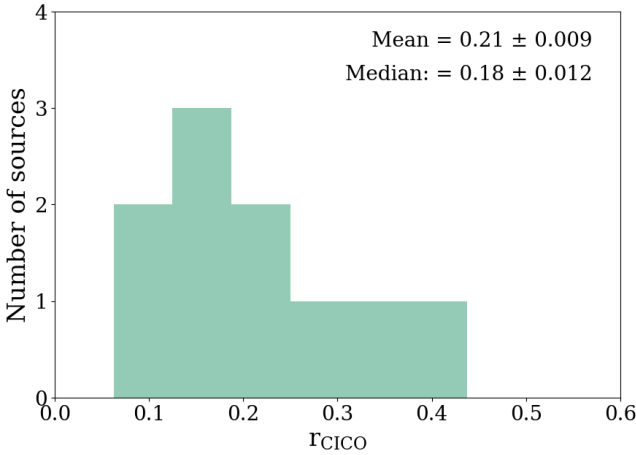**Fig. 8.** Distribution of galaxy-integrated $r_{CICO} \equiv L'_{[CI](1-0)}/L'_{CO(1-0)}$ line ratios obtained for our sample of ULIRGs, with mean and median values reported on the plot.

Fig. 9. r_{CICO} as a function of L_{IR} for our sample of ULIRGs. Similar relations with other galaxy properties are reported in Fig. E.1. Sources with direct measurements of both the [CI](1–0) and CO(1–0) lines are plotted using purple crosses. The pink diamonds represent sources observed in [CI](1–0) but without CO(1–0) line data, for which we inferred $L'_{CO(1-0)}$ from the CO(2–1) line luminosity by assuming $r_{21} = 1.1$, which is the mean value computed for our sample (see Fig. 6). The dashed purple line represents the best fit using a least squares regression analysis, and the shaded gray area corresponds to the 1σ confidence interval of the fit. The Pearson correlation coefficients (ρ) are reported at the upper-left corner of the panel with their associated p-values.

(p-value = 0.02) and $\rho_{r_{32}-\tau_{dep}} = -0.26$ (p-value = 0.17), where only r_{31} shows a (negative) correlation with τ_{dep}, consistent with the (opposite) trend seen by Lamperti et al. (2020) between r_{31} and SFE.

We do not find any trend between these global ratios and molecular gas mass estimates ($\rho = 0.19$, $\rho = 0.25$ and $\rho = -0.24$, for r_{21}, r_{31}, and r_{32}, all having p-values > 0.05). This result is in agreement with Yao et al. (2003), while Leroy et al. (2022) find a weak anticorrelation between r_{21} or r_{31} and the lowest-J CO transition available ($L'_{CO,low}$). We also do not find any significant trend between CO line ratios and L_{AGN} ($\rho = 0.29$, $\rho = 0.10$ and $\rho = -0.10$, for r_{21}, r_{31}, and r_{32}, all having p-values > 0.05), consistent with Lamperti et al. (2020) and Yao et al. (2003). The relations between CO line ratios and the AGN fraction α_{AGN} (lower-right panel of Fig. 7), may suggest a negative trend, in particular for r_{31}, though still not statistically significant as measured by $\rho_{r_{31}-\alpha_{AGN}} = -0.43$ (p-value = 0.09), while r_{21} and r_{32} show no correlation at all with α_{AGN}, having $\rho_{r_{21}-\alpha_{AGN}} = -0.03$ and $\rho_{r_{32}-\alpha_{AGN}} = -0.2$ and p-values > 0.05.

5.6. Global [CI](1−0)/CO(1−0) line ratios

The distribution of integrated [CI](1–0)/CO(1–0) line luminosity ratios ($r_{CICO} \equiv L'_{[CI](1-0)}/L'_{CO(1-0)}$) obtained for our sample is reported in Fig. 8. The measurements span the range $0.08 \lesssim r_{CICO} \lesssim 0.4$, with a median of $\langle r_{CICO} \rangle^{median} = 0.18$ and a mean of $\langle r_{CICO} \rangle^{mean} = 0.21$.

Due to the paucity of [CI](1–0) detections available in the literature, it is unfortunately not possible to compare our results with statistically significant measurements performed on less extreme samples of local star-forming galaxies. Furthermore, often local targets observed in [CI](1–0) do not have adequate, aperture-matched CO(1–0) line data that can be used to compute the [CI](1–0)/CO(1–0) ratio, so there are only a few works to which we can compare our results. Jiao et al. (2019) analyze *Herschel* SPIRE [CI](1–0) maps (with 1 kpc resolution) of 15 nearby galaxies, and combined them with single-dish CO(1–0) observations, convolved to the same beam, obtained with the single-dish Nobeyama 45m telescope. The 15 sources of Jiao et al. (2019) are very famous nearby galaxies: a few SBs (such as M 82, NGC 253, and M 83), one HII galaxy (NGC 891), six low-ionization nuclear emission-line region galaxies
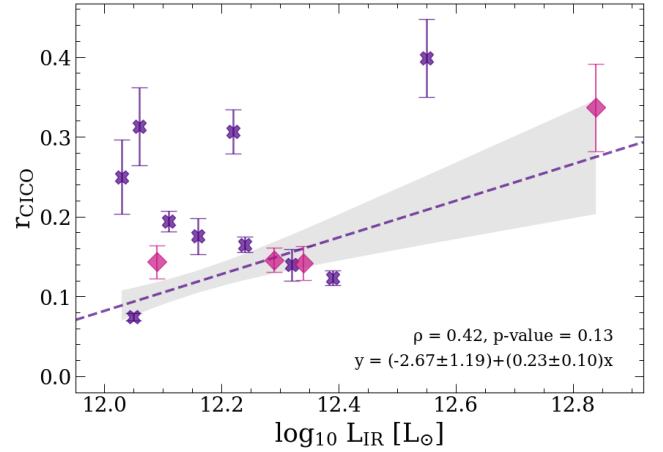
(LINERs) and three Seyferts (including NGC 1068). Their sample is small but it is diverse and covers almost three orders of magnitude in SFR surface density. Therefore, their median r_{CICO} of 0.11 (mean is 0.12), based on multiple measurements per galaxy (one per resolution element), may be considered the closest we can get to a value that is representative of typical local star-forming galaxies. Michiyama et al. (2021) perform simultaneous CO(4–3) and [CI](1–0) observations with ACA Band 8 in 36 local (U)LIRGs, and report single-dish CO(1–0) line luminosity measurements for 25 of their targets that have also an [CI](1–0) line detection. We used these values to compute the average and median r_{CICO} ratio for the Michiyama et al. (2021) sample with both CO(1–0) and [CI](1–0) measurements, both coincidentally being 0.13 with a standard deviation of 0.07. Their median value of 0.13 is lower than what we find for our sample of ULIRGs, despite our samples overlapping by seven sources (of which only five have a CO(1–0) value in Michiyama et al. 2021) and span a similar range of SFRs. We note that only in two cases we decided to employ in our analysis the ACA Band 8 data collected by Michiyama et al. (2021; project ID 2018.1.00994.S; see Table B.1). For the other five overlapping targets we preferred our own APEX PI observations over the ACA archival data, because of their better quality and/or higher flux recovered (see the duplicated [CI](1–0) data shown in Fig. C.1). This is consistent with the considerations by Michiyama et al. (2021), who estimate an [CI](1–0) line flux loss of $\sim 30 - 40\%$ for their ACA data.

We then investigated the r_{CICO} ratio as a function of the following galaxy properties: L_{IR}, SFR, L_{AGN}, M_{mol}, τ_{dep}, and α_{AGN}. According to the Pearson correlation coefficients, none of these relations show a significant trend. Hence, in the main body of the paper, we show only the r_{CICO} versus L_{IR} relation (Fig. 9) and report the other plots in Fig. E.1. As explained earlier, it is hard to make a comparison between our results and previous studies of [CI] and CO in galaxies, because these sparse

previous analyses have mostly considered very heterogeneous samples and data sets, with large aperture and sensitivity variations between different data. With these caveats in mind, we can discuss Fig. 9 in relation to some previous findings. A study performed by Israel et al. (2015) in a sample of 76 local galaxies with *Herschel* [CI] line data and ground-based JCMT ^{13}CO(2–1) line spectra, shows a correlation between the [CI](1–0)/^{13}CO(2–1) flux ratio and L_{FIR}. Though with a Pearson parameter indicating a non-significant correlation, Fig. 9 shows a hint of a positive trend between the [CI](1–0)/^{12}CO(1–0) line ratio and infrared luminosity in our sample of local ULIRGs. There are however two important things to consider. Firstly, the [CI](1–0)/^{13}CO(2–1) ratio investigated by Israel et al. (2015) may behave differently from the [CI](1–0)/^{12}CO(1–0) line ratio that we explore here. Indeed the different isotopologue and rotational level of the CO transition used to compute the ratio implies a different excitation temperature, abundance, and opacity. Secondly, the study by Israel et al. (2015) includes sources spanning $L_{IR} \sim 10^9\ L_\odot$ to $\gtrsim 10^{12}\ L_\odot$, while all the data points studied in Fig. 9 are in the $L_{IR} > 10^{12}\ L_\odot$ regime. Performing a visual inspection of the Israel et al. (2015) [CI](1–0)/^{13}CO(2–1) – L_{FIR} relation, considering only the data points at $L_{FIR} > 10^{12}\ L_\odot$, we observe no clear trend. Taking these considerations into account, our results are actually in agreement with these previous findings: our average r_{CICO} is clearly higher than that computed in less infrared-luminous galaxies by Jiao et al. (2019), as discussed above for Fig. 8. Another study we can examine is Valentino et al. (2018). These authors investigate the [CI](1–0)/CO(2–1) luminosity ratio in a heterogeneous sample including star-forming galaxies on the $z \sim 1.2$ main-sequence observed with ALMA, and ~ 30 local SBs (mostly LIRGs and AGNs) with archival *Herschel* [CI] and ground-based single-dish low-J CO data, respectively from Liu et al. (2015) and Kamenetzky et al. (2016). Their total sample spans $10^{10} \lesssim L_{IR}\ [L_\odot] \lesssim 10^{13.5}$; they find no [CI]/CO ratio variations as a function of L_{IR}, with an average value of $L'_{[CI](1–0)}/L'_{CO(2–1)} \simeq 0.20 \pm 0.02$, consistent with our results.

Similarly, for SFR and L_{AGN}, we retrieve Pearson correlation coefficients of $\rho_{r_{CICO}-SFR} = 0.31$ and $\rho_{r_{CICO}-L_{AGN}} = 0.39$ (with p-values of 0.28 and 0.17, respectively).

6. Discussion

The discussion is divided into three parts. First, in Sect. 6.1, we discuss the possible origin of the high CO line ratios measured in our sample, by exploring also possible dependences on gas kinematics (ISM turbulence, and presence of outflows). Then, in Sect. 6.2 we discuss the origin of the high r_{CICO} ratios, and investigate their relationship with prominent molecular outflows. Finally, in Sect. 6.3 we discuss the role of AGN feedback in setting the molecular gas properties of (U)LIRGs.

6.1. Physical drivers of low-J CO line ratios in (U)LIRGs

6.1.1. A weak dependence on ISM excitation

Our sample is characterized by extremely high global r_{21}, r_{31}, and r_{32} values, which show little or no overlap with those measured in the local main-sequence galaxy population (see Fig. 6). Only marginal correlations were found, mainly for r_{31} with L_{IR}, SFR, and τ_{dep}, while no statistical trends were found with L_{AGN}, or α_{AGN} (see Fig. 7). This suggests that, in these (U)LIRGs, galaxy-averaged low-J CO line ratios are unable to trace effects originated by AGN activity, while ratios depending on CO(3–2)

line emission may start to reflect effects of star formation activity and gas density (seen in the relations with SFR and τ_{dep}). Overall, our results agree with the conclusion of Papadopoulos et al. (2012), who stated that the low-excitation $J_{up} \leq 3$ portion of CO spectral line energy distributions (SLEDs) are "highly degenerate to the average state of the ISM," as we verified here for these (U)LIRGs that are not characterized by cold CO SLEDs.

We highlight the observed large variations of CO line ratios within our sample, much larger than those measured in main-sequence galaxies. Does Fig. 7 inform us about the drivers of such strong differences? The largest $r_{J,J-1}$ variations appear to be typical at the high-L_{IR} end of the sample, in particular for the global r_{21} values, which become consistently $r_{21} > 1$ at $\log_{10} L_{IR}\ [L_\odot] \simeq 12.3$. However, Fig. 7 shows only a weak a link between large CO ratio variations and SFR, but no link to AGNs. This may seem puzzling since AGNs are strong sources of far-UV photons and CRs, which can excite CO, but it is consistent with the hypothesis that low-J CO line ratios in these (U)LIRGs are actually degenerate for CO excitation effects. Higher-J CO transitions are needed to better constrain the effects of AGN on the excitation of the ISM (Gallerani et al. 2014; Rosenberg et al. 2015; Jarvis et al. 2020).

Ratios >1.0 can only be obtained through highly excited gas coupled with low optical depths. More specifically, CO lines can become partially transparent (i.e., reduced line opacities) in the presence of a diffuse, warm, turbulent component characterized by a large velocity gradient. Cicone et al. (2018), based on the analysis of NGC 6240, suggest that such a turbulent (and/or envelope in) H_2 phase may be typical of massive molecular outflows, which are widespread in (U)LIRGs. In Sect. 6.1.2 we explore the hypothesis of a connection between high CO line ratios and the gas kinematics.

6.1.2. Effects of high-velocity and turbulent gas on the CO line ratios

The simultaneous multi-Gaussian component spectral fitting procedure described in Sect. 4.1 (see the spectral fits in Figs. B.1–B.6) allowed us to study CO line ratios as a function of the kinematic properties (v_{cen} and σ_v) of the CO-emitting gas. The results of this investigation are shown in Fig. 10, where we plot the r_{21}, r_{31}, and r_{32} obtained for each Gaussian component employed in the fit as a function of their kinematic parameters, namely: σ_v, $|v_{cen}|$, and the combined parameter $\sigma_v + |v_{cen}|$. We also studied the dependence on v_{cen}, and the results were similar to the ones shown in Fig. 10, which is why we chose to only show the absolute value.

Concerning the gas kinematics, the σ_v values range from ~ 10 km s^{-1} up to ~ 230 km s^{-1}, and v_{cen} from ~ -300 km s^{-1} up to ~ 315 km s^{-1}. Most Gaussian components display $|v_{cen}| \lesssim 100$ km s^{-1}, which are most likely tracing "disk" material with systemic velocities, though we observe components reaching up to $|v_{cen}| \sim 315$ km s^{-1} tracing blueshifted or redshifted velocity gas, with motions clearly deviating from ordered rotation. We caution against an over-interpretation of the specific best-fit kinematic properties for the individual targets, because the possibility to fit multiple components depends mainly on the S/N of the lines and on the presence of spectral substructures. As a result, a source with generally broad CO lines may be fitted either with one single broad component or with multiple narrow components at different velocities. We therefore stress again that the plots presented in Fig. 10 should be regarded for their statistical value.
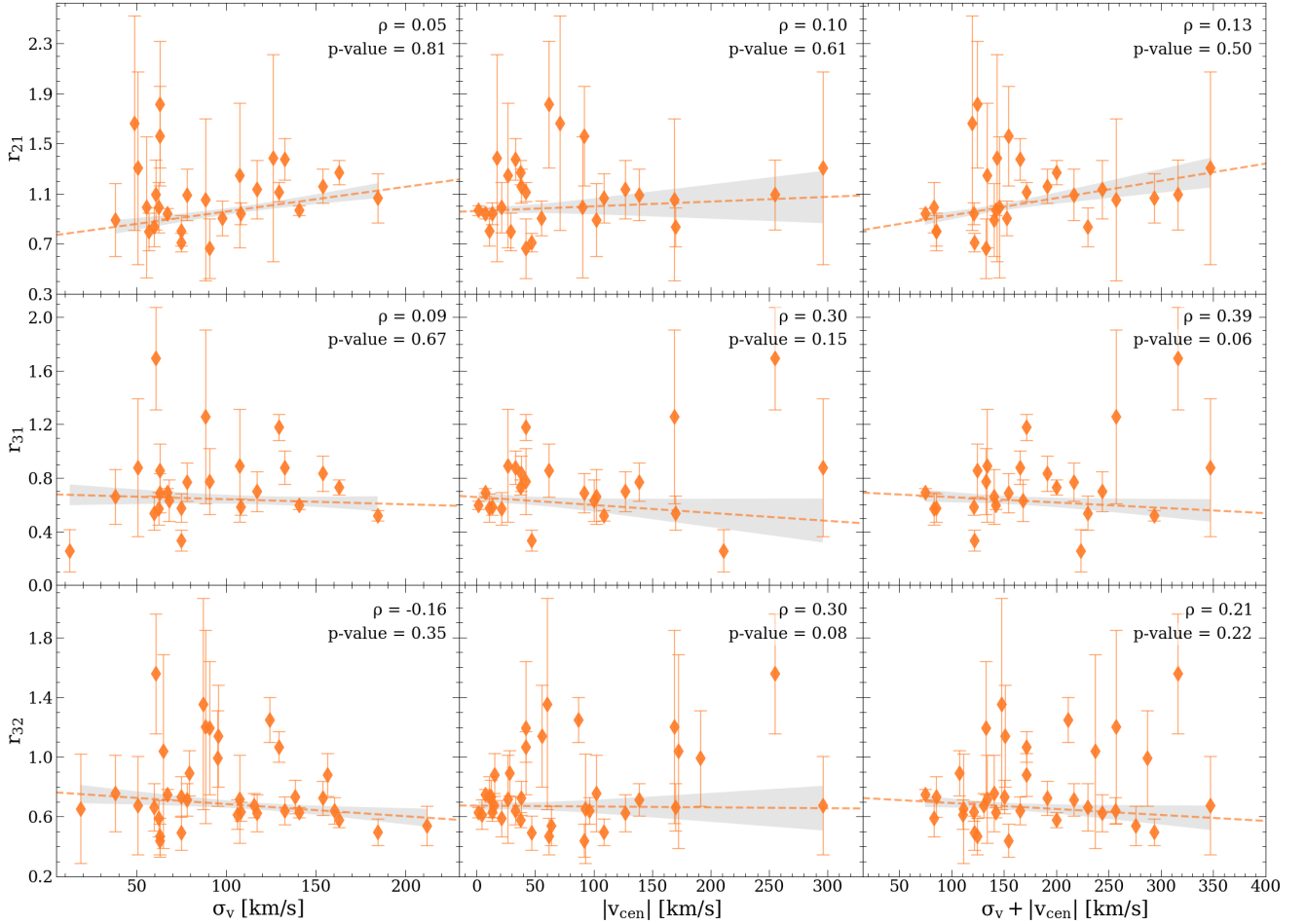
Fig. 10. Individual spectral component analysis of the CO line ratios as a function of the gas kinematics for our sample of ULIRGs. We set a detection threshold of 2σ for the flux of each Gaussian component in order to compute the ratios. The top, central, and bottom rows show, respectively, the r_{21}, r_{31}, and r_{32} plots. Left column: Line ratios as a function of the velocity dispersion, σ_v (line width of the spectral Gaussian component). Middle column: Line ratios as a function of the module of the central velocity of the spectral Gaussian component ($|v_{cen}|$), measured with respect to the galaxy's redshift, reported in Table 1. Right column: Line ratios as a function of the $\sigma_v + |v_{cen}|$ parameter. The dashed lines correspond to the best-fit relations obtained from a least squares regression analysis, and the shaded gray areas correspond to the 1σ confidence interval of the fit. The Pearson correlation coefficients and associated p-values are reported at the top-right corner of each plot, although they are less informative than the best fit because they do not take the (large) error bars into account.

The CO line ratios measured for the individual Gaussian components span similar ranges as the global galaxy-integrated ratios (see Fig. 6), namely: $0.7 \leq r_{21} \leq 1.8$, $0.3 \leq r_{31} \leq 1.8$, and $0.5 \leq r_{32} \leq 1.6$. The Pearson correlation coefficients (ρ) and associated p-values (see Fig. 10) do not evidence any significant trend among the nine relations explored. There are clearly instances where spectral components characterized by higher σ_v and/or higher central velocity show higher CO line ratios, but these trends are not statistically significant if considering the whole sample.

However, we note that the correlation coefficients do not take into account the error bars, which are quite large in this case. We therefore proceed with a regression analysis, whose results are over-plotted in Fig. 10. The r_{21} versus σ_v plot (top-left panel) shows a statistical positive trend, described by the relation

$$r_{21} = (0.76 \pm 0.08) + (2.0 \pm 0.7) \times 10^{-3}\sigma_v. \qquad (11)$$

A similar one is found between r_{21} and $\sigma_v + |v_{cen}|$ ($r_{21} = (0.79 \pm 0.07) + (1.4 \pm 0.5) \times 10^{-3}(\sigma_v + |v_{cen}|)$). Since no clear trend is detected between r_{21} and $|v_{cen}|$, the relation found between r_{21} and $\sigma_v + |v_{cen}|$ is consistent with being entirely driven by the trend with σ_v.

Among the CO ratios explored here, r_{21} is the least sensitive to ISM gas excitation, and so we can hypothesize that the scatter observed in r_{21} values is dominated by optical depth effects (see also Zschaechner et al. 2018). In particular, high $r_{21} \gtrsim 1$ can be explained by a low opacity, especially in the CO(1–0) transition. The positive correlation between r_{21} and σ_v reported in Eq. (11) suggests that the low CO opacity is driven by large velocity gradients, which can in turn be due to turbulence in the ISM and/or bulk motions within molecular outflows. A similar positive trend between r_{21} and σ_v was observed in NGC 6240, and in that case the high-r_{21} and high-σ_v gas was predominantly linked to the massive molecular outflow (Cicone et al. 2018).

We note that neither the r_{31} nor the r_{32} values show significant trends as a function of gas kinematics. It is possible that ratios involving the CO(3–2) line transition are less sensitive to optical depth effects and more affected by gas excitation, and hence the absence of trends with these ratios may support an interpretation of the r_{21} versus σ_v relation in terms of opacity of CO lines, rather than gas excitation effects.

As explained in Sect. 2, our sources were selected from the *Herschel* OH parent sample, and we made use of the literature OH119 μm data to study possible dependences between the
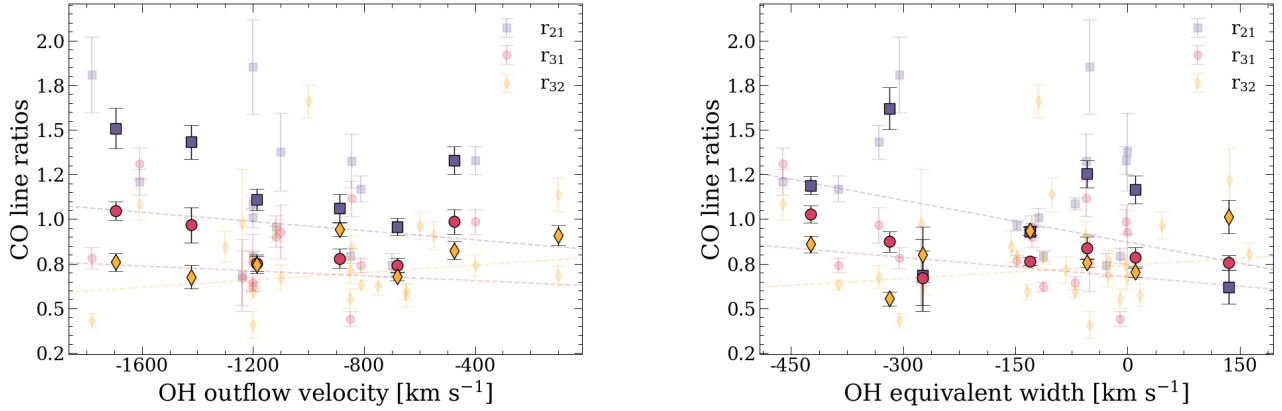
Fig. 11. Global CO line ratios as a function of OH_{max} (left) and OH_{EQW} (right) for the sources with OH119 μm data as reported in the literature (see Table 1). The binned values (computed in the same way as in Sect. 5.4) are shown using darker colors and overplotted on the individual data points. Dashed lines indicate the best-fit relations obtained from a least squares regression analysis conducted for each transition line separately. The color coding refers to different line ratios, as indicated in the legend at the top-right corner of each plot.

line ratios measured in this paper and the available OH outflow parameters, mainly the OH maximal outflow velocity (OH_{max}) for sources that show absorption components and the equivalent width of the OH line (OH_{EQW}). The latter parameter is a negative value for sources where the absorption component is stronger than the emission component of the OH119 μm doublet. The OH parameters are also tracers of molecular gas kinematics in these galaxies and we can test whether there are correlations with the global CO line ratios measured in our sample. In Fig. 11 we show the global r_{21}, r_{31} and r_{32} line ratios as a function of the OH_{max} and OH_{EQW}. As we did also in Sect. 5.5, we divided the total sample into bins according to the quantity on the x-axis and calculated the mean values of the ratios in these bins, which are shown using darker symbols. The dashed lines show the best-fit relations, with color coding indicating different CO line ratios. We do not observe any statistically significant trend between the quantities, with Pearson correlation coefficients of $\rho_{r_{21}-OH_{max}}$ = -0.33 (p-value = 0.23), $\rho_{r_{31}-OH_{max}}$ = -0.13 (p-value = 0.68), $\rho_{r_{32}-OH_{max}}$ = 0.10 (p-value = 0.64), $\rho_{r_{21}-OH_{EQW}}$ = -0.26 (p-value = 0.31), $\rho_{r_{31}-OH_{EQW}}$ = -0.32 (p-value = 0.24), $\rho_{r_{32}-OH_{EQW}}$ = 0.06 (p-value = 0.78). Additionally, the regression analysis performed on each luminosity ratio, which takes the error bars into account, reveal best-fit parameters that are consistent with flat trends for all the variables.

Summarizing, we study any possible trends between the CO line ratios and the kinematics of the gas as traced by (i) the velocity of the individual spectral components of the CO multi-Gaussian fit, and (ii) the OH outflow properties. The former allows us to study the ratios for each spectral component, for which we retrieve a statistically significant positive trend (via regression analysis) between r_{21} and σ_v, likely due to a lower CO opacity in the high-σ_v gas, which could be tracing outflows. On the other hand, we do not find significant trends between the global r_{21} ratios and OH119 μm outflow properties, showing that stronger OH outflows are not statistically associated with globally enhanced r_{21} values. These two results are only in apparent contradiction. Indeed, the OH119 μm outflows are detected in absorption against the FIR continuum and so trace mainly the inner components of the galaxy-scale molecular outflows, while the low-J CO lines, observed in emission and integrated over the whole extent of these galaxies, probe the totality of the molecular gas including extended and diffuse components far from the central engines. Indeed, it would be remarkable if we were to find a trend between the global r_{21} values and the OH outflow proper-

ties. Higher-J CO lines, tracing the medium exposed to the excitation sources, may show tighter relations with the OH outflows. This hypothesis needs to be tested with $J_{up} \geq 4$ CO line observations. In conclusion, our analysis of CO line ratios as a function of gas kinematics, suggests that molecular outflows are not statistically characterized by higher CO line ratios in ULIRGs, at least for low-J CO lines up to $J = 3$. In other words, the low-J CO line ratios do not appear sensitive to the presence or strength of massive molecular outflows.

6.1.3. Absence of a relation between r_{21} and α_{CO}

It has been proposed that, although the CO(2–1)/CO(1–0) luminosity ratio alone cannot be used to constrain the α_{CO} in galaxies (which require either independent H_2 tracers or a much more accurate multi-J analysis of CO lines), variations in r_{21} should be correlated to those observed in α_{CO}, because both these parameters are affected by the optical depth of the gas. This holds as long as other factors, such as the CO abundance, are fixed. In particular, Gong et al. (2020) predict a close-to-linear anticorrelation between r_{21} and α_{CO} ($r_{21} \propto (1/\alpha_{CO})^{1.2}$), based on their models tailored to the ISM conditions typical of galaxy disks. Such a trend is also strengthen by the findings in Leroy et al. (2022): these authors, by fitting radiative transfer models to measured line ratios, find an anticorrelation between r_{21} and α_{CO}. However, such a dependence is not found in our sample. As shown by Fig. 12, r_{21} and α_{CO} values are not correlated ($\rho = 0.16$, p-value = 0.66). The best-fit relation, which takes the large uncertainties on α_{CO} into account, is consistent with a flat trend.

This result further strengthens the hypothesis that the molecular ISM of (U)LIRGs, as traced by low-J CO line ratios, is extremely different from that of normal galaxy disks. The global $r_{21} > 1$ measured in our sample are not even allowed by the models proposed by Gong et al. (2020). Furthermore, even if such high r_{21} values strongly suggest optically thin CO emission, the corresponding α_{CO} estimates of $\sim 1-4$ $M_\odot$ (K km s^{-1} pc^2)$^{-1}$ measured in those same sources that display $r_{21} > 1$ (see Fig. 12), are significantly higher than the optically thin α_{CO} values measured in, for example, disk galaxies (see, e.g., Bolatto et al. 2013). This indicates an apparent contradiction that was already observed in NGC 6240 (Cicone et al. 2018). A possible explanation is the coexistence of a diffuse, turbulent molecular ISM phase, which is characterized by large velocity gradients (such as those typical of outflows) and dominates the
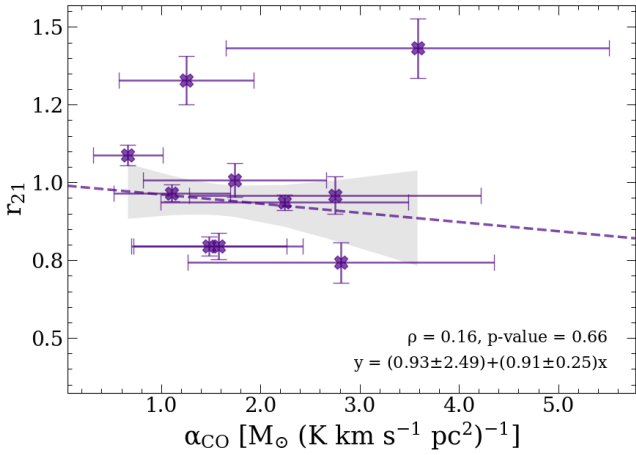
Fig. 12. Global r_{21} ratios plotted as a function of [CI]-derived α_{CO} values. The purple dashed line shows the best-fit relation, with its corresponding 1σ confidence interval represented by the gray shaded area. Neither the Pearson correlation coefficient (ρ) nor the regression analysis suggest any correlation between these quantities.

low-J CO luminosity, with a denser phase, which dominates the gas mass and drives up the [CI]-based α_{CO} measurements. The latter phase may be preferentially traced by denser molecular gas tracers, such as CN, HCN, CS, and higher-J CO transitions.

6.2. Effects of high-velocity and turbulent gas on the [CI]/CO line ratio

In Sect. 5 we show that, in our targets, $L'_{CO(1-0)}$ (as well as $L'_{CO(2-1)}$) is tightly correlated with $L'_{[CI](1-0)}$, and that the [CI](1–0)/CO(1–0) luminosity ratios, spanning $0.07 \lesssim r_{CICO} \lesssim 0.4$, are significantly higher than those measured in normal star-forming galaxies. Such high r_{CICO} values appear to be typical of infrared-bright galaxies, as suggested by previous works (Israel et al. 2015; Valentino et al. 2018). Within our sample, we do not find any significant relation between r_{CICO} and intrinsic galaxy properties such as SFR, M_{mol}, τ_{dep}, or L_{AGN}. In this section we test the hypothesis of a link between r_{CICO} and gas kinematics, and in particular with molecular outflows.

As described in Sect. 4.1, the [CI](1–0) line spectra were fitted independently from the CO lines, due to their generally lower S/N, and to the possibility that CO and [CI] lines may not have identical profiles (see also results in Sect. 5.1.2). Therefore, it is not possible to investigate r_{CICO} ratios as a function of kinematic parameters for individual Gaussian components as we did in Fig. 10 for the CO line ratios. However, we can still investigate the global r_{CICO} values as a function of velocity dispersion of the gas, as traced by, for example, σ_v (from the single Gaussian fit to [CI](1–0) and CO(2–1); see Sect. 5.1.2), the $v_{97.7} - v_{2.3}$ interval for CO and [CI], and as a function of OH properties (i.e., maximal outflow velocity and equivalent width). In Fig. 13, we show the relations between r_{CICO} and $\sigma_{v,CO}$ (top-left panel), $v_{97.7} - v_{2.3}$ for CO (top-right panel), OH outflow maximal velocity (bottom-left panel) and OH equivalent width (bottom-right panel). All Pearson correlation coefficients and the respective p-values are reported in the figures, evidencing no indication of a correlation between any of the quantities. The regression analyses, which take the error bars into account, are consistent with flat trends in all cases. Similarly, we do not find any trend between r_{CICO} and [CI] line widths, as probed by $\sigma_{v,[CI]}$ and its $v_{97.7} - v_{2.3}$ velocity interval. Therefore, our results do not evidence a significant

impact of the gas kinematics on the global [CI]/CO luminosity ratio in (U)LIRGs.

In light of this independence of r_{CICO} from gas kinematics, it remains difficult to explain the detection, shown in Fig. 2, of a marginal deviation of the [CI] and CO line widths from a 1:1 relation, where [CI] lines appear narrower than CO lines in sources with broad CO lines. One hypothesis is that a slight depletion of [CI] with respect to CO in the broad wings of the lines conspires with an enhancement of [CI]/CO in the narrow core of the same lines, so that $\sigma_{v,[CI]} < \sigma_{v,CO}$ while the total luminosity ratio, r_{CICO}, remains unchanged. The reason why [CI] may be fainter in the high-velocity wings of the molecular lines could be due to its optically thin nature. This makes it challenging to detect this line in the presence of more diffuse and extended components of the medium, where the column density is much lower than in the disks. On the contrary, low-J CO lines such as CO(1–0) and CO(2–1) remain bright and relatively easy to detect in such components. The apparent bi-modality of the data observed in the two top panels of Fig. 13, where a cluster of sources with high r_{CICO} and narrower CO lines populate the upper-left regions of the plots, while the remaining data points show low r_{CICO} and high CO line widths, could strengthen that hypothesis. We warn the reader, however, that this needs to be confirmed with larger statistics.

Moreover, the premise of the different behaviors for the two gas tracers studied here is not supported by any theoretical prediction. Actually, such an effect would be at odds with the theoretical prediction that massive molecular outflows contain a significant CO-dark H_2 component, due to leakage of far-UV photons and CRs (Papadopoulos et al. 2004, 2018), which instead seems to be a promising avenue to explain the observational results by Saito et al. (2022) and Ueda et al. (2022). In particular, Saito et al. (2022) use ALMA to explore the [CI](1–0) and CO(1–0) emission within the central 1 kpc of the Seyfert 2 galaxy NGC 1068. They measure the highest r_{CICO} values (median 0.72, 16th–84th range of 0.33–1.86) in a region offset by ~300 pc from the AGN position, beyond the circumnuclear disk, which appears to correspond to the shocked environment between the molecular outflow (see García-Burillo et al. 2014) and the galactic disk. These authors interpret the high [CI]/CO ratios as arising from the shocked gas, due to efficient shock dissociation of H_2 gas by the shock wave, and the consequent dissociation of CO via atomic hydrogen endothermically reacting with said molecule (see Hollenbach & McKee 1980). On the contrary, the SB ring of NGC 1068, which is unaffected by the outflow, displays a much lower median $r_{CICO} = 0.15$ (16th–84th ranges of 0.08–0.23). Given the limited field of view of the [CI](1–0) observation by Saito et al. (2022), an r_{CICO} map beyond the central 1 kpc, which could probe the outflow in regions not overlapping with the galactic disk (therefore not shocked), is not available.

Another example is the study of Arp 220 performed by Ueda et al. (2022), who obtain an r_{CICO} map of the central 5″ (1.9 kpc) of the galaxy. These authors, however, report that the archival ALMA data used in their analysis suffer from missing flux, whose fraction they estimate to be 34% for the [CI](1–0) line through a comparison between their data and JCMT observations (Papadopoulos et al. 2004). Therefore, the results presented by Ueda et al. (2022) apply only for components smaller than the maximum recoverable scale (MRS) of their data sets, 1.75 kpc. Ueda et al. (2022) measure $r_{CICO}^{red\ OF} = 0.9 \pm 0.3$ in the collimated molecular outflow hosted by the western nucleus of Arp 220, clearly higher than the galaxy-integrated value of $r_{CICO} = 0.22 \pm 0.04$. They interpret such a high r_{CICO} value to

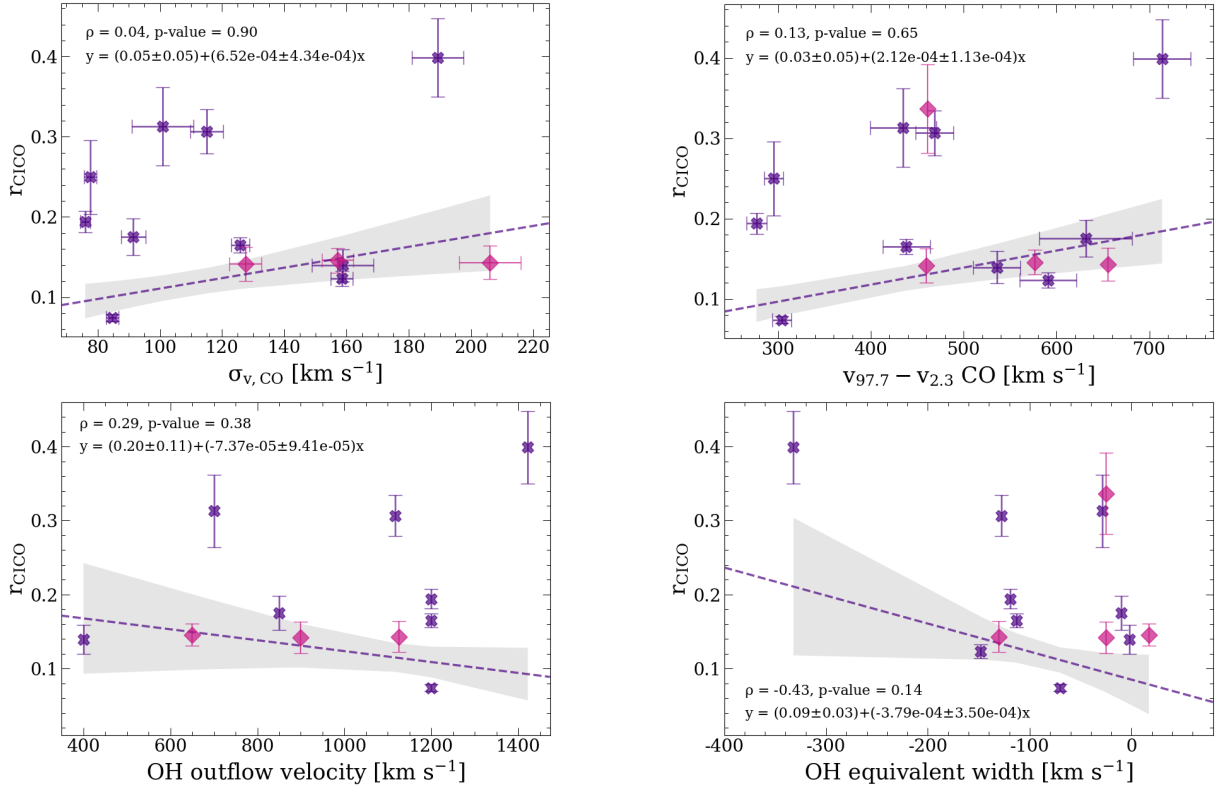**Fig. 13.** Global r_{CICO} as a function of the velocity dispersion of the gas. Top row: [CI](1–0)/CO(1–0) luminosity ratio as a function of $\sigma_{v,CO}$ from the single Gaussian fit (see Sect. 5.1.2, left), and as a function of $v_{97.7} - v_{2.3}$ velocity interval for CO (right). Bottom row: r_{CICO} line ratio as a function of OH_{max} (left) and OH_{EQW} (right). Sources with direct measurements of both the [CI](1–0) and CO(1–0) lines are plotted using purple crosses. For the other sources (pink diamonds), the CO(1–0) line luminosity was estimated assuming the average CO(2–1)/CO(1–0) luminosity ratio of $r_{21} = 1.1$ computed for our sample of ULIRGs. The dashed purple line represents the best fit using a least squares regression analysis, and the shaded gray area corresponds to the 1σ confidence interval of the fit. The Pearson correlation coefficients (ρ) are reported at the upper left corner of the panel with their associated p-values.

be arising from regions with elevated [CI]/CO abundance ratio, which may be caused either by CRs or by shocks. Compared to the results obtained by Saito et al. (2022), the regions with high r_{CICO} in Arp 220 are well within its central region and, as such, could also be driven by shock waves, leading to CO dissociation, as suggested for NGC 1068. However, disentangling between CRs, high radiation fields or shocks, is challenging. Additionally, Ueda et al. (2022) also study how r_{CICO} relates to r_{31} and find a positive trend between $r_{CICO} > 0.3$ measurements and high $r_{31} > 1$ values. Hence, regions with high [CI]/CO luminosity show very high, optically thin CO(3–2)/CO(1–0) ratios. In our sample, although most of the sources with $r_{31} \gtrsim 0.9$ have also $r_{CICO} > 0.2$, the correlation found between the two quantities is not statistically significant ($\rho = 0.52$, p-value = 0.15, best-fit relation: $r_{CICO} = (-0.05 \pm 0.14) + (0.24 \pm 0.20)\ r_{31}$). However, any kiloparsec-scale effects of the type observed by Saito et al. (2022) and Ueda et al. (2022), possibly triggered by collimated outflows and localized shocks, would probably be washed out in the galaxy-integrated measurements used in this work.

6.3. Role of AGN feedback

The CO and [CI]/CO line ratios investigated in this work do not show any significant correlation with L_{AGN} or α_{AGN}, suggesting that AGN radiation has little effect on these ratios, in this sample of (U)LIRGs.

AGN feedback could manifest in different ways in galaxies. One manifestation is through powerful outflows, which expel gas from the central regions and may deplete the galaxy of its M_{mol} reservoir (Cicone et al. 2014). Alternatively, AGN feedback could inject turbulence in the gas (through, e.g., compact jets or outflows), making star formation inefficient even in the presence of cold and dense H_2 gas (see, e.g., Alatalo et al. 2015).

We exploited our refined total molecular gas mass estimates, which are based on higher quality data as well as on an independent check on the α_{CO} factor, to investigate any links between the AGN luminosity and signatures of suppressed star formation in these (U)LIRGs. Figure 14 shows the molecular gas depletion timescale as a function of L_{AGN}. We note that this is the depletion timescale due to the consumption of gas by the star formation activity, without including the gas expelled via outflows (see, e.g., Cicone et al. 2014 for an investigation including AGN feedback).

We find a weak though still statistically significant correlation ($\rho = 0.33$, p-value = 0.05), implying that the ULIRGs with more luminous AGNs consume their gas slower than the ones with less luminous AGNs, or, in other words, have a less efficient star formation. We note, however, that the L_{AGN} values, taken from Veilleux et al. (2013) and Spoon et al. (2013), were computed using method 6 by Veilleux et al. (2009b), which is based on the 15 to 30 μm continuum ratio (f_{30}/f_{15}). This method carries uncertainties on the order of ~20% on average for the reported L_{AGN}. Moreover, we also explored the τ_{dep} versus OH outflow velocity relation, and we did not find any significant trend.
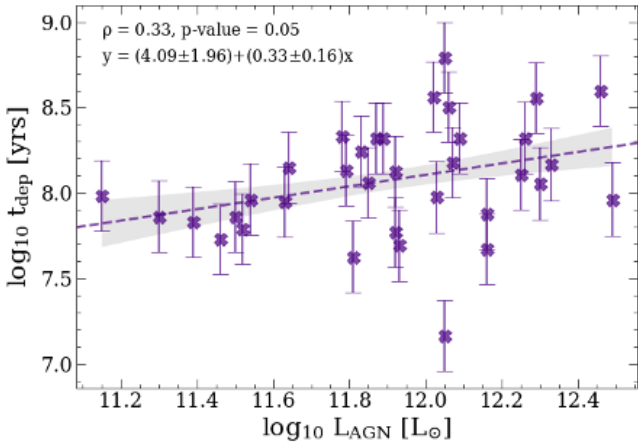
Fig. 14. Depletion timescale ($\tau_{dep} \equiv M_{mol}/SFR$) plotted as a function of L_{AGN}. The dashed line shows the best-fit relation and its 1σ confidence interval plotted as a shaded gray area. The best-fit parameters and the Pearson correlation coefficient are reported at the upper left corner of the panel.

7. Summary and conclusions

We have performed a combined analysis of high S/N CO(1–0), CO(2–1), CO(3–2), and [CI](1–0) emission line spectra of 36 ULIRGs and an additional 4 LIRGs at $z < 0.2$, selected because they had OH 119 μm observations from *Herschel*. These data sets are particularly sensitive to the total line emission from the sources, including faint, low-surface-brightness components that may be missed by high-resolution interferometric observations. All data, both PI and archival, were reduced and analyzed in a uniform way, with the goal of minimizing the aperture biases that usually affect the ratios computed between lines observed at different frequencies. The LIRGs, which are a minority in our sample, were discussed separately from the ULIRGs to avoid the low statistics at $L_{IR} < 10^{12} L_\odot$ biasing our relations. Our findings can be summarized as follows:

- We find a tight relation between CO and [CI] luminosity, $\log_{10} L'_{CO(1-0)} = (4 \pm 2) + (0.64 \pm 0.26) \log_{10} L'_{[CI](1-0)}$, and a very similar one for CO(2–1). This strengthens the hypothesis that atomic carbon is a valid alternative to CO for tracing the bulk of H_2 gas in galaxies.
- We compared the line widths of [CI] and CO, and derived a best-fit relation of $\sigma_{v,[CI]} = (30 \pm 9) + (0.64 \pm 0.07) \sigma_{v,CO}$ when comparing the velocity dispersion obtained via a single Gaussian fit. We also explored the line widths computed at the wings of the lines, using the difference in percentile velocities. We obtain $v_{97.7} - v_{2.3}(CO) = (74 \pm 66) + (0.70 \pm 0.12)v_{97.7} - v_{2.3}([CI])$. Hence, in our sample, [CI] lines are on average narrower than CO lines, especially for sources that show broader line profiles.
- We combined [CI](1–0) and CO(1–0) observations to derive a galaxy-averaged α_{CO} factor. Based on the ten sources with data available for both emission lines, we computed a median value of $\langle \alpha_{CO} \rangle = 1.7 \pm 0.5 \, M_\odot$ (K km s^{-1}pc^2)$^{-1}$. This value is higher than the α_{CO} commonly used in the literature for (U)LIRGs and is consistent with recent estimates by Herrero-Illana et al. (2019) and Kawana et al. (2022) based on the thermal dust continuum.
- In the ULIRGs sample, the total CO and [CI] line luminosities show weak correlations with L_{IR} and the SFR. However, when including the LIRGs, the correlations become much stronger, though they remain weaker for SFRs than for L_{IR}.

Our sample of (U)LIRGs is characterized by L'_{CO}/L_{IR} ratios that are similar to or lower than the SBs' best fit derived by Sargent et al. (2014), and so it is clearly not representative of the general local star-forming population, but rather only its most extreme (merger-driven) SBs.

- We measure extremely high galaxy-integrated CO line ratios, significantly offset from those measured in local massive main-sequence galaxies. For example, more than 50% of our targets have global $r_{21} > 1$ ($\langle r_{21} \rangle^{median} = 1.09$). The distribution of r_{31} values in our (U)LIRGs, with a median of $\langle r_{31} \rangle^{median} = 0.76$, does not even overlap with that of massive local galaxies. The extremely high low-*J* CO ratios of local (U)LIRGs were noted by several previous studies (e.g., Papadopoulos et al. 2012), and here we confirm this trend with better-quality data.
- We investigated possible drivers of such high CO line ratios. The global r_{21} and r_{31} values show a positive relation with L_{IR}, and r_{31} also shows a correlation with the SFR. We studied links between CO line ratios and gas kinematics, as traced by the central velocity and σ_v of the spectral line components simultaneously fit to all three CO transitions. We find a positive trend between r_{21} and the velocity dispersion of the spectral components, probably tracing CO opacity effects, which is described by the relation $r_{21} = (0.76 \pm 0.08) + (2.0 \pm 0.7) \times 10^{-3} \sigma_v$. From these results we infer that, in local (U)LIRGs, low-*J* CO line ratios are generally poor tracers of CO excitation, contrary to what has been found for local massive main-sequence galaxies (e.g., Leroy et al. 2022; Lamperti et al. 2020). We have also explored the CO line ratios as a function of OH outflow properties, as retrieved from the literature (Veilleux et al. 2013; Spoon et al. 2013), and conclude that these ratios are not sensitive to the presence or strength of molecular outflows.
- We measure $r_{CICO} = L'_{[CI](1-0)}/L'_{CO(1-0)}$ values between 0.07 and 0.4, with a median of $\langle r_{CICO} \rangle^{median} = 0.18$. The values we obtained, based on APEX observations, are significantly higher than previous (sparse) measurements in local galaxies, including those obtained from interferometric observations of a partially overlapping sample of ULIRGs. This highlights the importance of sensitive, single-dish observations that can capture the total line flux, especially at high frequencies, where the interferometric flux loss becomes more severe. The r_{CICO} ratios do not show any significant trend with the galaxy properties explored here.
- We do not observe any significant correlation between r_{CICO} and the velocity of molecular outflows (as probed by OH absorption) or gas kinematics (as probed by the CO or [CI] velocity dispersion, σ_v, and the $v_{97.7} - v_{2.3}$ velocity intervals), and hence we rule out gas kinematics or turbulence having, statistically, any significant effect on the global [CI]/CO luminosity ratio. This result makes the discovery that [CI](1–0) lines are narrower than CO lines even more puzzling, because it implies that any effect causing [CI] lines to be narrower (in high-σ_v sources) conspires with some other effect in such a way that the total luminosity ratio remains unchanged.
- Finally, we used our refined total M_{mol} estimates to investigate links between L_{AGN} and signatures of suppressed star formation. We find a statistically significant correlation between $\tau_{dep} \equiv M_{mol}/SFR$ and L_{AGN}, implying that (U)LIRGs with more luminous AGNs are statistically less efficient at forming stars. This could result from injected turbulence by radio jets or AGN winds (see, e.g., Alatalo et al. 2015).

Overall, our analysis confirms the exceptional molecular gas properties of local (U)LIRGs, which are completely different from those of normal star-forming galaxies in the local Universe. This study highlights the necessity of gathering large samples of high S/N observations of alternative H_2 gas tracers in local galaxies, especially [CI] lines, high-J CO lines, and high-density gas tracers (e.g., HCN, CN, CS, and SiO), to understand the extreme mechanisms at work during accelerated phases of galaxy evolution. Due to the faintness of most of these tracers and their potentially different spatial extents in host galaxies, such high S/N multi-tracer analyses need to be conducted with a sensitive large-aperture single-dish telescope with a large instantaneous field of view. Furthermore, observations of [CI] lines and high-J CO lines require a high atmospheric transparency that can only be obtained in a high, dry site. Finally, the large line widths (σ_v) of these local galaxy mergers require stable spectral baselines. The new concept for the Atacama Large Aperture Submillimeter Telescope (AtLAST[12]) satisfies all of these conditions, and so it can be a transformational facility for this field.

References

Aalto, S., Garcia-Burillo, S., Muller, S., et al. 2012, A&A, 537, A44
Aalto, S., Garcia-Burillo, S., Muller, S., et al. 2015, A&A, 574, A85
Abdo, A. A., Ackermann, M., Ajello, M., et al. 2010, A&A, 512, A7
Alatalo, K., Lacy, M., Lanz, L., et al. 2015, ApJ, 798, 31
Aravena, M., Hodge, J. A., Wagg, J., et al. 2014, MNRAS, 442, 558
Armus, L., Mazzarella, J. M., Evans, A. S., et al. 2009, PASP, 121, 559
Arribas, S., Colina, L., Bellocchi, E., Maiolino, R., & Villar-Martín, M. 2014, A&A, 568, A14

Barcos-Muñoz, L., Aalto, S., Thompson, T. A., et al. 2018, ApJ, 853, L28
Belitsky, V., Lapkin, I., Fredrixon, M., et al. 2018, A&A, 612, A23
Biernacki, P., & Teyssier, R. 2018, MNRAS, 475, 5688
Bisbas, T. G., Papadopoulos, P. P., & Viti, S. 2015, ApJ, 803, 37
Bolatto, A. D., Warren, S. R., Leroy, A. K., et al. 2013, Nature, 499, 450
Bothwell, M. S., Aguirre, J. E., Aravena, M., et al. 2017, MNRAS, 466, 2825
Cazzoli, S., Arribas, S., Colina, L., et al. 2014, A&A, 569, A14
Chung, A., Narayanan, G., Yun, M. S., Heyer, M., & Erickson, N. R. 2009, AJ, 138, 858
Cicone, C., Feruglio, C., Maiolino, R., et al. 2012, A&A, 543, A99
Cicone, C., Maiolino, R., Sturm, E., et al. 2014, A&A, 562, A21
Cicone, C., Bothwell, M., Wagg, J., et al. 2017, A&A, 604, A53
Cicone, C., Severgnini, P., Papadopoulos, P. P., et al. 2018, ApJ, 863, 143
Cicone, C., Maiolino, R., Aalto, S., Muller, S., & Feruglio, C. 2020, A&A, 633, A163
Costa, T., Rosdahl, J., Sijacki, D., & Haehnelt, M. G. 2018, MNRAS, 479, 2079
den Brok, J. S., Chatzigiannakis, D., Bigiel, F., et al. 2021, MNRAS, 504, 3221
Downes, D., & Solomon, P. M. 1998, ApJ, 507, 615
Duc, P. A., & Renaud, F. 2013, Lecture Notes Phys., 861, 327
Dunne, L., Maddox, S. J., Vlahakis, C., & Gomez, H. L. 2021, MNRAS, 501, 2573
Falstad, N., Aalto, S., König, S., et al. 2021, A&A, 649, A105
Feruglio, C., Maiolino, R., Piconcelli, E., et al. 2010, A&A, 518, L155
Feruglio, C., Fiore, F., Maiolino, R., et al. 2013, A&A, 549, A51
Feruglio, C., Fiore, F., Carniani, S., et al. 2015, A&A, 583, A99
Fischer, J., Sturm, E., González-Alfonso, E., et al. 2010, A&A, 518, L41
Fluetsch, A., Maiolino, R., Carniani, S., et al. 2019, MNRAS, 483, 4586
Gallerani, S., Ferrara, A., Neri, R., & Maiolino, R. 2014, MNRAS, 445, 2848
García-Burillo, S., Combes, F., Usero, A., et al. 2014, A&A, 567, A125
Genzel, R., Lutz, D., Sturm, E., et al. 1998, ApJ, 498, 579
Glover, S. C. O., Clark, P. C., Micic, M., & Molina, F. 2015, MNRAS, 448, 1607
Gong, M., Ostriker, E. C., Kim, C.-G., & Kim, J.-G. 2020, ApJ, 903, 142
González-Alfonso, E., Fischer, J., Spoon, H. W. W., et al. 2017, ApJ, 836, 11
González-Alfonso, E., Fischer, J., Bruderer, S., et al. 2018, ApJ, 857, 66
Herrera-Camus, R., Janssen, A., Sturm, E., et al. 2020, A&A, 635, A47
Herrero-Illana, R., Privon, G. C., Evans, A. S., et al. 2019, A&A, 628, A71
Hollenbach, D., & McKee, C. F. 1980, ApJ, 241, L47
Hopkins, P. F., Cox, T. J., Kereš, D., & Hernquist, L. 2008, ApJS, 175, 390
Husemann, B., Davis, T. A., Jahnke, K., et al. 2017, MNRAS, 470, 1570
Imanishi, M., & Nakanishi, K. 2014, AJ, 148, 9
Imanishi, M., Nakanishi, K., & Izumi, T. 2019, ApJS, 241, 19
Israel, F. P., Rosenberg, M. J. F., & van der Werf, P. 2015, A&A, 578, A95
Izumi, T., Nguyen, D. D., Imanishi, M., et al. 2020, ApJ, 898, 75
Jarvis, M. E., Harrison, C. M., Mainieri, V., et al. 2020, MNRAS, 498, 1560
Jiao, Q., Zhao, Y., Zhu, M., et al. 2017, ApJ, 840, L18
Jiao, Q., Zhao, Y., Lu, N., et al. 2019, ApJ, 880, 133
Kamenetzky, J., Rangwala, N., Glenn, J., Maloney, P. R., & Conley, A. 2016, ApJ, 829, 93
Kawana, Y., Saito, T., Okumura, S. K., et al. 2022, ApJ, 929, 100
Kennicutt, R. C., Jr 1998, ApJ, 498, 541
Kramer, C., Cubick, M., Röllig, M., et al. 2008, A&A, 477, 547
Lamperti, I., Saintonge, A., Koss, M., et al. 2020, ApJ, 889, 103
Lamperti, I., Pereira-Santaella, M., Perna, M., et al. 2022, A&A, 668, A45
Ledger, B., Wilson, C. D., Michiyama, T., et al. 2021, MNRAS, 504, 5863
Leroy, A. K., Rosolowsky, E., Usero, A., et al. 2022, ApJ, 927, 149
Liu, D., Gao, Y., Isaak, K., et al. 2015, ApJ, 810, L14
Lonsdale, C. J., Farrah, D., & Smith, H. E. 2006 in Astrophysics Update 2, ed. J. W. Mason, 285
Lutz, D., Sturm, E., Janssen, A., et al. 2020, A&A, 633, A134
Martin, C. L. 2005, ApJ, 621, 227
Meledin, D., Lapkin, I., Fredrixon, M., et al. 2022, A&A, 668, A2
Michiyama, T., Saito, T., Tadaki, K.-I., et al. 2021, ApJS, 257, 28
Narayanan, D., Cox, T. J., Robertson, B., et al. 2006, ApJ, 642, L107
Narayanan, D., Cox, T. J., Kelly, B., et al. 2008, ApJS, 176, 331
Offner, S. S. R., Bisbas, T. G., Bell, T. A., & Viti, S. 2014, MNRAS, 440, L81
Ojha, R., Stark, A. A., Hsieh, H. H., et al. 2001, ApJ, 548, 253
Papadopoulos, P. P., Thi, W.-F., & Viti, S. 2004, MNRAS, 351, 147
Papadopoulos, P. P., van der Werf, P. P., Xilouris, E. M., et al. 2012, MNRAS, 426, 2601
Papadopoulos, P. P., Bisbas, T. G., & Zhang, Z. 2018, MNRAS, 478, 1716
Papadopoulos, P., Dunne, L., & Maddox, S. 2022, MNRAS, 510, 725
Pereira-Santaella, M., Colina, L., García-Burillo, S., et al. 2018, A&A, 616, A171
Pérez-Torres, M., Mattila, S., Alonso-Herrero, A., Aalto, S., & Efstathiou, A. 2021, A&A Rev., 29, 2
Planck Collaboration XVI. 2014, A&A, 571, A16
Rosenberg, M. J. F., van der Werf, P. P., Aalto, S., et al. 2015, ApJ, 801, 72

---

[12] https://www.atlast.uio.no

Rupke, D. S., Veilleux, S., & Sanders, D. B. 2005, ApJS, 160, 115
Saintonge, A., Catinella, B., Tacconi, L. J., et al. 2017, ApJS, 233, 22
Saito, T., Michiyama, T., Liu, D., et al. 2020, MNRAS, 497, 3591
Saito, T., Takano, S., Harada, N., et al. 2022, ApJ, 927, L32
Sakamoto, K., Aalto, S., Evans, A. S., Wiedner, M. C., & Wilner, D. J. 2010, ApJ, 725, L228
Salak, D., Nakai, N., Seta, M., & Miyamoto, Y. 2019, ApJ, 887, 143
Sanders, D. B., & Mirabel, I. F. 1996, ARA&A, 34, 749
Sargent, M. T., Daddi, E., Béthermin, M., et al. 2014, ApJ, 793, 19
Schmidt, M. 1959, ApJ, 129, 243
Scoville, N., Sheth, K., Aussel, H., et al. 2016, ApJ, 820, 83
Shangguan, J., Ho, L. C., Bauer, F. E., Wang, R., & Treister, E. 2020a, ApJ, 899, 112
Shangguan, J., Ho, L. C., Bauer, F. E., Wang, R., & Treister, E. 2020b, ApJS, 247, 15
Solomon, P. M., Downes, D., Radford, S. J. E., & Barrett, J. W. 1997, ApJ, 478, 144
Spoon, H. W. W., Farrah, D., Lebouteiller, V., et al. 2013, ApJ, 775, 127
Springel, V., Di Matteo, T., & Hernquist, L. 2005, MNRAS, 361, 776
Stone, M., Veilleux, S., Meléndez, M., et al. 2016, ApJ, 826, 111
Strong, A. W., & Mattox, J. R. 1996, A&A, 308, L21

Sturm, E., González-Alfonso, E., Veilleux, S., et al. 2011, ApJ, 733, L16
Tielens, A. G. G. M., & Hollenbach, D. 1985, ApJ, 291, 722
U, V. 2022, Universe, 8, 392
Ueda, J., Iono, D., Yun, M. S., et al. 2014, ApJS, 214, 1
Ueda, J., Michiyama, T., Iono, D., Miyamoto, Y., & Saito, T. 2022, PASJ, 74, 407
Valentino, F., Magdis, G. E., Daddi, E., et al. 2018, ApJ, 869, 27
Veilleux, S., Rupke, D. S. N., Kim, D. C., et al. 2009a, ApJS, 182, 628
Veilleux, S., Kim, D.-C., Rupke, D. S. N., et al. 2009b, ApJ, 701, 587
Veilleux, S., Meléndez, M., Sturm, E., Gracia-Carpio, J., & Fischer, J. 2013, ApJ, 776, 27
Veilleux, S., Maiolino, R., Bolatto, A. D., & Aalto, S. 2020, A&A Rev., 28, 2
Walter, F., Weiß, A., Downes, D., Decarli, R., & Henkel, C. 2011, ApJ, 730, 18
Weiß, A., Walter, F., & Scoville, N. Z. 2005, A&A, 438, 533
Westmoquette, M. S., Clements, D. L., Bendo, G. J., & Khan, S. A. 2012, MNRAS, 424, 416
Wilson, C. D., Petitpas, G. R., Iono, D., et al. 2008, ApJS, 178, 189
Xia, X. Y., Gao, Y., Hao, C. N., et al. 2012, ApJ, 750, 92
Yao, L., Seaquist, E. R., Kuno, N., & Dunne, L. 2003, ApJ, 588, 771
Zschaechner, L. K., Bolatto, A. D., Walter, F., et al. 2018, ApJ, 867, 111

Appendix A: LIRGs

This appendix shows several plots presented in the main body of the text, now including the 4 LIRGs in our sample. These sources populate poorly the $11.0 < \log_{10} L_{IR} L_\odot < 12.0$ regime, with IRAS F12243-0036 (also known as NGC 4418), with the lowest infrared luminosity and redshift in our sample, being the main driver of the relations found for our extended sample of (U)LIRGs. In Fig. A.1 we plot the [CI](1–0) with respect to CO(1–0) and CO(2–1) line luminosities. The results are similar to the ones obtained in Fig. 1, although the slope is now steeper, with a close-to-linear relation between the quantities.

In Fig. A.2 we explore how the CO-to-H$_2$ conversion factor changes when taking into account the two LIRGs in our sample for which we have both [CI](1–0) and CO(1–0) data (i.e., IRAS F12243-0036 and IRAS F00509+1225). These two sources show average α_{CO} values of ~ 2.5 M$_\odot$ (K km s^{-1} pc^2)$^{-1}$ and ~ 0.7 M$_\odot$ (K km s^{-1} pc^2)$^{-1}$, respectively. The overall mean and median of the α_{CO} factor, remains the same for the extended sample of (U)LIRGs.

Figure A.3 shows the relations between the line luminosities and the general galaxy properties for the extended sample of (U)LIRGs. By including sources with $L_{IR} < 12.0$ L$_\odot$, we now retrieve tighter relations between all CO and [CI] line luminosities and infrared luminosity (top-left and bottom-left panels). On the contrary, the relations with SFR (middle panels) become weaker for all CO lines, and the [CI] line shows now a stronger correlation to SFR. Lastly, the relations with L_{AGN} become stronger for all line luminosities, with statistically significant relations for CO(1–0) ($\rho_{L'_{CO(1-0)}-L_{AGN}} = 0.53$, and p-value = 0.01), CO(2–1) ($\rho_{L'_{CO(2-1)}-L_{AGN}} = 0.37$ and p-value = 0.02), and interestingly, the highest correlation is measured for [CI](1–0) ($\rho_{L'_{[CI](1-0)}-L_{AGN}} = 0.68$ and p-value = 3.7×10^{-3}). If this result were to be confirmed with larger statistics, this could hint of different behaviors for the two gas tracers in the presence of AGNs.
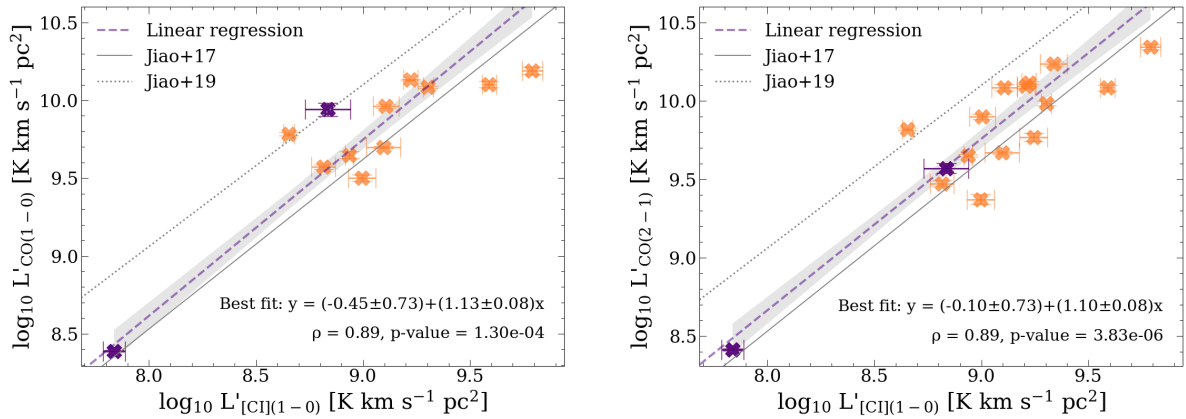
Fig. A.1. Same as Fig. 1, now including the two LIRGs (in purple data points) for which we have [CI](1–0) observations. The best-fit relations (shown as *dashed purple* lines) now include the LIRGs data points. The best-fit parameters are reported at the bottom-right corner of the plots. We also display the Pearson correlation coefficients (ρ) and their associated p-values. The *solid black lines* in both panels represent the corresponding relations reported by Jiao et al. (2017) for a sample of 71 (U)LIRGs, and the *dotted lines* represent the relations of Jiao et al. (2019) for a sample of 15 nearby spiral galaxies, between $L'_{CO(1-0)}$ and $L'_{[CI](1-0)}$.
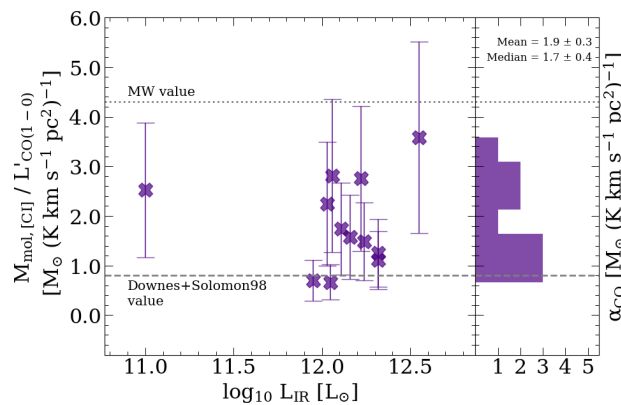
Fig. A.2. Same as Fig. 3, but now including the two LIRGs for which we have [CI](1–0) and CO(1–0) observations. The right part of the plot shows the resulting distribution of [CI]-based α_{CO} values. The *dotted* line indicates the CO-to-H$_2$ conversion factor for the Milky Way galaxy, and the *dashed* line corresponds to the value commonly used in the literature for (U)LIRGs (Downes & Solomon 1998). The mean and median values for the sample of (U)LIRGs remain the same as the ones obtained solely for the ULIRGs: $\alpha_{CO} = 1.9 \pm 0.3$ M$_\odot$ (K km s^{-1} pc^2)$^{-1}$ and 1.7 ± 0.4 M$_\odot$ (K km s^{-1} pc^2)$^{-1}$ for the mean and median, respectively.
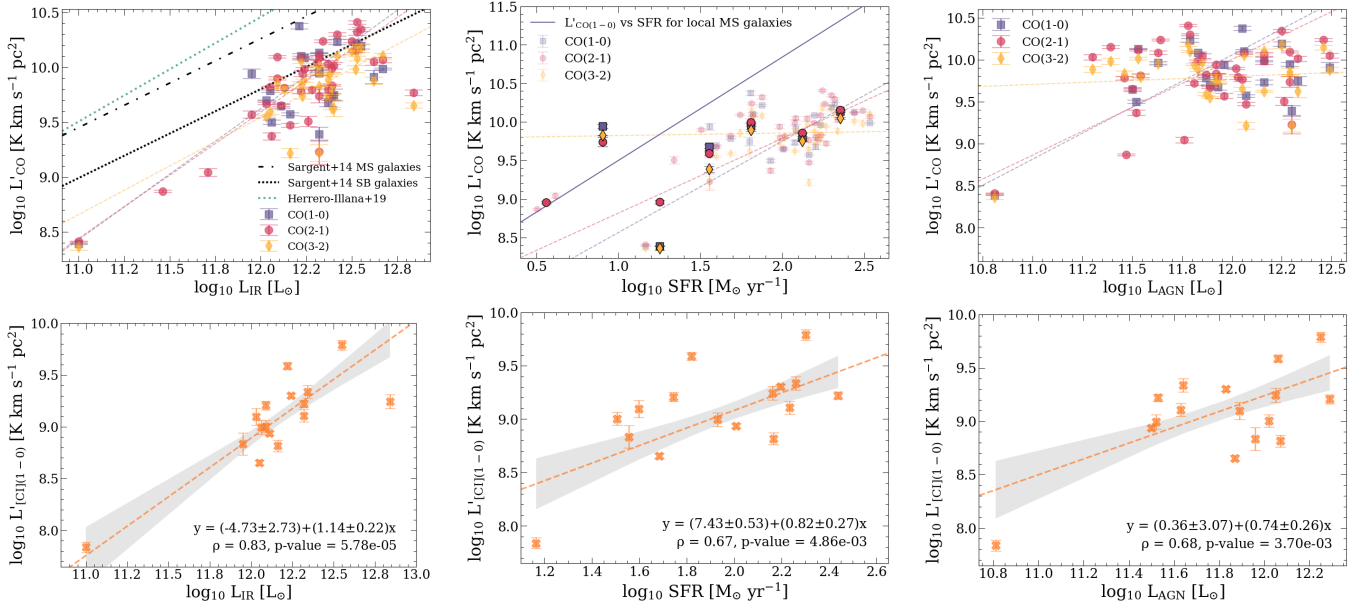
Fig. A.3. Same as Fig. 5, but now including the four LIRGs in the extended sample. In each plot, the dashed lines are the best-fit relations obtained from a least squares regression analysis conducted for each transition separately (color-coded according to the transition; see the legend in the top-left panel). In the bottom panels, the shaded gray areas correspond to the 1σ confidence interval of the fit. The bottom panels report also the Pearson correlation coefficients (ρ) and their associated p-values. The *top-left panel* shows also the $L'_{CO(1-0)}$-L_{IR} relations found by Sargent et al. (2014) for local main-sequence (dot-dashed black line) and SB galaxies (dotted black line), and the $L'_{CO(1-0)}$-L_{TIR} relation obtained by Herrero-Illana et al. (2019) using IRAM 30m CO(1–0) observations of 55 local sources in the GOALS sample including mostly LIRGs with $L_{IR} < 10^{12}\ L_\odot$ and with a < 20% AGN contribution to L_{IR}. In the *top-middle panel*, for better visualization, we over-plotted with darker colors the data in bins of SFRs. In this plot, the solid purple line represents the $L'_{CO(1-0)}$-SFR best fit obtained by Cicone et al. (2017) for the ALLSMOG and COLD GASS samples of local star-forming galaxies, described by $\log_{10} L'_{CO(1-0)} = (8.16 \pm 0.04) + (1.34 \pm 0.07) \log_{10}$ SFR.

Appendix B: The CO and [CI] line data sets: Tables and final reduced spectra

This appendix collects plots and tables describing the CO(1–0), CO(2–1), CO(3–2) and [CI](1–0) spectral line data sets used in this work.

Figures B.1 to B.6 report the final reduced CO(1–0), CO(2–1), CO(3–2), and [CI](1–0) line spectra of our sample of (U)LIRGs. All data, including archival ones, were re-reduced and reanalyzed by us in a consistent and uniform way, following the description provided in Sect. 3. The spectra are presented together with their best-fit multicomponent spectral models, computed following Sect. 4.1.

Table B.1 collects the telescope and project number information for all data used in this work, including the duplicated data not employed in the main analysis (see Appendix C).

Table B.2 lists the values of spectral extraction aperture, the observing time, and the RMS noise values for all the spectral line data sets employed in the analysis.

Table B.1. Data analyzed in this paper

Galaxy	CO(1–0) Telescope	Proj ID	CO(2–1) Telescope	Proj ID	CO(3–2) Telescope	Proj ID	[CI](1–0) Telescope	Proj ID
IRAS 00188−0856	ACA archive	2018.1.00503.S	APEX archive	099.F−9709	ACA archive	2018.1.00503.S		
IRAS 01003−2238	ALMA archive	2013.1.00535.S	APEX archive	099.F−9709	APEX PI / APEX archive	0106.B−0674 / 090.B−0404		
IRAS F01572+0009	ALMA archive	2013.1.00535.S	APEX PI	0104.B−0672	APEX PI / ALMA archive	0106.B−0674 / 2012.1.00611.S		
IRAS 03521+0028			APEX PI	0104.B−0672	APEX PI	0106.B−0674		
IRAS F05024−1941			APEX PI	0104.B−0672	APEX PI	0106.B−0674		
IRAS F05189−2524	ALMA archive	2013.1.00535.S	APEX PI	0104.B−0672	ACA archive	2012.1.00611.S	APEX PI	0104.B−0672
IRAS 06035−7102	ACA archive	2018.1.00503.S	APEX PI	0104.B−0672	APEX PI	0106.B−0674	APEX PI	0104.B−0672
IRAS 06206−6315			APEX PI	0104.B−0672	APEX PI / APEX archive	0106.B−0674 / 090.B−0404		
IRAS 07251−0248			ALMA archive / APEX archive	2018.1.00699.S / 086.F−9321	APEX archive	086.F−9321		
IRAS 08311−2459			APEX PI	0104.B−0672	APEX archive	090.B−0404		
IRAS 09022−3615			APEX PI	0104.B−0672	APEX PI	0106.B−0674	APEX PI / ACA archive	0104.B−0672 / 2018.1.00994.S
IRAS 10378+1109			APEX PI	0104.B−0672	APEX archive	090.B−0404		
IRAS 11095−0238			APEX PI	0104.B−0672	APEX archive	090.B−0404		
IRAS F12072−0444	ALMA archive	2013.1.00535.S	APEX PI	0104.B−0672	APEX archive	090.B−0404		
IRAS F12112+0305	ALMA archive	2016.1.00140.S	APEX PI	0104.B−0672	APEX PI / ACA archive	0106.B−0674 / 2016.2.00042.S	APEX PI / ACA archive	0104.B−0672 / 2018.1.00994.S
IRAS 13120−5453	ALMA archive	2015.1.00287.S	APEX archive / APEX archive	090.B−040 / 092.F−9325	APEX archive / APEX archive	090.B−040 / 092.F−9325	APEX PI	0104.B−0672
IRAS F13305−1739			APEX PI	0104.B−0672				
IRAS 13451+1232	ALMA archive	2013.1.00180.S	APEX PI	0104.B−0672	APEX PI / ALMA archive	0106.B−0674 / 2013.1.00180.S		
IRAS F14348−1447			APEX PI / APEX archive	0104.B−0672 / 090.B−0404			APEX PI / ACA archive	0104.B−0672 / 2018.1.00994.S
IRAS F14378−3651	ACA archive	2018.1.00503.S	ACA archive	2018.1.00503.S			APEX PI	0104.B−0672

Table B.1. Continued.

Galaxy	CO(1–0) Telescope	CO(1–0) Proj ID	CO(2–1) Telescope	CO(2–1) Proj ID	CO(3–2) Telescope	CO(3–2) Proj ID	[CI](1–0) Telescope	[CI](1–0) Proj ID
IRAS F15462−0450	ALMA archive	2015.1.01147.S	APEX archive	099.F−9709	APEX PI ACA archive	0106.B−0674 2018.1.00503.S		
IRAS 16090-0139	ACA archive	2018.1.00503.S	APEX PI	0104.B−0672	APEX PI ALMA archive	0106.B−0674 2015.1.00102.S	APEX PI	0104.B−0672
IRAS 17208−0014	ALMA archive	2016.1.00177.S	APEX PI	0104.B−0672			APEX PI	0104.B−0672
IRAS 19254−7245			APEX archive	090.B−0404	ACA archive	2018.1.00503.S	APEX PI	0104.B−0672
IRAS F19297−0406			APEX PI	0104.B−0672				
IRAS 19542+1110	ALMA archive	2017.1.01235.S	APEX PI	0104.B−0672	ACA archive APEX archive ALMA archive	2018.1.00503.S 090.B−0404 2018.1.00888.S	APEX PI	0104.B−0672
IRAS 20087−0308	ACA archive	2018.1.00503.S	APEX PI	0104.B−0672				
IRAS 20100-4156	ALMA archive	2013.1.00659.S	APEX PI	0104.B−0672	APEX PI APEX archive	0106.B−0674 090.B−0404		
IRAS 20414-1651			APEX PI ALMA archive	0104.B−0672 2018.1.00699.S	APEX PI APEX archive	0106.B−0674 084.F−9306		
IRAS F20551−4250	ACA archive	2016.2.00006.S	APEX PI	0104.B−0672	APEX PI	0106.B−0674	ACA archive	2018.1.00994.S
IRAS F22491-1808	IRAM PdBI	UF2A	APEX PI	0104.B−0672	APEX PI APEX archive	0106.B−0674 084.F−9306	APEX PI ACA archive	0104.B−0672 2018.1.00994.S
IRAS F23060+0505			APEX PI	0104.B−0672	ACA archive	2016.2.00042.S		
IRAS F23128-5919	ALMA archive	2017.1.01398.S	APEX PI	0104.B−0672	ACA archive APEX archive	2018.1.00503.S 090.B−0404	APEX PI ACA archive	0104.B−0672 2018.1.00994.S
IRAS 23230-6926	ACA archive	2018.1.00503.S	APEX PI	0104.B−0672	APEX archive APEX PI	090.B−0404 0106.B−0674		
IRAS 23253-5415			APEX PI	0104.B−0672				
IRAS F23389+0300			APEX PI	0104.B−0672				
IRAS F00509+1225	ALMA archive	2015.1.01147.S	APEX PI	0104.B−0672			APEX PI	0104.B−0672
PG1126−041			ACA archive APEX PI	2017.1.00297.S 0104.B−0672				
IRAS F12243−0036	ALMA archive	2016.1.00177.S	ACA archive	2012.1.00377.S	APEX archive	077.F−9300	APEX PI ACA archive	0104.B−0672 2018.1.00994.S
PG2130+099			ACA archive APEX PI	2017.1.00297.S 0104.B−0672			APEX PI	0104.B−0672

Notes. The data collected for the analysis performed throughout this paper is a combination of PI and archival data from several telescopes: APEX, ALMA, ACA and PdBI. We report all the data sets used with their respective project IDs. For the cases (line + source) where there is more than one data set available, we report the data set used on top, followed by the rest. The [CI](1–0) line observation for the source PG2130+099 is a non-detection, though we still report it, and in Table D.1, we report the upper limit.

Table B.2. Description of the observations

Galaxy name	CO(1-0) $d_{aperture}$ ["]	CO(1-0) t_{obs} [h]	CO(1-0) rms [mJy]	CO(2-1) $d_{aperture}$ ["]	CO(2-1) t_{obs} [h]	CO(2-1) rms [mJy]	CO(3-2) $d_{aperture}$ ["]	CO(3-2) t_{obs} [h]	CO(3-2) rms [mJy]	[CI](1-0) $d_{aperture}$ ["]	[CI](1-0) t_{obs} [h]	[CI](1-0) rms [mJy]
(1)	(2)	(3)	(4)	(5)	(6)	(7)	(8)	(9)	(10)	(11)	(12)	(13)
IRAS 00188−0856	30	0.65	3	28	1.4	32	15	0.34	5			
IRAS 01003−2238	5	0.03	5	28	3.3	35	20	0.84	45			
							20	0.49	93			
IRAS F01572+0009[†]	7	0.03	10	34	1.3	12	20	1.6	30			
							8	0.54	5			
IRAS 03521+0028				34	2.0	10	20	0.95	28			
IRAS F05024−1941				34	2.3	10	20	1.24	22			
IRAS F05189−2524	30	1.5	4	27	0.21	25	20	0.75	120	13	0.82	148
							12	1.86	13			
IRAS 06035−7102	41	0.24	11	27	0.19	32	20	3.3	486	13	0.6	158
							20	0.44	59			
IRAS 06206−6315				27	0.6	26	20	0.8	45			
IRAS 07251−0248				5	0.69	3.3						
				28	1.22	24						
							20	1.11	110			
IRAS 08311−2459				27	0.43	41	20	0.74	98	13	0.17	139
										8	0.08	46
IRAS 09022−3615				27	0.46	39	20	0.63	152			
IRAS 10378+1109				27	1.66	22	20	1.43	42			
IRAS 11095−0238				27	0.76	26	20	0.37	144			
IRAS F12072−0444[†]	5	0.03	7	27	0.33	29	20	0.86	65	13	0.23	148
IRAS F12112+0305	10	0.09	5	27	0.4	37	20	1.47	113	10	0.08	36
							15	2.72	42			
IRAS 13120−5453	17	0.22	12	28	0.35	81	20	0.5	130	13	0.17	185
				30			20					
IRAS F13305−1739				34	0.71	12						
IRAS F13451+1232	12	0.4	4	27	0.24	26	20	1.26	37			
							6	0.08	6			

Table B.2. Continued.

Galaxy name	CO(1–0)			CO(2–1)			CO(3–2)			[CI](1–0)		
(1)	$d_{aperture}$ ["] (2)	t_{obs} [h] (3)	rms [mJy] (4)	$d_{aperture}$ ["] (5)	t_{obs} [h] (6)	rms [mJy] (7)	$d_{aperture}$ ["] (8)	t_{obs} [h] (9)	rms [mJy] (10)	$d_{aperture}$ ["] (11)	t_{obs} [h] (12)	rms [mJy] (13)
IRAS F14348–1447				27	0.21	32				13	0.24	292
				28	0.21	107				9	0.08	15
				20	0.08	9				13	0.08	191
IRAS F14378–3651	30	0.15	8									
IRAS F15462–0450	17	0.3	17	28	1.9	20						
IRAS 16090–0139	30	0.15	6	27	0.68	21	20	0.53	77	13	1.8	131
							15	0.17	13			
IRAS 17208–0014	16	0.53	1.35	27	0.11	39	20	0.34	239	13	0.18	232
							11	0.27	81.5			
IRAS 19254–7245				28	1.2	27				13	0.41	79
IRAS F19297–0406				27	0.42	19	30	0.17	19			
IRAS 19542+1110	9	0.35	5	27	0.64	34				13	0.08	138
IRAS 20087–0308	30	0.08	9	27	0.59	22	20	0.17	14			
IRAS 20100–4156	25	3.5	1	27	1.09	17	20	1.58	59			
							7	0.94	6			
IRAS 20414–1651				27	0.98	19	20	1.24	70			
				4	0.78	122	20	0.76	90			
IRAS F20551–4250	35	0.4	11	27	0.4	42	20	0.42	150	9	0.08	44
							20	0.2	132			
IRAS F22491–1808				27	0.32	30	20	2	69			
IRAS F23060+0505	10	3	1	34	1.32	16	20	2.7	28	13	0.53	135
				15			15	2.7	20	9	0.08	29
IRAS F23128–5919	23	2.27	2	27	0.68	26	20	0.35	102	13	0.16	414
										11	0.08	43
IRAS 23230–6926	30	1.29	4	27	0.73	21	20	0.58	8			
							15	0.6	116			
IRAS 23253–5415				27	0.83	21	20	1.28	75			
IRAS F23389+0300				34	2.4	11	20	1.8	25			
IRAS F00509+1225	23	0.07	26	27	0.29	42				13	0.72	650
				32	2.5	2						
				27	0.59	25						
PG1126–041												
IRAS F12243–0036	12	0.5	4	29	1.3	18	20	0.06	562	13	0.11	327
										9	0.45	23
PG2130+099				30	2.06	3				13	1.8	70
				27	2	17						

Notes. For each transition, we report single-dish beam or spectral extraction aperture ($d_{aperture}$), the observing time (t_{obs}) (corresponding to the effective value after excluding the discarded sub-scans), and the spectral rms computed using $\Delta v = 50$ km s^{-1} velocity channels. † Sources for which uv-tapering was applied for the ALMA CO(1–0) archival data.
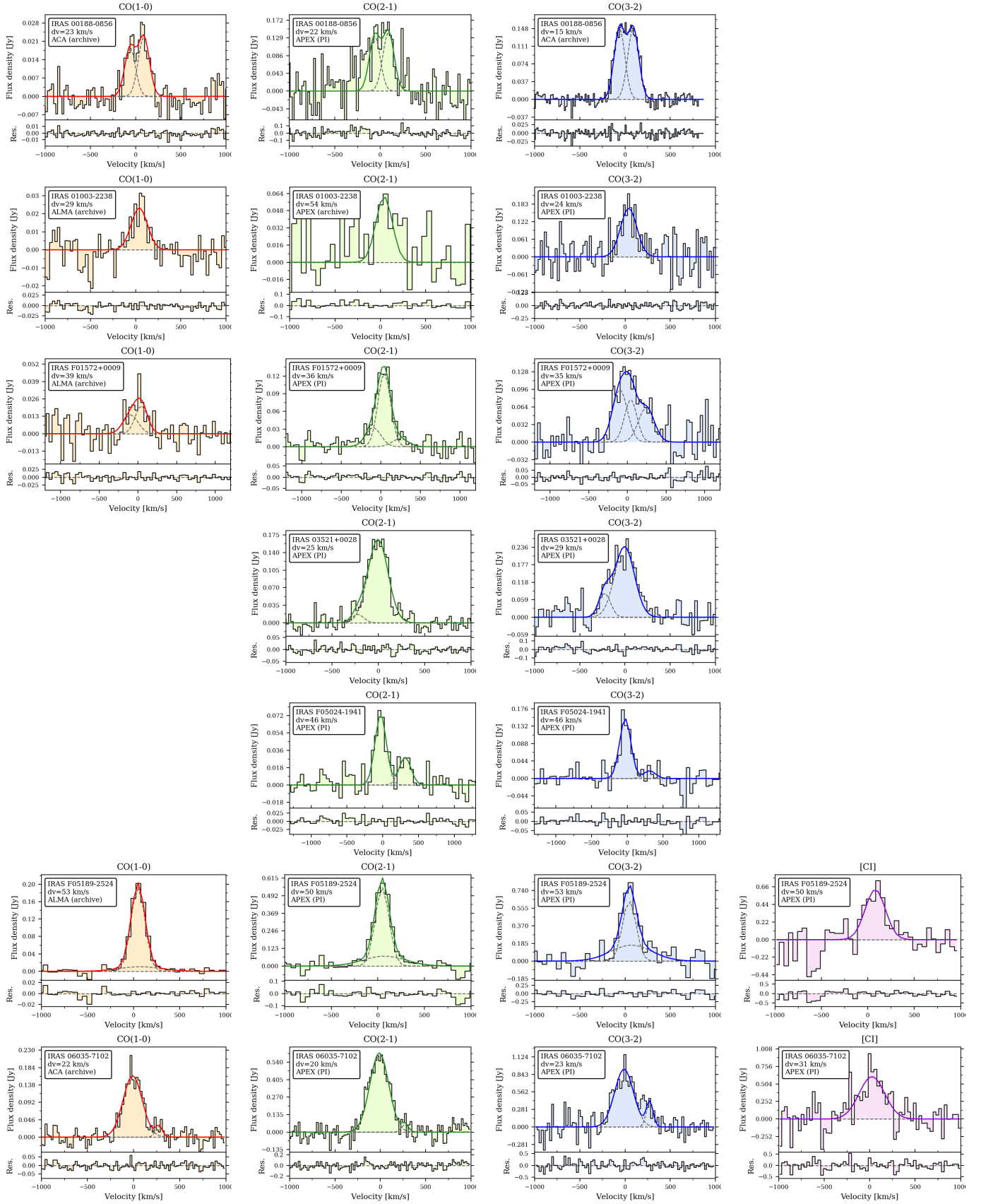
Fig. B.1. Integrated, continuum-subtracted CO(1–0), CO(2–1), CO(3–2) and [CI](1–0) spectra, including only the data employed in the analysis. We show in red the CO(1–0) transition, in green the CO(2–1) transition, in blue the CO(3–2) transition, and in magenta the [CI](1–0) transition. The source name, spectral binning, and telescope are reported on the top-left corner of each plot. This figure shows sources: IRAS 00188-0856, IRAS 01003-2238, IRAS F01572+0009, IRAS 03521+0028, IRAS F05024-1941, IRAS F05189-2524, and IRAS 06035-7102.
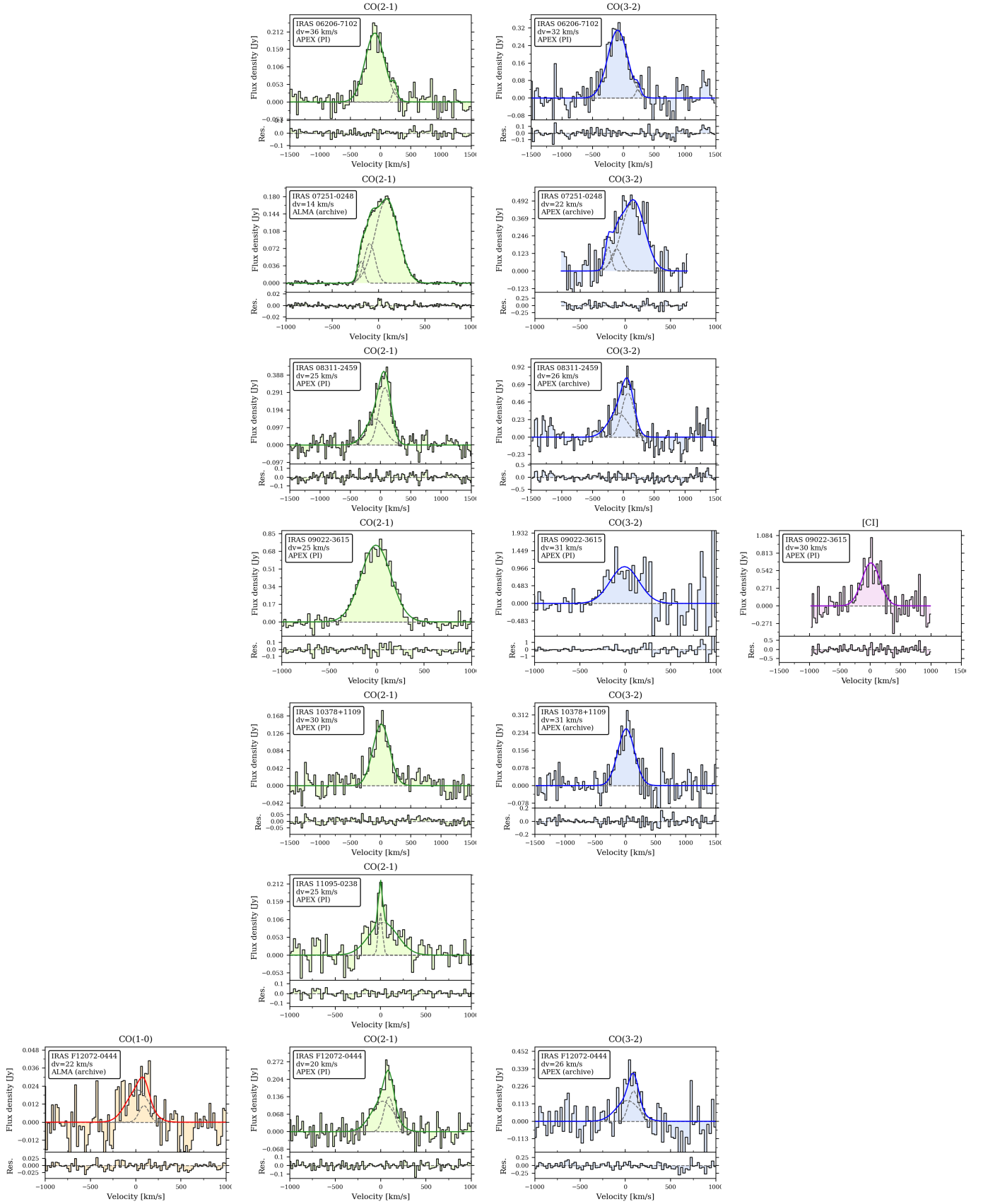
Fig. B.2. Continued from Fig. B.1. This figure shows sources: IRAS 06206-6315, IRAS 07251-0248, IRAS 08311-2459, IRAS 09022-3615, IRAS 10378+1109, IRAS 11095-0238, and IRAS F12074-0444.
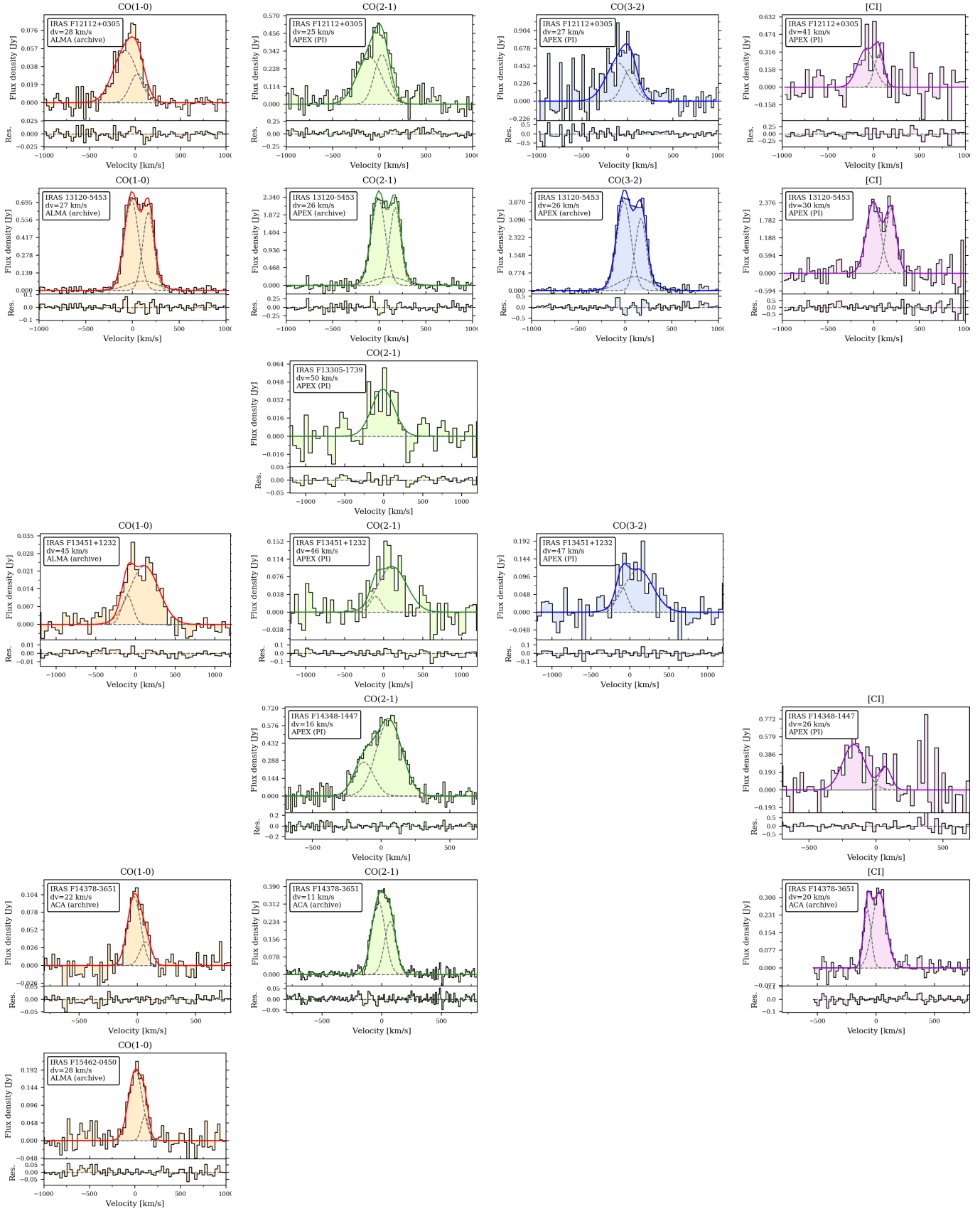
Fig. B.3. Continued from Fig. B.2. This figure shows sources: IRAS F12112+0305, IRAS 13120-5453, IRAS F13305-1739, IRAS F13451+1232, IRAS F14348-1447, IRAS F14378-3651, and IRAS F15462-0450.
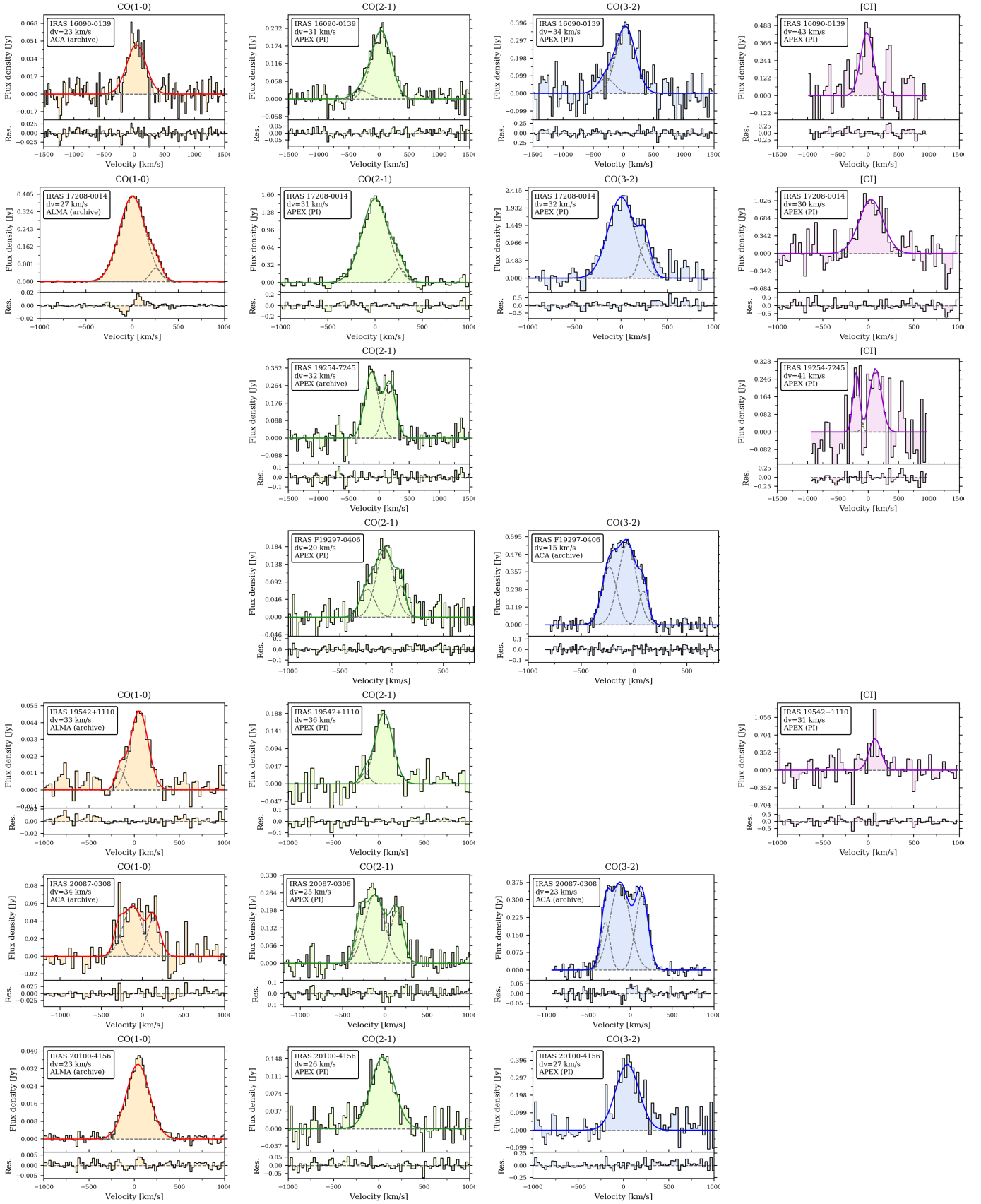
Fig. B.4. Continued from Fig. B.3. This figure shows sources: IRAS 16090-0139, IRAS 17208-0014, IRAS 19254-7245, IRAS F19297-0406, IRAS 19542+1110, IRAS 20087-0308, and IRAS 20100-4156.
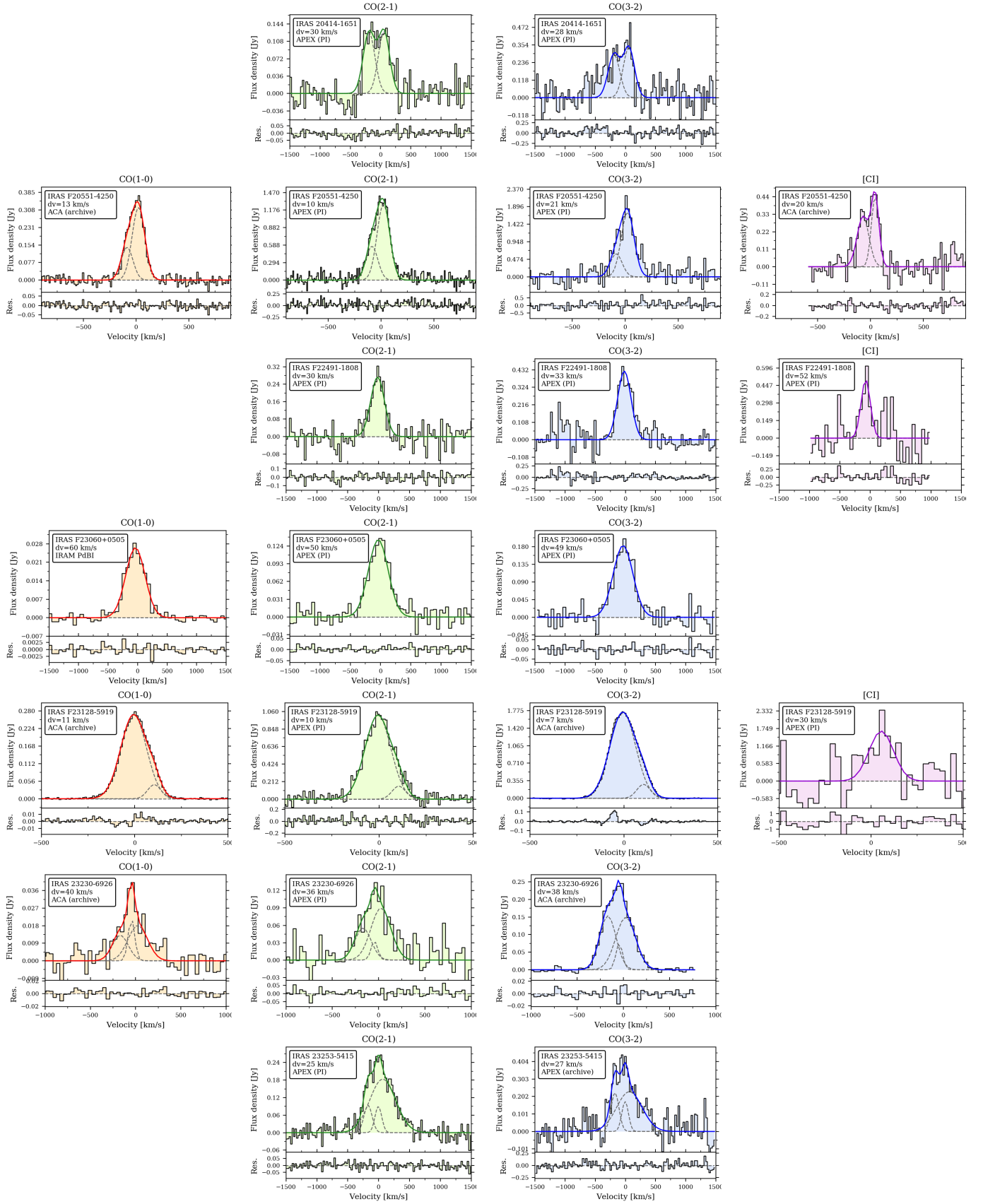
Fig. B.5. Continued from Fig. B.4. This figure shows sources: IRAS 20414-1651, IRAS F20551-4250, IRAS F22491-1808, IRAS F23060+0505, IRAS F23128-5919, IRAS 23230-6926, and IRAS 23253-5415.
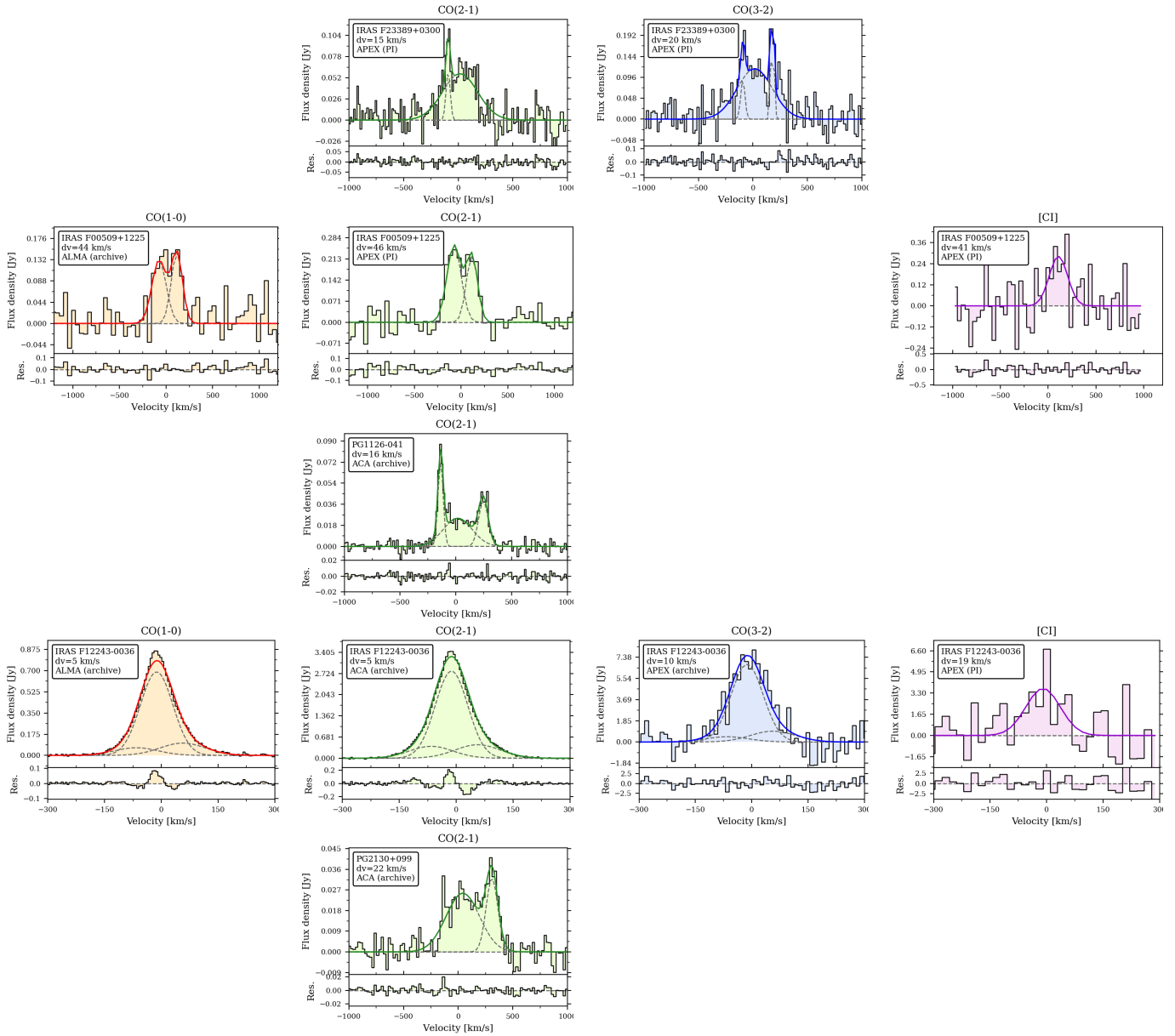
Fig. B.6. Continued from Fig. B.5. This figure shows sources: IRAS F23389+0300, IRAS F00509+1225, PG1126-041, IRAS F12243-0036, and PG2130+099.

Appendix C: Duplicated data sets not employed in the main analysis

Here we report additional spectra reduced for the sources in our sample, which were not included in the main analysis because of the availability of better quality and/or higher priority data, as explained in Sect. 3.1. Figures C.1, C.2, and C.3 show the [CI](1–0), CO(2–1), and CO(3–2) duplicated spectra, respectively.
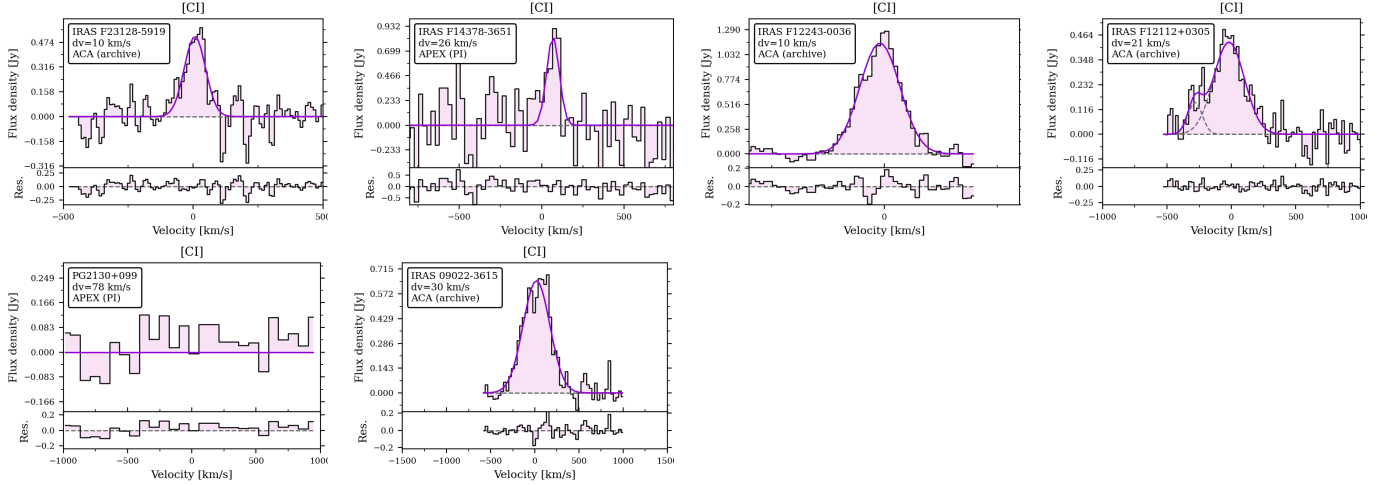

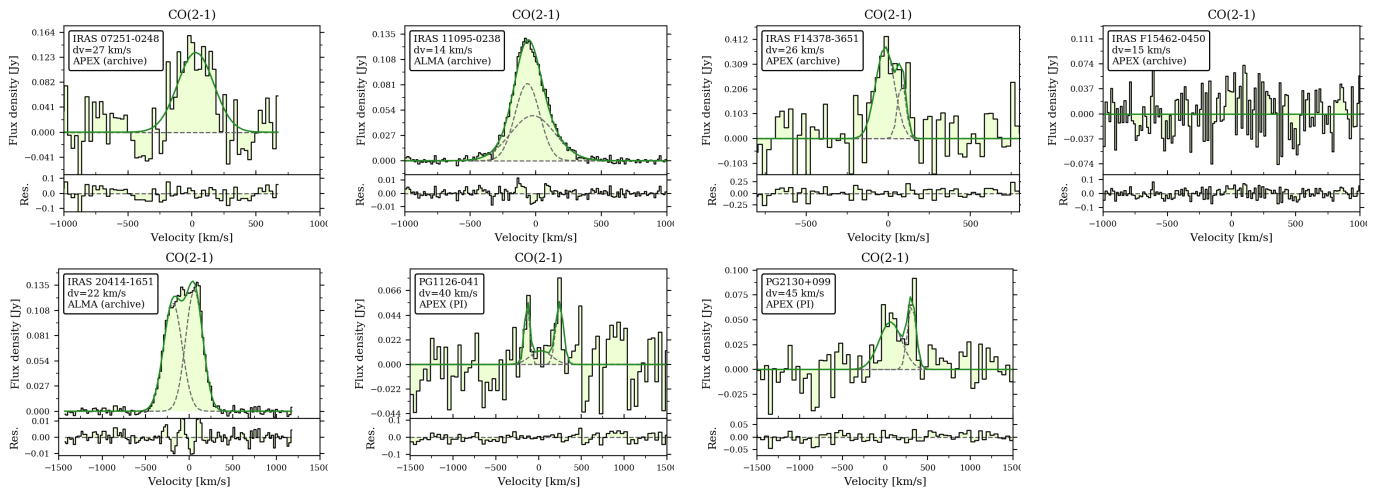**Fig. C.1.** Duplicated [CI](1–0) spectra not used in the analysis.

Fig. C.2. Duplicated CO(2–1) spectra not used in the analysis.

Additional details concerning individual sources are described below.

IRAS F15462-0450

The APEX archival CO(2–1) data set for the source IRAS F15462-0450 was discarded from the analysis because an inspection of the header signals a suspected pointing issue during the observation. This may be the cause of significant flux loss that led to a non detection. The ALMA archival CO(1–0) data for this source show a total flux of 43 ± 16 [Jy km s^{-1}], which would lead to detectable CO(2–1) transition by APEX, which supports our hypothesis of pointing issues. We checked the literature for previous CO(2–1) observations of this source and found an IRAM 30m telescope data set from 2008 published by Xia et al. (2012), where they computed a total integrated CO(2–1) flux of 21.04 ± 1.58 [Jy km s^{-1}] for IRAS F15462-0450.

IRAS F12112+0305

The ALMA CO(1–0) line observations of IRAS F12112+0305 show a low flux value of 34.6 ± 1.1 [Jy km s^{-1}], hinting at a significant missing flux. We proceeded to check the literature for previous CO(1–0) observations of this particular source, and found the work by Chung et al. (2009) reporting a Five College Radio Astronomy Observatory (FCRAO) 14 m telescope observation carried out between 2007 and 2008, with a total CO(1–0) line flux of 64.3 ± 21.04 [Jy km s^{-1}].
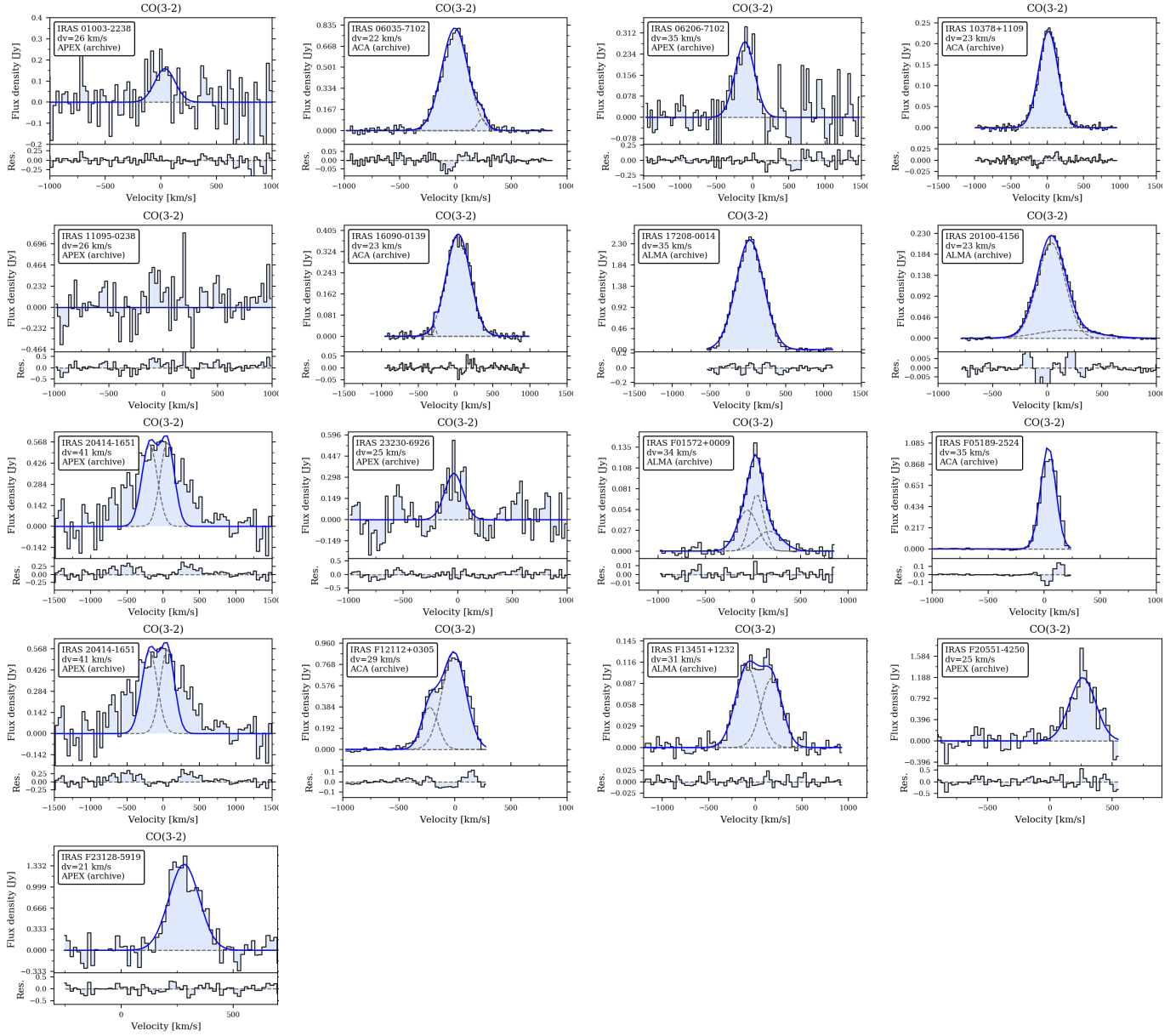
Fig. C.3. Duplicated CO(3–2) spectra not used in the analysis.

Appendix D: Tables listing line fluxes, luminosities, and luminosity ratios

Table D.1 lists the integrated line fluxes and luminosities, obtained through the spectral line fitting, computed using the relations in Sect. 4.2.

Table D.1. Total CO fluxes and luminosities.

Galaxy name	CO(1–0)		CO(2–1)		CO(3–2)		[CI](1–0)	
	$S_{CO}\,dv$	$L'_{CO} \times 10^{-9}$	$S_{CO}\,dv$	$L'_{CO} \times 10^{-9}$	$S_{CO}\,dv$	$L'_{CO} \times 10^{-9}$	$S_{[CI]}\,dv$	$L'_{[CI]} \times 10^{-9}$
	[Jy km s^{-1}]	[K km s^{-1} pc^2]	[Jy km s^{-1}]	[K km s^{-1} pc^2]	[Jy km s^{-1}]	[K km s^{-1} pc^2]	[Jy km s^{-1}]	[K km s^{-1} pc^2]
(1)	(2)	(3)	(4)	(5)	(6)	(7)	(8)	(9)
IRAS 00188-0856	6.4 ± 0.5	5.4 ± 0.4	46.6 ± 4.4	9.8 ± 0.9	45.4 ± 1.2	4.2 ± 0.1		
IRAS 01003-2238	3.5 ± 0.5	2.5 ± 0.4	9.6 ± 2.5	1.7 ± 0.4	21.2 ± 3.8	1.7 ± 0.3		
IRAS F01572+0009	5.9 ± 0.8	8.1 ± 1.2	32.7 ± 2.2	11.2 ± 0.8	49.7 ± 3.9	7.5 ± 0.6		
IRAS 03521+0028			47.8 ± 1.8	14.1 ± 0.5	73.1 ± 5.6	9.6 ± 0.7		
IRAS F05024-1941			22.0 ± 1.6	10.7 ± 0.8	35.5 ± 2.6	7.7 ± 0.6		
IRAS F05189-2524	42.0 ± 1.3	3.7 ± 0.1	133.6 ± 5.8	3.0 ± 0.1	167.0 ± 15.5	1.6 ± 0.2	134.4 ± 17.1	0.7 ± 0.1
IRAS 06035-7102	40.3 ± 1.9	12.7 ± 0.6	154.4 ± 6.7	12.1 ± 0.5	326.5 ± 14.8	11.4 ± 0.5	224.9 ± 17.4	3.9 ± 0.3
IRAS 06206-6315			81.6 ± 4.9	8.7 ± 0.5	115.0 ± 7.0	5.5 ± 0.3		
IRAS 07251-0248			71.3 ± 1.0	6.8 ± 0.1	145.5 ± 12.4	6.2 ± 0.5		
IRAS 08311-2459			136.7 ± 5.3	17.3 ± 0.7	247.4 ± 16.5	13.9 ± 0.9		
IRAS 09022-3615			284.4 ± 7.9	12.5 ± 0.3	368.2 ± 40.3	7.2 ± 0.8	168.0 ± 16.3	1.6 ± 0.2
IRAS 10378+1109			46.7 ± 3.1	11.1 ± 0.7	89.0 ± 6.8	9.4 ± 0.7		
IRAS 11095-0238			43.4 ± 2.9	6.2 ± 0.4	761.5*	48.4*		
IRAS F12072-0444	6.6 ± 0.8	5.6 ± 0.7	49.3 ± 3.4	10.3 ± 0.7	45.2 ± 7.8	4.2 ± 0.7		
IRAS F12112+0305	34.6 ± 1.1	9.2 ± 0.3	183.8 ± 9.0	12.2 ± 0.6	306.7 ± 19.6	9.0 ± 0.6	88.0 ± 12.2	1.3 ± 0.2
IRAS 13120-5453	263.8 ± 4.6	12.2 ± 0.2	838.3 ± 28.6	9.7 ± 0.3	1477.2 ± 55.2	7.6 ± 0.3	794.2 ± 42.8	2.0 ± 0.1
IRAS F13305-1739			11.4 ± 1.3	3.2 ± 0.4				
IRAS F13451+1232	11.8 ± 0.6	8.8 ± 0.5	29.2 ± 4.2	5.5 ± 0.8	80.1 ± 0.2	6.7 ± 0.02		
IRAS F14348-1447			201.0 ± 6.4	17.3 ± 0.5			115.4 ± 16.7	2.2 ± 0.3
IRAS F14378-3651	19.4 ± 1.0	4.4 ± 0.2	78.0 ± 1.6	4.5 ± 0.1			68.5 ± 3.1	0.9 ± 0.01
IRAS F15462-0450	47.0 ± 2.8	23.8 ± 1.4						
IRAS 16090-0139	17.0 ± 0.9	15.5 ± 0.8	97.5 ± 3.9	22.1 ± 0.9	148.3 ± 12.9	15.0 ± 1.3	123.8 ± 13.6	6.2 ± 0.7
IRAS 17208-0014	150.9 ± 2.0	13.5 ± 0.2	583.0 ± 14.6	13.1 ± 0.3	1041.2 ± 36.6	10.4 ± 0.4	339.1 ± 26.0	1.7 ± 0.1
IRAS 19254-7245			170.0 ± 6.4	7.9 ± 0.3			98.7 ± 13.5	1.0 ± 0.1
IRAS F19297-0406			57.5 ± 3.0	5.3 ± 0.3	214.7 ± 4.6	8.7 ± 0.2		
IRAS 19542+1110	16.5 ± 0.8	3.2 ± 0.15	48.8 ± 3.6	2.3 ± 0.2			93.9 ± 14.0	1.0 ± 0.1
IRAS 20087-0308	30.3 ± 1.6	17.0 ± 0.9	141.8 ± 4.6	19.9 ± 0.6	202.1 ± 4.2	12.6 ± 0.3		
IRAS 20100-4156	11.3 ± 0.2	9.7 ± 0.2	54.7 ± 3.0	11.7 ± 0.6	133.5 ± 8.4	12.7 ± 0.8		
IRAS 20414-1651			63.7 ± 3.1	6.0 ± 0.3	163.0 ± 11.1	6.9 ± 0.5		
IRAS F20551-4250	67.1 ± 1.5	6.1 ± 0.13	292.1 ± 6.5	6.6 ± 0.15	389.0 ± 19.2	3.9 ± 0.2	90.8 ± 5.2	0.5 ± 0.03
IRAS F22491-1808			77.9 ± 4.6	5.9 ± 0.3	133.8 ± 7.4	4.5 ± 0.2	106.2 ± 16.0	1.8 ± 0.3
IRAS F23060+0505	10.7 ± 0.3	16.5 ± 0.5	54.2 ± 3.1	20.9 ± 1.2	70.3 ± 3.6	12.1 ± 0.6		
IRAS F23128-5919	51.2 ± 0.7	5.0 ± 0.1	191.9 ± 4.4	4.7 ± 0.1	329.5 ± 5.4	3.6 ± 0.1	233.3 ± 43.0	1.2 ± 0.2
IRAS 23230-6926	8.3 ± 0.7	4.8 ± 0.4	44.1 ± 3.3	6.3 ± 0.5	83.5 ± 2.4	5.3 ± 0.2		
IRAS 23253-5415			119.6 ± 3.9	25.7 ± 0.8	160.1 ± 10.5	15.3 ± 1.0		
IRAS F23389+0300			24.1 ± 1.3	6.5 ± 0.4	52.4 ± 3.1	6.3 ± 0.4		
IRAS F00509+1225	47.4 ± 4.7	8.7 ± 0.9	80.6 ± 6.1	3.7 ± 0.3			67.7 ± 16.4	0.7 ± 0.2
PG1126-041			16.7 ± 0.4	0.7 ± 0.02				
IRAS F12243-0036	101.6 ± 1.0	0.2 ± 0.003	428.2 ± 5.6	0.3 ± 0.003	862.5 ± 56.3	0.2 ± 0.02	520.4 ± 61.5	0.1 ± 0.001
PG2130+099			22.5 ± 1.8	1.1 ± 0.1			72.4*	0.78*

Notes. We compute the 3σ upper limit on the total integrated line flux, following $\int S_{\text{line,dv}} < 3\sigma_{\text{rms,channel}} \sqrt{\delta v_{\text{channel}}}\Delta v_{\text{line}}$, where $\sigma_{\text{rms,channel}}$ is the rms noise per spectral channel, $\delta v_{\text{channel}}$ is the channel width, and Δv_{line} is the expected line width (assumed to be equal to the CO(2–1) line width).

Appendix E: Additional relations explored

In this appendix, we show the relations between the r_{CICO} and different galaxy properties: SFR, L_{AGN}, M_{mol}, τ_{dep}, and α_{AGN} (Fig. E.1). In the main body of the text we plot the relation with L_{IR} (see Fig. 9). We do not retrieve any significant relations for any of the quantities studied here, as can be seen from the Pearson correlation coefficients and p-values reported in each graph.
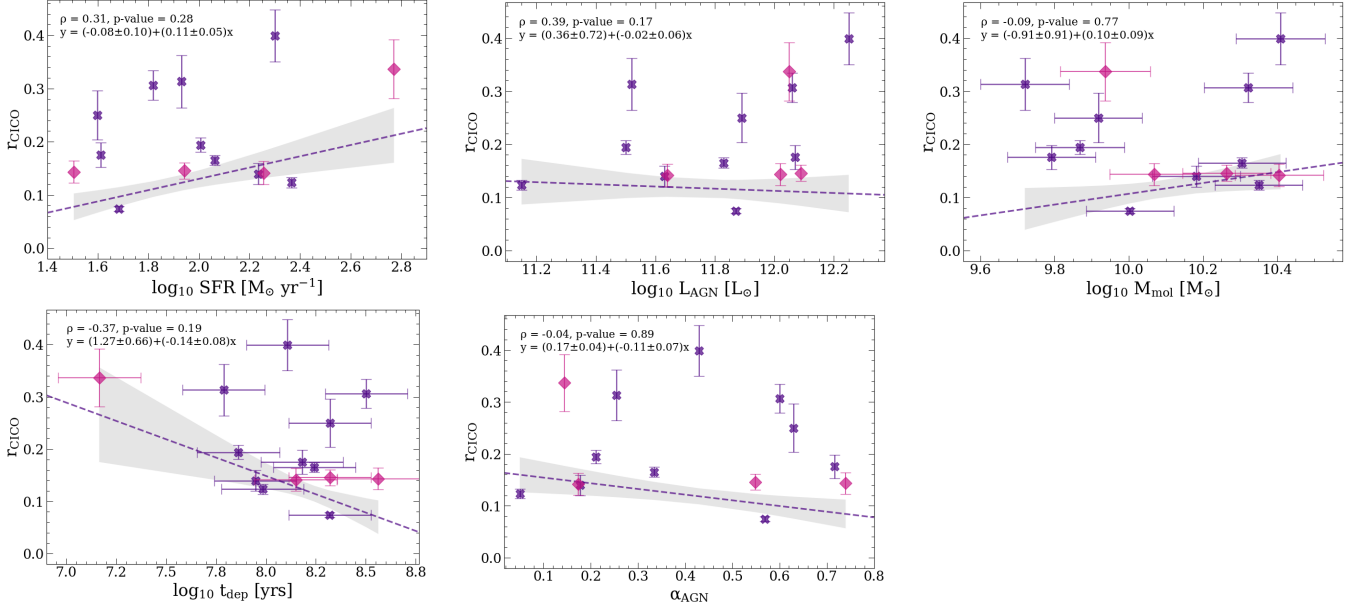

Fig. E.1. r_{CICO} plotted as a function of different galaxy properties, namely: SFR, L_{AGN}, M_{mol}, τ_{dep}, and α_{AGN}. Symbols and notation are as in Fig. 9 for our sample of ULIRGs.